2022

# Investigation Of Stripes, Spin Density Waves And Superconductivity In The Ground State Of The Two-Dimensional Hubbard Model

Hao Xu
*William & Mary - Arts & Sciences*, hxu10@email.wm.edu

## Recommended Citation

Xu, Hao, "Investigation Of Stripes, Spin Density Waves And Superconductivity In The Ground State Of The Two-Dimensional Hubbard Model" (2022). *Dissertations, Theses, and Masters Projects.* William & Mary. Paper 1673281720.
https://dx.doi.org/10.21220/s2-hr7r-jy66

# Investigation of Stripes, Spin Density Waves and Superconductivity in the Ground State of the Two-Dimensional Hubbard Model

Hao Xu

Cangzhou, Hebei, China

Master of Science, College of William & Mary, 2017
Bachelor of Physics, University of Science and Technology of China, 2015

A Dissertation presented to the Graduate Faculty
of The College of William & Mary in Candidacy for the Degree of
Doctor of Philosophy

Department of Physics

College of William & Mary
August 2022

# APPROVAL PAGE

This Dissertation is submitted in partial fulfillment of
the requirements for the degree of

Doctor of Philosophy

Hao Xu

Hao Xu

Approved by the Committee July 2022

Committee Chair
Shiwei Zhang, Adjunct Professor, Physics
College of William & Mary

Enrico Rossi

Co-Chair
Enrico Rossi, Associate Professor, Physics
College of William & Mary

Konstantinos Orginos, Calkins-Ritter Professor, Physics
College of William & Mary

Seth Aubin

Seth Aubin, Associate Professor, Physics
College of William & Mary

Junping Shi

Junping Shi, Professor, Math
College of William & Mary

# ABSTRACT

The Hubbard model is a "paradigmatic" model in the realm of condensed matter physics. Recently a work with various state-or-art methods established the ground state stripe order near 1/8 doping and strong on-site interaction. Therefore, in this thesis, we determine the spin and charge order of ground state of 2D doped Hubbard model in its simplest form (with only on site repulsion and nearest-neighbor hoping) with various doping and small to medium interaction. At half-filling, the ground state is known to be an antiferromagnetic Mott insulator. Doping Mott insulators is believed to be relevant to the superconductivity observed in cuprates. We employ one of the state-of-art method, the auxiliary field quantum monte-carlo (AFQMC) with self-consistently optimized gauge constraints, to systematically study this model. With carefully finite size scaling, we map out the ground state phase diagram in terms of spin and charge order. The result shows a modulated antiferromagnetic (AFM) order present from near half-filling to about 1/5 doping.

The doped Hubbard model is believed to be relevant to high temperature superconductivity in cuprates. We employ AFQMC together with the density matrix renormalization group (DMRG) method to study the superconducting order parameter in the ground state of the Hubbard model when a next-nearest-order hopping, $t'$, is included. Our algorithmic advances include a more robust procedure for self-consistent constraint in AFQMC and twist average boundary conditions which can handle finite size effects much more effectively. We compute the superconducting order parameter in the ground state for a number of parameter sets ($t'$, doping) and discuss its interplay with magnetic and charge orders.

# TABLE OF CONTENTS

Acknowledgments . . . iii

List of Tables . . . iv

List of Figures . . . v

CHAPTER

- 1 Introduction . . . 2
- 2 Methodology . . . 7
  - 2.1 Projection . . . 7
  - 2.2 Auxiliary field quantum Monte-Carlo (AFQMC) . . . 10
  - 2.3 Self-consistent constraint . . . 15
- 3 Ground state phase diagram of the 2D repulsive pure Hubbard model . . . 18
  - 3.1 Benchmark example . . . 18
  - 3.2 Finite size scaling . . . 20
  - 3.3 Determining the wavelength of the collective modes . . . 29
  - 3.4 Phase diagram . . . 31
- 4 Superconductivity pairing order in Hubbard model with next nearest hoping 40
  - 4.1 Computation of the pairing order parameter . . . 40
    - 4.1.1 Particle hole transformation . . . 42
    - 4.1.2 Twist average boundary condition . . . 44
    - 4.1.3 AFQMC approach with self-consistent constraint . . . 47
  - 4.2 Benchmark study with AFQMC and DMRG . . . 51
    - 4.2.1 t'=-0.2t . . . 51

4.2.2 t’=0.2t . . . . . . . . . . . . . . . . . . . . . . . . . . . . . . 56
4.3 Finite size scaling of pairing order parameter . . . . . . . . . . . . . . . 60
4.4 Stripe order and its relationship with superconductivity in t’ model . . 63
5 Summary and perspective . . . . . . . . . . . . . . . . . . . . . . . . . . . 72

APPENDIX A

Additional filling of stripes . . . . . . . . . . . . . . . . . . . . . . . . . 74

APPENDIX B

Diagonal vs. linear stripes . . . . . . . . . . . . . . . . . . . . . . . . . 78

APPENDIX C

Double occupancy and effective doping of model . . . . . . . . . . . . . . . . 80

APPENDIX D

Conductivity of model . . . . . . . . . . . . . . . . . . . . . . . . . . . . 86
Bibliography . . . . . . . . . . . . . . . . . . . . . . . . . . . . . . . . . 91
Vita . . . . . . . . . . . . . . . . . . . . . . . . . . . . . . . . . . . . . 97

# ACKNOWLEDGMENTS

Foremost, I would like to thank my advisor, prof. Shiwei Zhang, for his guidance to my PhD study. Under his guidance, I grow up from a nearly blank undergraduate student, to a more proficient scientific researcher. He is always my primary resource for solving my scientific problems encountered during the research. Besides, he is also a good mentor in my lifetime other than study. I feel very lucky, and will never regret being his student. Thank you prof. Zhang!

I am grateful for the rest of my committee members: Prof. Enrico rossi, Prof. Seth Aubin, Prof. Kostas Orginos and Prof.Junping Shi for their insightful comments and suggestions. They help me to polish my dissertations from different perspectives. Thank you all.

I would also like to thank Dr.Hao Shi, Dr.Mingpu Qin and Dr.Yuanyao He, for their generous help with my academic study. It is so enjoyable and enlightening to discuss with them, and learn from them. Now they are also professors in other universities, I wish them all the best and become excellent professors and doctoral advisors like professor Zhang.

What' more, I would like to thank my fellow doctoral students and postdoctoral researchers for coordination and friendship, like Dr. Ettore Vitali, Dr.Chia-Min Chang, Mr. Zhiyu Xiao, Mr. Siyuan Chen, Mr. Yiqi Yang ......

I gratefully acknowledge the Center for Computational Quantum Physics (CCQ), Flatiron Institute for support and hospitality. Most of the computing was carried out at the Flatiron Institute, with the rest carried out at computational facilities of College of William and Mary, and XSEDE. The Flatiron institute is a division of the Simons Foundation.

Specially, I am grateful to Tracy Cui, for her accompany in my last two years of PhD study. Although she doesn't help in my academic area, but I would say, without her, I will never graduate so successfully. Every time I failed and in depression, I can find encouragement from her. It's so enjoyable to be with you, Tracy Cui.

Finally, I would like to thank my great parents. I behaved very much like autism in my childhood, all the others suggests my parents to give me up and raise another children, but my parents always believe I would be great in the future. I cannot imagine how they raised a child like me for more than 20 years, until I go aboard for PhD study. They are always saying they are proud to have a child like me, but I'd rather say I am proud to be a child of them. There are more people I would like to thank, but due to the limited space, I need to stop here. Thank you all!

# LIST OF TABLES

3.1 Comparison of the computed total energies (per site) in the half-filled and filled stripe states at $U = 12$ and $\delta = 1/12$, in cylinders with widths 4 and 8, and lengths 24 and 48. The system setup is the same as in Fig. 3.10. Half-filled stripe state has lower energy in width-4 systems but higher energy in width-8 systems. A correction has been applied to the energies to account for finite Trotter step size [1]. . . . . . . . . . . . . . . . . . . . . . . . . . 31

3.2 Comparison of the energy per site in the half-filled ($\lambda = 6$), 2/3 filled ($\lambda = 8$) and filled ($\lambda = 12$) stripe states at $U = 8$ and $\delta = 1/12$ in two different lattice sizes. Fully periodic supercells are studied here, with no pinning fields. Half-filled stripe state has the highest energy in both systems. The 2/3-filled stripe state has the lowest energy in the width-6 supercell, while its energy is indistinguishable from that of the filled stripe state in the width-8 supercell. Both self-consistency and the use of a linear combination of trial wavefunctions with different stripe fillings lead to the filled stripe state as the ground state. . . . . . . . . . . . . . . . . . . . . . . . . . . . . . . 31

4.1 benchmark comparison of a non-interacting system using two types of twist boundary conditions, type A (picking up a phase only when particles cross the boundary) and type B (splitting the phase over all the lattice cites evenly). The system is $20 \times 4$, $t' = -0.2t$, with chemical potential $\mu = 0.8$ and twist angle $k_x = 1.2994\pi, k_y = 0.6026\pi$. These results shows two type of boundary conditions are equivalent. . . . . . . . . . . . . . . . . . . . . . 46

B.1 Energy comparison for linear and diagonal stripe states at $U = 12$. We can see linear stripe state always has lower energy. . . . . . . . . . . . . . . . . . 79

C.1 Detailed double occupancy result in Fig.C.2 . . . . . . . . . . . . . . . . . . . 85

# LIST OF FIGURES

1.1 A schematic figure of the 2-dimensional Hubbard model, where t,t' denote the nearest (next nearest) hopping and U is the repulsive energy for double occupation of a site. Up arrows and down arrows correspond to up-spin and down-spin electrons, respectively. This figure is originated from the article [2] . . . . . . . . . . . . . . . . . . . . . . . . . . . . . . . . . . . . . . . 3

3.1 The staggered spin density $(-1)^{i_x+i_y}S_z(i)$ along $x$-direction for $20\times4$ system with 1/10 doping and $U = 6$ in the self-consistent CP-AFQMC calculation. Results are averaged over different rows ($i_y$ values). After convergence, the CP-AFQMC result agrees well with the accurate DMRG results (black line). 20

3.2 The corresponding hole density in the same system as in Fig. 3.1: $20 \times 4$ cylinder with 1/10 doping and $U = 6$. There is noticeable discrepancy in the self-consistent CP-AFQMC hole density from the accurate DMRG result (black line). However the stripe structure is the same. . . . . . . . . . 21

3.3 Insensitivity of the long-range order to the choice of self-consistent method. Method 1 is the independent particle self-consistent method, and method 2 is the natural orbital self-consistent method. Although two results have a little discrepancy in spin and charge density, they get exactly the same spin and charge pattern. . . . . . . . . . . . . . . . . . . . . . . . . . . . . . 22

3.4 Insensitivity of the long-range order to the strength of the spin local pinning field. Staggered spin density (up) and hole density (down) are shown for a $32 \times 6$ cylinder with 1/8 doping and $U = 6$. The strengths of the pinning field ranges from 0.2 to 0.8. Converged results from self-consistent CP-AFQMC are shown for each system. The pinning field has little effect on the spin and hole density, especially in the "bulk" of the system. . . . . . . 23

3.5 Insensitivity of the long-range order to the strength of the local pinning field. Staggered spin density (up) and hole density (down) are shown for a $32 \times 6$ cylinder with 1/8 doping and $U = 6$. The strengths of the pinning field ranges from 0.2 to 0.8. Converged results from self-consistent CP-AFQMC are shown for each system. The pinning field has little effect on the spin and hole density, especially in the "bulk" of the system. . . . . . . . . . . . 24

3.6 Presence and absence of long-range order with supercell system size. The staggered spin density is shown for two interaction strengths, $U = 2$ (top) and $U = 4$ (bottom), at $h = 1/12$ doping, each for a sequence of supercell sizes. All results are for cylinders with width 8, and the staggered spin densities are plotted along the long ($x$) direction. As the length of the cylinder is increased, the staggered spin density vanishes for $U = 2$ but remains a constant for $U = 4$. . . . . . . . . . . . . . . . . . . . . . . . . . 25

3.7 Spin structure factor $S_s(k_x, \pi)$ for a variety of simulation cell sizes, at two interaction strengths, $U = 2$ (top) and $U = 4$ (bottom). All systems are at $\delta = 1/12$ doping. A peak is seen at $k_x = \frac{11}{12}\pi$. With the increase of systems size, the peak descreases and vanishes at $U = 2$ but increases and saturates at $U = 4$. Note the different vertical scales in the two panels. . . . . . . . 27

3.8 Finite size scaling of the spin structure factors in Fig. 3.7. An extrapolation with $L_y$ is performed for each set of cylinders with the same length, shown in the left panel for $U = 2$ and middle panel for $U = 4$. This is followed by an extrapolation with respect to the length of the cylinders, $L_x$, shown in the right panel for both $U$ values. At the TDL, the peak value of the spin structure factor vanishes for $U = 2$, while it reaches a finite value for $U = 4$. 28

3.9 Staggered spin (top panel) and hole (bottom) densities at $\delta = 1/12$ doping and $U = 4$, in width-6 cylinders as the length $L_x$ is varied. Results are omitted at the left edge ($i_x = 1$), where the pinning field is applied. When $L_x$ is commensurate with the expected wavelengths for spin and charge orders ($1/\delta$ and $2/\delta$), the spin and charge density waves are least frustrated and have the largest amplitude. . . . . . . . . . . . . . . . . . . . . . . . . 32

3.10 Different behaviors in width-4 (top panel) and width-8 (bottom) cylinders. Staggered spin densities are shown for $\delta = 1/12$ doping with $U = 12$. The red curves show results for cylinders of length $L_x = 24$, while the blue curves show those with $L_x = 48$. . . . . . . . . . . . . . . . . . . . . . . . . . 33

3.11 Example of energy per site calculation with different $\Delta\tau$ in $24 \times 4$ lattice, U=12, 1/12 doping. By the linear extrapolation of the result with $\Delta\tau^2$, we can greatly reduce the Trotter error and get more precise energy calculation. 34

3.12 Phase diagram of spin and charge orders in the pure Hubbard model. The black curve gives a rough estimation of the phase boundary based on the green squares representing parameters with modulated AFM spin and charge order and red cycles representing those without. The black dashed curve is the phase boundary from unrestricted Hartree-Fock [3] for reference. A ($U = 2$, $\delta = 1/12$) and B ($U = 4$, $\delta = 1/12$) denote the two examples shown in Figs. 3.6, 3.7, and 3.8. . . . . . . . . . . . . . . . . . . . 37

3.13 Staggered spin (up) and hole (down) density at 1/12 doping for different $U$ values. We can find that the stripe order develops only with $U \geq 4$. . . . . 38

3.14 taggered spin (up) and hole (down) density at $U = 6$ for different dopings. We can find that the stripe order only develops with $\delta \leq 1/8$. . . . . . . . 39

4.1 The detailed self-consistent iteration procedure for calculating pairing order for each $h_p$. . . . . . . . . . . . . . . . . . . . . . . . . . . . . . . . . 49

4.2 The example of $16 \times 4$ cylinder with $U = 8$, $t' = -0.2t$ and $\delta = 1/4$ to illustrate our procedure and accuracy with DMRG. Top: the iteration procedure using initial $\alpha = 0.1$. Bottom: iteration procedure using initial $\alpha = 1.0$. It turns out that final pairing order and $\alpha$ value is independent of the initial value chosen, and have excellent agreement with DMRG calculation. 50

4.3 The AFQMC and DMRG energy and pairing order result for 1/5 doping and $t' = -0.2$ with PBC. Although the discrepancy between DMRG and QMC is greater than that for 1/4 doping, we find that two states are competing in DMRG, with very close energy (only 0.2% relative error). In fact, AFQMC is more consistent with the first excited state of DMRG with $h_p < 0.12$, while AFQMC agrees better with DMRG ground state with $h_p > 0.13$ . . 52

4.4 The pairing order parameter for each twist value in the $y$ direction with pairing field $h_p = 0.205$. The twists in the $y$ direction ranges for 0(PBC) to $\pi$(Anti-PBC). The red shaded area is where the first few QMC excited states falls, while black dashed line is the DMRG first excited state. The figure shows that the QMC and DMRG ground and first few excited states range overlaps, or at least they are very close to each other. The twist average order parameter value for this pairing field is 0.054(3) for DMRG and 0.052(3) for QMC, which means the discrepancies between DMRG and QMC on each twist bond cancel each other out when using twist average value for this system. . . . . . . . . . . . . . . . . . . . . . . . . . 54

4.5 The twist average order parameter results on different lattice sizes and different boundary condition, with $t' = -0.2t$ and 1/5 doping. The twist average DMRG on a cylinder $20 \times 4$ system have excellent overall agreement with AFQMC, and the twist average value $20 \times 4$ cylinder system is nearly the same as systems with both sides periodic, which means 20 is long enough for finite size scaling. However, the finite size effect from the width of system is crucial, since there is huge difference between $20 \times 4$ and $20 \times 16$ twist average results. . . . . . . . . . . . . . . . . . . . . . . . . . . . 55

4.6 The staggered spin density benchmark comparison of DMRG and QMC results for 1/5 doping with $t' = -0.2t$, with PBC(above) and Anti-PBC(below). The magnetic pinning fields $v_p = 0.25$ are added on both periodic sides of the PBC lattice, and only one side in Anti-PBC lattice. As a result, all figures with both methods shows stripe pattern, but the wavelength for DMRG and QMC with PBC are different. It turns out that in QMC, the energy of the stripe state, which is same as DMRG, is only 0.001 above the energy of the ground state. In APBC calculation, the DMRG and QMC have excellent agreement. . . . . . . . . . . . . . . . . . . . . . . . 57

4.7 The bencmark comparison of DMRG and QMC result for 1/8 doping (upper panel) and 1/5 doping (lower panel) with $t' = 0.2t$, with lattice sizes $16 \times 4$ and $20 \times 4$ and both PBC. Both methods have good agreement at both doping. . . . . . . . . . . . . . . . . . . . . . . . . . . . . . . . . 58

4.8 The benchmark comparison of DMRG and QMC result for 1/8 doping with $t' = 0.2t$, with PBC and Anti-PBC. The upper panel shows the $16 \times 4$ result and the lower panel shows the $16 \times 6$ results. In this figure, both DMRG and AFQMC shows stronger superconducting properties in PBC lattice of 4 legs cylinder, and Anti-PBC lattice in 6 legs cylinder. . . . . . . . . . 59

4.9 The benchmark comparison of DMRG and QMC result for 1/8 doping with $t' = 0.2t$, with pairing field strengths $h_p = 0.021$ and $h_p = 0.134$ at each twist value. The upper panel shows $16 \times 4$ result and the lower panel shows $16 \times 6$ results. In this figure, both QMC and DMRG shows a sharp peak at $k_y = 0$ in the 4 legs cylinder, and $k_y = \pi$ in the 6 legs cylinder. . . . . . . 61

4.10 The staggered spin density benchmark comparison of DMRG and QMC results for 1/8 doping with $t' = 0.2t$, with PBC(above) and Anti-PBC(below). Magnetic pinning fields $v_p = 0.25$ are added on both periodic sides in both figures. Both figure shows the excellent agreement between DMRG and AFQMC. . . . . . . . . . . . . . . . . . . . . . . . . . . . . . . . 62

4.11 Finite size scaling of the pairing order parameter with $t' = -0.2t$ and 1/5 doping. The top plot shows the twist average results for the pairing order parameter due to the pairing field in various lattice sizes(cyl represents cylinder boundary condition), and the middle plot is the linear extrapolation results from the top plot, which is performed with respect to the inverse of system width $1/L_y$. The resulting pairing order parameter $\Delta_\infty(h_p)$ is shown on the left. Then, in the bottom plot, for each $h_p$, both linear and quadratic extrapolation are performed to obtain $\Delta_\infty(0)$, with results 0.016(2) and 0.015(3). These results shows significant evidence for superconductivity exists in the Hubbard $U = 8$, $t' = -0.2t$ and 1/5 doping system. . . . . . 64

4.12 Finite size scaling of the pairing order parameter with $t' = -0.2t$ and 1/5 doping. The top plot shows the twist average results for the pairing order parameter due to the pairing field in various lattice sizes(cyl represents cylinder boundary condition), and the middle plot is the linear extrapolation results from the top plot, which is performed with respect to the inverse of system width $1/L_y$. The resulting pairing order parameter $\Delta_\infty(h_p)$ is shown on the left. Then, in the bottom plot, for each $h_p$, both linear and quadratic extrapolation are performed to obtain $\Delta_\infty(0)$, with results 0.006(4) and 0.006(3). These results shows little superconducting pairing order in Hubbard $U = 8$, $t' = 0.2t$ and 1/8 doping system. . . . . . . . . . 65

4.13 The pairing order parameter $\Delta_\infty(0)$ for each doping with $t' = 0.2t$ and $t' - 0.2t$. The plot indicates that at $t' = -0.2t$, superconductivity pairing is stronger than that of $t' = 0.2t$. Besides, both $t' = 0.2t$ and $t' - 0.2t$ see vanishing superconducting order with the doping increases above 1/4 doping. . . . . . . . . . . . . . . . . . . . . . . . . . . . . . . . . . . . 66

4.14 Staggered spin density of 1/5 doping and $t' = -0.2t$ with various lattice sizes, from $20 \times 6$ to $40 \times 8$. We can see spin density wave exists, which the wavelength $1.5/h$ is different from pure Hubbard model with $2/h$ . . . . . 67

4.15 Staggered spin density for 1/8 doping and $t' = -0.2t$ with various lattice sizes, from $16 \times 6$ to $32 \times 8$. We can see spin density wave exists, but the wavelength is $1.5/h$, which is different from pure Hubbard model with $2/h$ 68

4.16 Staggered spin density for 1/8 doping and $t' = 0.2$ with various lattice sizes, from $16 \times 6$ to $32 \times 8$. No clear common spin pattern is observed in these lattice sizes . . . . . . . . . . . . . . . . . . . . . . . . . . . . . . . . . 69

4.17 The superconducting pairing order for PBC (upper) and APBC (lower) in $16 \times 4$ cylinder with 1/8 doping and $t' = 0.2$. The red solid curve is the original QMC result while orange dashed lines represents the results with spin-like pinning fields similar with the ground state spin pattern added on all of the lattices. The results shows better agreement with DMRG after the spin-like pinning fields added, but the relationship of the stripe order with the superconducting pairing order is unclear, since in the PBC lattice, the growth of spin density pattern contributes to the growth of pairing order, while in the Anti-PBC lattice, the growth of spin density waves occurs as the pairing order decreasing. . . . . . . . . . . . . . . . . . . . . . . . . 71

A.1 Staggered spin (top panel) and hole (bottom) densities at $\delta = 1/10$ doping and $U = 5$, in width-6 cylinders as the length $L_x$ is varied. Results are omitted at the left edge ($i_x = 1$), where the pinning field is applied. When $L_x$ is commensurate with the expected wavelengths for spin and charge orders ($1/\delta$ and $2/\delta$), the spin and charge density waves are least frustrated and have the largest amplitude. . . . . . . . . . . . . . . . . . . . . . . . 75

A.2 Staggered spin (top panel) and hole (bottom) densities at $\delta = 1/8$ doping and $U = 6$, in width-6 cylinders as the length $L_x$ is varied. Results are omitted at the left edge ($i_x = 1$), where the pinning field is applied. When $L_x$ is commensurate with the expected wavelengths for spin and charge orders ($1/\delta$ and $2/\delta$), the spin and charge density waves are least frustrated and have the largest amplitude. . . . . . . . . . . . . . . . . . . . . . . . 76

A.3 Staggered spin (top panel) and hole (bottom) densities at $\delta = 1/6$ doping and $U = 8$, in width-6 cylinders as the length $L_x$ is varied. Results are omitted at the left edge ($i_x = 1$), where the pinning field is applied. When $L_x$ is commensurate with the expected wavelengths for spin and charge orders ($1/\delta$ and $2/\delta$), the spin and charge density waves are least frustrated and have the largest amplitude. . . . . . . . . . . . . . . . . . . . . . . . . . 77

C.1 The comparison of double occupancy of Hubbard model at half-filling, between AFQMC and Metropolis, which can get results without system error since t does not constraint the path. The results the highly accuracy of double occupancy calculation. . . . . . . . . . . . . . . . . . . . . . . . 82

C.2 Double occupancy of pure Hubbard model with respect to U in different doping. . . . . . . . . . . . . . . . . . . . . . . . . . . . . . . . . . . . 83

C.3 Effetive hoping of pure Hubbard model with respect to U in different doping. 84

D.1 The charge gap of several examples, one (U=3, 1/7 doping) is paramagnetic in the TDL and others (U=4.5 with 1/10 doping, U=5 with 1/8 doping, U=6 with 1/7 doping, U=7 with 1/6 doping) indicates the existence of SDW in the TDL according to the Fig.refphase-diagram. All results are with-8 cylinder. With the increase of size, all results, whether have SDW or not, see the charge gap vanishes to zero. This indicates the conductive state of doped Hubbard model, regardless the existence of SDW. . . . . . 87

D.2 The quantum metric tensor (QM tensor) of all the systems. The lower panel includes systems that have SDW in TDL, while systems which is paramagnetic in TDL is included in the upper panel. We observe clearly diverge QM tensor value in the upper panel, which indicates the strong conductivity in the paramagnetic model. However, although the value is much smaller, we cannot decide quantitatively whether the QM tensor value converge in the lower panel. Thus we cannot decide whether system is conducting or not in our present QM tensor data. . . . . . . . . . . . . 89

# INVESTIGATION OF STRIPES, SPIN DENSITY WAVES AND SUPERCONDUCTIVITY IN THE GROUND STATE OF THE TWO-DIMENSIONAL HUBBARD MODEL

# CHAPTER 1

# Introduction

The study of quantum many body systems has been an outstanding challenge in recent decades. Among them, the Hubbard model [4] is one of the most studied models in condensed matter physics. It is a paradigm model like the Ising model is in statistical physics. Although its form is simple, the Hubbard model hosts rich physics with the variation of interaction strength, doping level, temperature, lattice geometry, and so on [5]. What's more, on the square lattice, it is widely believed that the Hubbard model contains key physics which is relevant to high temperature superconductivity in cuprates [6].

The Hamiltonian of the Hubbard model is as follows (a schematic figure shown as Fig. 1.1):

$$H = -t \sum_{\langle i,j \rangle;\sigma} c^\dagger_{i\sigma} c_{j\sigma} - t' \sum_{\langle\langle i,j \rangle\rangle;\sigma} c^\dagger_{i\sigma} c_{j\sigma} + U \sum_i n_{i\uparrow} n_{i\downarrow} + \sum_i v_{i\sigma} n_{i\sigma} \tag{1.1}$$

where the coordinates of the lattice site labeled $i$ are given by $\mathbf{r}_i = (i_x, i_y)$. $c^\dagger_{i\sigma}$ ($c_{i\sigma}$) represents the creation (annihilation) operator on site $i$, with $\sigma = \uparrow, \downarrow$ being the spin of the election. The operator $n_{i\sigma} = c^\dagger_{i\sigma} c_{i\sigma}$ measures the number of electrons with spin $\sigma$ on site $i$. We denote the average hole density, or doping, in the system as $h = 1 - N_e/N_{site}$ where $N_e$

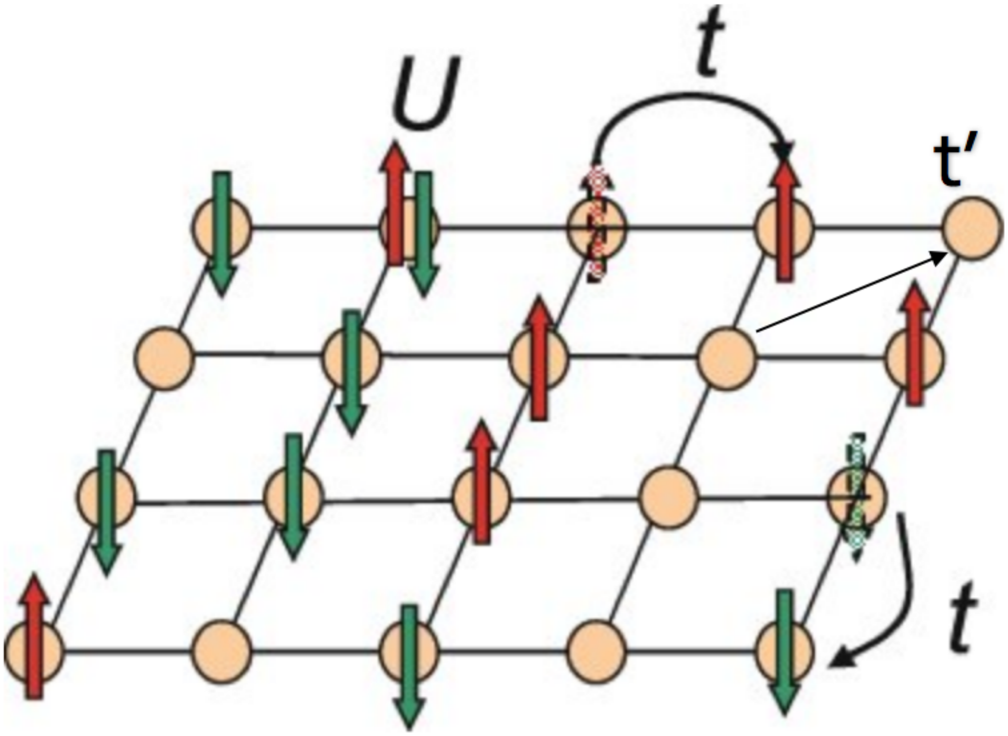

FIG. 1.1: A schematic figure of the 2-dimensional Hubbard model, where t,t' denote the nearest (next nearest) hopping and U is the repulsive energy for double occupation of a site. Up arrows and down arrows correspond to up-spin and down-spin electrons, respectively. This figure is originated from the article [2]

is the total number of electrons and $N_{site} = L_x \times L_y$ the number of sites of the lattice. We set $t$ as the energy unit in this work. The first two terms in the Hubbard model represent the kinetic energy, with first (second) term describing nearest (next nearest) hoping . We will call the model "pure Hubbard model" in the case $t' = 0$. The third term represents the interaction energy, and the last term is a spin-dependent potential from an external field, which is applied to explicitly break the SU(2) symmetry. We use the external field as a pinning field, applied to the edges, in such a way that the symmetry breaking allows us to measure local densities as opposed to the more demanding correlation functions [7]. As we illustrate in Fig.3.4, the effects of the pinning field are negligible in the bulk of the system. So the details of the field does not affect the characterization of the ground state.

In the general form of equation 1.1, with only a few exceptions [8, 9], this model cannot be solved analytically. The size of the Hibert space grows exponentially with the system size, so straightforward numerical diagonalization is limited to small lattice sizes. Most studies of the model nowadays depend on numerical methods. [10, 5].

When the number of electrons is same as the number of lattice (half-filling case), it has already established that the ground state of Hubbard model has anti-ferrimagnetic (AFM) order with mott-insulating at any finite interaction strength [11]. When holes are added, the ground state will tell a different story, and it is believed to be important for understanding the mechanism of high temperature superconductivity to study this "story" [12]. Previous study has shown different possibilities of what this "story" is like, including spin density waves(SDW), charge density waves(CDW) [13, 14, 15, 16], superconductivity [17, 18]. For example, in 2017 it has shown that, near 1/8 doping, a filled stripe (wavelength equals to reverse of doping) will be observed in the ground state, with state-of-the-art numerical many-body correlated methods applied collaborating in this paper. [19] Since then, more evidence has confirmed the existence of stripe order in the doped Hubbard model [20, 21, 22].

The study of stripe order in the Hubbard model can be traced back to 1980s in Hartree-Fock [23, 24, 25] and then 1990s in density matrix renormalization group (DMRG) [13] calculations. After that, Constrained-path auxiliary-field quantum Monte-Carlo (AFMQC) found the incommensurate SDW state with AFM order and homogeneous charge correlation at intermediate interaction.[15]. In both the SDW and stripe states, a unidirectional order is established with the AFM correlations displaying a $\pi$ phase flip across nodes. The doped holes concentrate in the nodal region of the spin modulation in the stripe phase. The formation of the stripe results from compromise between the AFM background and kinetic energy of the holes. Stripe order is widely observed in cuprates [26]. There is evidence suggesting that the stripe order might be the origin of pseudo-gap phase of cuprates [27] when temperature is above the superconducting transition temperature.

However, the existence of stripe order away from 1/8 doping is still not fully understood. In the early experimental studies, 1/8 doping is somehow special to cuprates[28]. Given the relationship between the Hubbard model and cuprates, we can ask a question: "is 1/8 doping also 'special' in the Hubbard model ? If so, how?" In this thesis we determine the ground state phase diagram of the doped Hubbard model by scanning different doping (h) and different interaction strengths (U), with main focus on the existence of SDW and stripe order. We will use the constrained path AFQMC method [1, 14] , with self-consistently optimized constraint[29], to study the ground state. By calculating the spin and charge order of the ground state for different systems sizes, and careful finite size scaling to thermodynamic limit (TDL), we determine whether the ground state of particular interaction U and doping h has SDW phase order or not. Finally, a phase diagram is obtained by these scanned results. We find the existence of SDW and stripe order up to 1/5 doping when interaction is strong enough.

To characterize the spin order, we measure the staggered spin density $S_i = \frac{1}{2}(-1)^{(i_x+i_y)}\langle n_{i\uparrow} - n_{i\downarrow}\rangle$ in the presence of the symmetry-breaking pinning field mentioned above. To characterize the charge order, we measure the local hole density $h_i = \langle 1 - n_{i\uparrow} - n_{i\downarrow}\rangle$.

In most spin and charge calculations, a cylindrical geometry is adopted to accommodate the pinning fields. We study rectangular lattices with either open or periodic boundary conditions on the longer direction ($x$), and either periodic or twist boundary condition on the shorter one ($y$). From now on, when we present the results, unless otherwise specified, the default will be cylindrical cells, namely open along $x$ and periodic along $y$. This allows us to study systems with a size which can accommodate one or multiple periods of density waves or stripe order. We vary the aspect ratio of the simulation cells to confirm the robustness of the results. In some energy and pairing order calculations, we use periodic or twist boundary condition on both sides to further reduce the size effects.

Apart from the nature of the spin and charge order, whether superconductivity exists in the Hubbard model or not is a crucial question is which has drawn tremendous interest in the field of quantum many body physics. Superconductivity seems to have a subtle competition and/or co-existence with stripe order [30, 31, 32, 33]. Based on these facts, and our previous pure Hubbard model study on superconductivity [33], we carry out computations of superconductivity pairing order in the Hubbard model with next nearest neighbor hoping $t'$, with two state-or-art numerical many-body methods, AFQMC together with DMRG.

Our study employs the most recent advance in our algorithms, including a more robust procedure for self-consistent constraint in AFQMC and twist average boundary conditions which can handle finite size effects more effectively. As a result, we have much better data quality. We will firstly discuss the benchmark comparison of pairing order parameter and stripes with DMRG. Then, carefully finite size scaling is used to calculate the superconductivity pairing order at $t' = 0.2$ and $t' = -0.2$ with various doping and interaction strength $U = 8t$. The relation between superconductivity and stripe order is also discussed. We find that the magnetic and charge correlations in t-prime model turn out to be different from that of $t' = 0$.

The following chapters of this thesis are organized as follows. In Chapter 2, we will briefly introduce the AFQMC method, including algorithms, the sign problem and how to control it, independent particle self-consistent iteration.... In Chapter 3, the stripe order of pure Hubbard model is discussed and spin density wave phase diagram as a function of doping $\delta$ and interaction $U$. Other properties like double occupancy, the conductivity will be included in appendix C and appendix D. The superconducting pairing correlation of $t'$ Hubbard model study will be discussed in Chapter 4. Finally, we summary and briefly comment on future research in chapter 5.

# CHAPTER 2

# Methodology

In this chapter, we will give a basic introduction to the AFQMC method. We will also introduce the self-consistent procedure to improve our results.

The auxiliary-field quantum Monte Carlo (AFQMC) method is a general numerical method [34] for correlated many-electron systems, which is being increasingly applied in lattice models, atoms, molecules, and solids [35]. However, we will use Hubbard model as a concrete example here.

## 2.1 Projection

Projection with Monte-carlo sampling plays a key role in the AFQMC method. Given the Hamiltonian of the Hubbard model in equation1.1, the ground state of the Hubbard model can be obtained as below:

$$|\psi_0\rangle = \lim_{\beta\to+\infty} e^{-\beta H} |\psi_T\rangle = (e^{-\Delta\tau H})^n |\psi_T\rangle , \tag{2.1}$$

where $n\Delta\tau = \beta$, and $|\psi_T\rangle$ is the trial wave function, and $E_T$ is the variation energy obtained by the trial wave function. The trial wave function must satisfy $\langle|\psi_0|\psi_T|\rangle \neq 0$ in order to be projected to ground states. In AFQMC, the trial wave function is usually represented by Slater-determinant states. In this work, unrestricted Hartree-Fock form of trial wave function is applied. [34]

In order to separate the kinetic energy term $K$ and potential energy term $V$, we use Trotter-Suzuki decomposition [36]

$$(e^{-\Delta\tau H})^n = (e^{-\Delta\tau(K+V)})^n = (e^{-\frac{1}{2}\Delta\tau K} e^{-\Delta\tau\ V} e^{-\frac{1}{2}\Delta\tau K})^n + O(\Delta\tau^2) \tag{2.2}$$

The Trotter error arises from the omission of the higher order terms. For our typical choice of $\Delta\tau$, the value is actually small compared to other errors when the potential term U is not very large. For very large U, we can make extrapolation to greatly reduce this. In the next chapter, an example will be shown in the Fig. 3.11.

The kinetic term is a one-body operator, which can be easily applied to the initial state of a Slater determinant. The potential term $e^{-\Delta\tau V}$ is not. In the repulsive Hubbard model ($U > 0$), we use the Hubbard-Stratonvich transformation to transform the two-body term $e^{-\Delta\tau\ V}$ into sum of one-body terms [37, 38]

$$e^{-\Delta\tau U n_{i\uparrow} n_{i\downarrow}} = e^{-\Delta\tau U(n_{i\uparrow}+n_{i\downarrow})/2} \sum_{x=\pm 1} \frac{1}{2} e^{-\Delta\tau\gamma x(n_{i\uparrow}-n_{i\downarrow})} \tag{2.3}$$

where $cosh(\gamma) = e^{-\Delta\tau U/2}$. In equation 2.3, which is referred to as spin decomposition, x is an Ising-spin like auxiliary field.

For attractive Hubbard model ($U < 0$), we will use the charge decomposition instead of the spin decomposition

$$e^{-\Delta\tau U n_{i\uparrow}n_{i\downarrow}} = e^{-\Delta\tau U(n_{i\uparrow}+n_{i\downarrow}-1)} \sum_{x=\pm1} \frac{1}{2} e^{-\Delta\tau\gamma x(n_{i\uparrow}+n_{i\downarrow}-1)} \tag{2.4}$$

Since each two-body term can be represented by a sum of two one-body terms, the projection will generate $2^n$ one-body terms, which is still impossible to be computed exactly in large systems, thus, Monte-Carlo sampling is needed.

We can write equation 2.4 in a general form:

$$e^{-\Delta\tau U n_{i\uparrow}n_{i\downarrow}} = \sum_x p(x) e^{\hat{o}(x)} \tag{2.5}$$

where the $\hat{o}(x)$ is a type of one-body operator defined by the auxiliary field $x$, and $p(x)$ is the probability of choosing $x$ and $\sum_x p(x) = 1$. We then can rewrite the projection operator by setting

$$\hat{B}(x) = e^{-\frac{1}{2}\Delta\tau K} e^{\hat{o}(x)} e^{-\frac{1}{2}\Delta\tau K}, \tag{2.6}$$

and write equation 2.1 as

$$|\psi_0\rangle = \sum_{\vec{X}} P(\vec{X}) \prod_{i=1}^{n} \hat{B}(x_i) |\psi_T\rangle\,, \tag{2.7}$$

where the vector $\vec{X}$ represent the choice of $(x_1, x_2 ... x_n)$ and $P(\vec{x}) = \prod_{i=1}^{n} p(x_i)$. We can sample these ground state elements by its probabilities, and the sampled ground state can be represented by

$$|\psi_0\rangle = \sum_k \omega_k |\psi_k\rangle \tag{2.8}$$

where $\omega_k$ represents the weight of $k$th walker.

After getting the ground state, we can measure the observable $\hat{O}$ by

$$\langle\hat{O}\rangle = \frac{\langle\psi_T| e^{-\beta H} O e^{-\beta H} |\psi_T\rangle}{\langle\psi_T| e^{-\beta H} e^{-\beta H} |\psi_T\rangle}, \tag{2.9}$$

which is called back-propagation. For energy measurement and observable that commute with $\hat{H}$, we use the mixed estimator like below

$$E = \langle \hat{H} \rangle = \frac{\langle \psi_T | H e^{-\beta H} | \psi_T \rangle}{\langle \psi_T | e^{-\beta H} | \psi_T \rangle} \tag{2.10}$$

which is more efficient and has much smaller error bar.

Next, we will discuss more about how we calculate the probabilities and conduct the random walk.

## 2.2 Auxiliary field quantum Monte-Carlo (AFQMC)

From the last section, the $2^n$ possibilities of the next step of each walker can be sampled by open-ended random walks. We can use a population of $N_w$ walkers to accomplish this, where $N_w$ is much less than $2^n$ . We first initialize these walkers by the trial wave function, usually with the same weight. During the sampling, the weight of these walkers will change with time, some walkers may be killed and some will multiply.

At the beginning, the initial state represented by these walkers can be written as

$$\left| \psi^{(0)} \right\rangle = \sum_{k=1}^{N_w} \omega_k^{(0)} \left| \phi_k^{(0)} \right\rangle , \tag{2.11}$$

where $|\phi_k^{(0)} >$ is Slater determinant wave function. we conduct the projection by equation 2.7 in Slater determinant space. Each walker will randomly choose $x$ with the probability equal to $p(x)$. Then the corresponding $\hat{B}(x)$ is applied to its Slater-determinant wave function. Since the two body terms have already be decomposed into one body terms, the operation contains only one-body terms. This will turn the current Slater-determinant into another Slater-determinant. [39]. For any $k = 0, 1, 2.....$

$$\left|\psi^{(l+1)}\right\rangle = \sum_{k=1}^{N_w} \sum_{x} p(x)\hat{B}(x)\omega_k^{(k)} \left|\phi_k^{(l)}\right\rangle = \sum_{k=1}^{N_w} \omega_k^{(l+1)} \left|\phi_k^{(l+1)}\right\rangle . \tag{2.12}$$

And after $n$ steps it will become

$$\left|\psi^{(n)}\right\rangle = \sum_{k=1}^{N_w} \omega_k^{(n)} \left|\phi_k^{(n)}\right\rangle . \tag{2.13}$$

During the projection, we will multiply a constant value for the weight of each walkers based on the Monte-Carlo sampling. After several steps, the weight of each walkers $\omega_i$ will differ. Some walkers may have very large weights and some weight value will be particularly small, which will make the efficiency of the sampling lower. In that case, we will introduce the population control procedure. In a word, we will split the walkers with large weight, and eliminate the walkers will small weight with proper probability. By doing the population control, we will preserve the overall statistic distribution and make the weight distribution for different walkers more uniform. The more uniform the weight distribution, the higher efficiency of sampling.

Also, in order to preserve the numerical stability in the Slater determinant, we will apply Modified Gram-Schmidt orthogonalization to each walker every several steps. [40]

In free projection (FP), what we need to do is to project these walkers to sufficiently long imaginary time $\beta$, and measure the energy by equation 2.10 and other observables by equation 2.9 (back propagation). However, in general, this will become very noisy, with an exponentially large number of walkers needed to reduce the variance.

Since electrons are Fermions, the ground state of the Fermi system will be anti-symmetric. The stochastically projected state will be symmetric about $|\phi^{(n)}\rangle$ and $-|\phi^{(n)}\rangle$. After sufficiently long time of projection, the walkers will have equal probability to go to "positive" state $|\phi^{(n)}\rangle$ or negative state $-|\phi^{(n)}\rangle$, and the denominator of equation 2.10 and 2.9 will be close to 0, which will cause the results of measurements to have diverging variance. This is the so called sign problem [34].

Given the conditions above, more techniques are needed to improve our algorithms. To tackle the sigh problem, random walkers should be confined to only one kind of "sign". If any particular walker has the zero overlap with the ground state at imaginary time $l\Delta\tau$

$$\langle\psi_0|\,\phi^{(l)}\rangle = 0, \tag{2.14}$$

it will no longer have any contribution in the future time since for any $l' > 0$

$$\langle\psi_0|\,e^{-l'\Delta\tau H}|\phi^{(l)}\rangle = 0. \tag{2.15}$$

Thus, we need to monitor periodically, and discard any walker that have zero overlap with the ground state. However, we are not able to know what exactly the ground state is. In constrained path monte carlo, we choose the trial wave state as an approximation of the ground state, and eliminate the walkers once they have zero overlap with the trial wave state. Systematic error is introduced in this calculation, however, the error turned out to be very small when interaction is not very large, as we illustrate in Chapter 3.

In order to impose the constraint and reduce the variance, we introduce importance sampling [1, 41]. We define the overlap of the $i$th walker with the trial wave function as

$$O_T(\phi_k) = \langle\psi_T|\phi_k\rangle\,. \tag{2.16}$$

Equation 2.12 can be rewritten as a formally different, but mathematical equivalent form:

$$\left|\widetilde{\psi}^{(l+1)}\right\rangle = \sum_{k=1}^{N_w}\sum_{x}\widetilde{p}(x)\hat{B}(x)\widetilde{\omega}_k^{(l)}\left|\widetilde{\phi}_k^{(l)}\right\rangle = \sum_{k=1}^{N_w}\widetilde{\omega}_i^{(l+1)}\left|\widetilde{\phi}_k^{(l+1)}\right\rangle . \tag{2.17}$$

The equation 2.13 will have the form

$$\left|\widetilde{\psi}^{(n)}\right\rangle = \sum_{k=1}^{N_w}\widetilde{\omega}_k^{(n)}\frac{|\phi_k^{(n)}\rangle}{O_T(\phi_k^{(n)})}. \tag{2.18}$$

Then, the probability of sampling each auxiliary field will be given as

$$\widetilde{p}(x) = p(x)\frac{\langle\psi_T|\hat{B}(x)|\phi_k\rangle}{O_T(\phi_k)}, \tag{2.19}$$

which can be realized by using force bias [41]. In this way, we can have greater probability of sampling the larger weight field, and the determinants that have zero or negative overlap with trial wave function will be prevented from sampling, which will greatly improve our proficiency of sampling, and brings about much smaller variance.

For energy measurement, using the mixed estimator, equation 2.10 can be written as

$$E = \frac{\sum_{k=1}^{N_w}\omega_k^{(n)}E_L(\phi_k)}{\sum_{k=1}^{N_w}\omega_k^{(n)}}, \tag{2.20}$$

where the local energy $E_L(\phi_k)$ is written as

$$E_L(\phi_k) = \frac{\langle\psi_T|H|\phi_k\rangle}{O_T(\phi_k)}. \tag{2.21}$$

Given the form of Hamiltonian in equation 1.1, we can calculate the one-body Green's function as

$$\langle c_{i\sigma}^\dagger c_{j\sigma}\rangle = \frac{\langle\psi_T|c_{i\sigma}^\dagger c_{j\sigma}|\phi_k\rangle}{\langle\psi_T|\phi_k\rangle} = \left[\phi_k^\sigma[(\psi_T^\sigma)^\dagger\phi_k^\sigma]^{-1}(\psi_T^\sigma)^\dagger\right]_{ji} \tag{2.22}$$

which can be obtained by matrix multiplication. Thus, we can calculate the kinetic energy term.

For the interaction energy, which contains two-body operators, we can use Wick's theorem to reduce it into one-body forms as

$$\langle c_{i\uparrow}^\dagger c_{i\uparrow} c_{i\downarrow}^\dagger c_{i\downarrow} \rangle = \langle c_{i\uparrow}^\dagger c_{i\uparrow} \rangle \langle c_{i\downarrow}^\dagger c_{i\downarrow} \rangle - \langle c_{i\uparrow}^\dagger c_{i\downarrow} \rangle \langle c_{i\downarrow}^\dagger c_{i\uparrow} \rangle. \tag{2.23}$$

The second term in the right-hand side of equation should be 0 if spin $\uparrow$ and $\downarrow$ are decoupled in the Slater determinant, and first term can be obtained by one-body calculation just like equation 2.22.

Thus, we can measure the energy after sufficient imaginary time of projection. Even with systematic error introduced from the constraint to control the sign problem, the energy measurement is very accurate with very small statistical variance, especially for closed shell systems [1]. For $4 \times 4$ system with $U = 4$, the relative error between AFQMC and exact diagonalization (ED) is within 0.5% [14]. For $4 \times 20$ system with $U = 6$ and $1/10$ doping, which cannot be tackled by exact diagonalization(ED), the relative error between AFQMC and DMRG is only about 0.1% [42], and the statistical uncertainty is only 0.01% of the value if we use thousands of walkers.

The mixed estimator can only measure observables that commute with the Hamiltonian. For other observable, such as spin density, charge density... we need to use back-propagation to create a so called pure estimate [1], and the results are affected more by the choice of trial wave function. If we use the self-consistent constraint method [29], we are able to obtain iteratively trial wave function closer to the correct state and the systematic error will be greatly reduced. In next chapter, we will discuss this self-consistent method.

## 2.3 Self-consistent constraint

In the previous section, we discussed the technique to tackle the sign problem, and systematic error is introduced due to the choice of trial wave function to impose the exact constraint condition approximately. Thus, better trial wave functions will lead to better results. External methods which can produce better trial wave functions at modest cost are limited. In this section, we will describe a technique that couples the AFQMC method to an independent-particle calculation, which provides the trial wave function by using the feedback of the AFQMC result.

Since we use single Slater-determinant as the trial wave function, it should be obtained from the ground state of a one-body Hamiltonian. We rewrite the Hamiltonian of equation 1.1 as

$$H = K + U \sum_i n_{i\uparrow} n_{i\downarrow} \tag{2.24}$$

where K is the one-body kinetic term that contains all the hoping and external field terms in 1.1, under a generalized mean field approximation, we can rewrite the two body term as below

$$H = K + U \sum_i (n_{i\uparrow} - \langle n_{i\uparrow} \rangle + \langle n_{i\uparrow} \rangle)(n_{i\downarrow} - \langle n_{i\downarrow} \rangle + \langle n_{i\downarrow} \rangle), \tag{2.25}$$

Where $\langle n_{i\sigma} \rangle$ is the expectation value of the electron density operator, and can by measured by the previous AFQMC calculation.

Equation 2.25 can be also rewritten as:

$$H = K + U \sum_i [\langle n_{i\downarrow} \rangle n_{i\uparrow} + \langle n_{i\uparrow} \rangle n_{i\downarrow}] + U \sum_i (n_{i\uparrow} - \langle n_{i\uparrow} \rangle)(n_{i\downarrow} - \langle n_{i\downarrow} \rangle) + U \sum_i \langle n_{i\uparrow} \rangle \langle n_{i\downarrow} \rangle \tag{2.26}$$

In the rewritten equation, the third term is constant and does not affect the trial wave function, the second term is treated as 0 in the mean field approximation, and the Hamiltonian of Hubbard model will have the approximate form

$$H = K + U \sum_{i} [\langle n_{i\downarrow} \rangle n_{i\uparrow} + \langle n_{i\uparrow} \rangle n_{i\downarrow}] \tag{2.27}$$

The self-consistent loop will be conducted as follows. First, we make an arbitrary initial trial wave function (e.g. the non-interacting trial wave function), we perform AFQMC with it and measure the observable $\langle n_{i\sigma} \rangle$ using AFQMC, then we feed back these values into equation 2.28 to generate a new trial wave function, which is used for the next step AFQMC calculation.

Since in the mean field approximation, the interaction between two particles are always over-estimated, we use $U_{eff}$ instead of $U$ in the self-consistent loop, where $U_{eff}$ is usually smaller than $U$. Equation 2.27 will have the form

$$H = K + U \sum_{i} [U_{eff} \langle n_{i\downarrow} \rangle n_{i\uparrow} + \langle n_{i\uparrow} \rangle n_{i\downarrow}] \tag{2.28}$$

The $U_{eff}$ is determined in the self-consistent process to make the densities of mean field solution as close to the AFQMC results as possible. In other words, we vary $U_{eff}$ to minimize the following terms:

$$\delta = \sum_{i,\sigma} |\langle \hat{n}_{i,\sigma} \rangle_{IP} - \langle \hat{n}_{i,\sigma} \rangle_{QMC}| \tag{2.29}$$

After equilibrium, the $U_{eff}$ value and QMC densities will converge, and the results will be more accurate. In next chapter, we will use an example to illustrate this.

There is another approach for constructing the trial wave function by the input value of AFQMC in the self-consistent procedure. We obtain the one-body density matrix $\rho^{QMC}$, and in order to find a Slater-determinant that closest to the density matrix, we diagonalize

$\rho^{QMC}$ to produce natural orbitals. Practically, we can make the density matrix Hermitian by averaging the original matrix and its conjugate transpose. The diagonalizition procedure can be written as:

$$\frac{1}{2}[\rho^{QMC} + (\rho^{QMC})^{\dagger}] = V\Lambda V^{\dagger} \tag{2.30}$$

$\Lambda$ is the diagonal matrix whose eigenvalues are arranged from smallest to largest, and $V$ are eigenvectors arranged correspondingly to the eigenvalues of $\Lambda$. We take the $N_\sigma$ leading eigenvectors in V corresponding to the $N_\sigma$ largest eigenvalues to construct the Slater-determinant for the trial wave function. Up electrons and down electrons are calculated separately.

The results turn out to be very similar to the self-consistent approach mentioned before, which will be illustrated in the next chapter.

# CHAPTER 3

# Ground state phase diagram of the 2D repulsive pure Hubbard model

In this chapter, we will have a detailed investigation in spin and charge density of the ground state of 2D doped Hubbard model in its simplest form ($t' = 0$), using the methods mentioned in the chapter 2. We will systemically this model as a function of interaction strength $U$ and doping $\delta$, and with carefully finite size scaling, we map out the ground state phase diagram in terms of spin and charge order.

## 3.1 Benchmark example

We first take the $20 \times 4$ cylinder with $U = 6$ and $h = 0.1$ as an example to illustrate the method and provide a sense of its procedure and accuracy. For a narrow cylindrical system such as this one, DMRG [43, 44] can provide highly accurate results for benchmark. A pinning field is applied at the edges of the cylinder to induce local antiferromagnetic order: $v_{i\downarrow} = -v_{i\uparrow} = \frac{1}{2}(-1)^{i_x+i_y} v_p$ for $i_x = 1$ and $i_x = L_x$. The strength of the pinning field is $v_p = 0.5$ here.

The result for the staggered spin density is shown in Fig. 3.1. We start the self-consistent iteration with the free-electron ($U_{\text{eff}} = 0$) trial wave-function. The energy from the free-electron trial wave-function is $-66.82(1)$, which is very close to the exact (DMRG) energy of $-66.74(1)$. However, the staggered spin density from the free-electron trial wave-function displays some significant discrepancies with respect to the exact result as seen in Fig. 3.1. As detailed in [29], we set up a self-consistent loop which uses the CP-AFQMC solution to determine a mean-field solution with an effective $U$, $U_{\text{eff}}$, which minimizes the difference between its density (or density matrix) and that from AFQMC. This solution (which has broken spin symmetry) is used as the new trial wave function, and the process is iterated to convergence. After 6 iterations, the CP-AFQMC results are indistinguishable from the exact results, consistent with previous studies [29]. The result for hole density is shown in Fig. 3.2. There is still noticeable discrepancy in the converged local hole densities, but the pattern is the same as the exact DMRG results.

It can be also shown that natural orbital self-consistent methods, which generates next step trial wave function by whole density matrix diagonalization, get the similar results as our original method. Fig 3.3 shows the difference between two self-consistent iteration method, their values have a tiny discrepancy, but both spin and charge pattern are exactly the same. These two methods can be considered equivalent in many cases.

In Fig. 3.4, we study the effect of the strength of the pinning field on the results. The system is a $32 \times 6$ cylinder with $U = 6$ and $\delta = 1/8$. Pinning fields are applied on the two edges, similar to the setup in the previous example. The strength of pinning field, $v_p$, is now varied by a factor of 4, from 0.2 to 0.8. We see that both the staggered spin density and hole density remain nearly the same in the "bulk" of the system. This validation shows the viability of probing long-range order with local pinning fields (provided that sufficiently large system sizes can be studied).

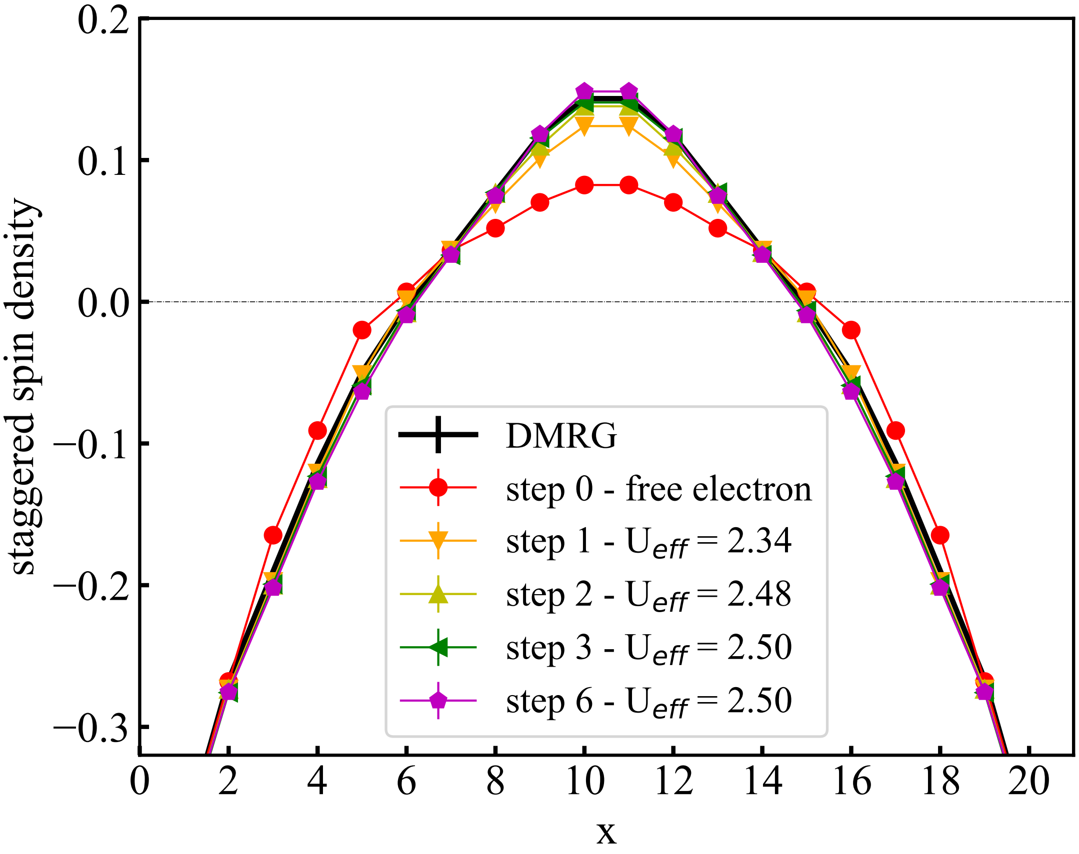

FIG. 3.1: The staggered spin density $(-1)^{i_x+i_y}S_z(i)$ along $x$-direction for $20 \times 4$ system with 1/10 doping and $U = 6$ in the self-consistent CP-AFQMC calculation. Results are averaged over different rows ($i_y$ values). After convergence, the CP-AFQMC result agrees well with the accurate DMRG results (black line).

We have also tested the case with charge pinning field alone and simultaneous spin and charge pinning field, the results are consistent with those obtained with spin pinning field only. An example is shown in Fig. 3.5

## 3.2 Finite size scaling

At each set of system parameters ($U$, $h$), we probe the order in a range of (large) lattice sizes. A true ground-state long-range order will persist with increasing system size,

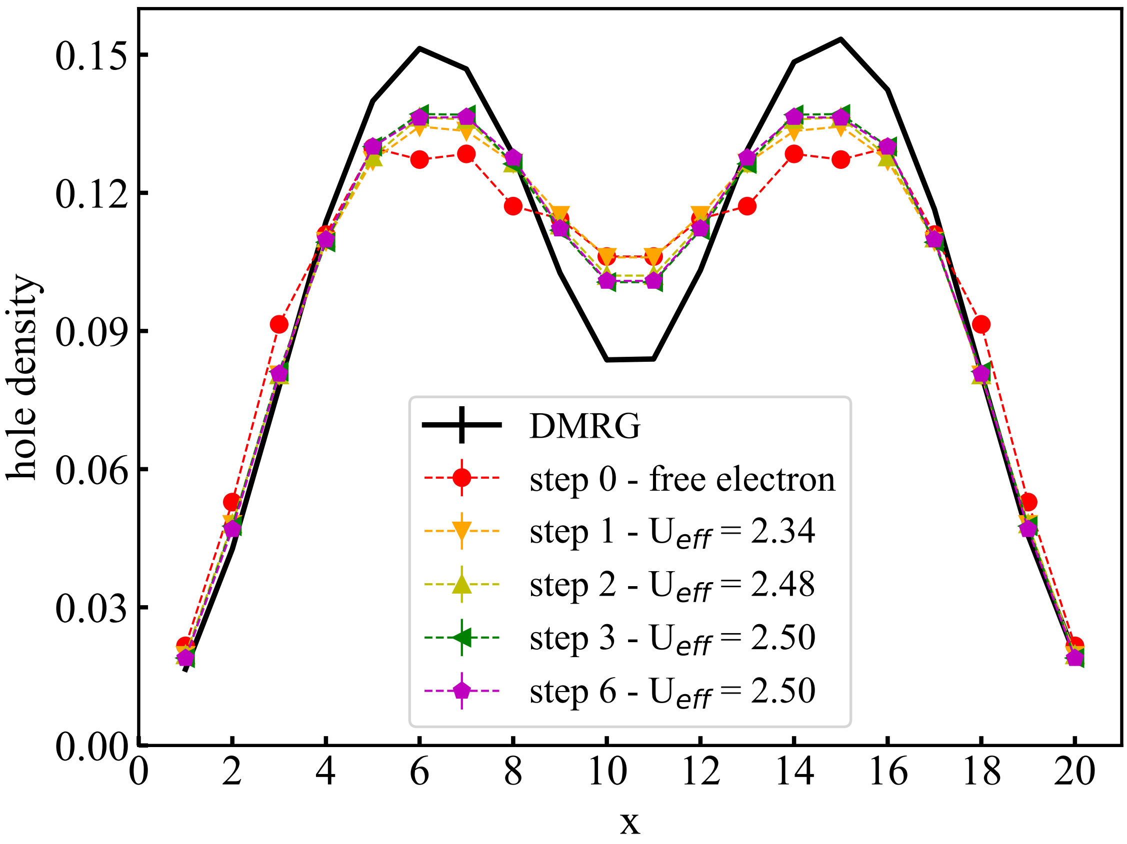

FIG. 3.2: The corresponding hole density in the same system as in Fig. 3.1: $20 \times 4$ cylinder with 1/10 doping and $U = 6$. There is noticeable discrepancy in the self-consistent CP-AFQMC hole density from the accurate DMRG result (black line). However the stripe structure is the same.

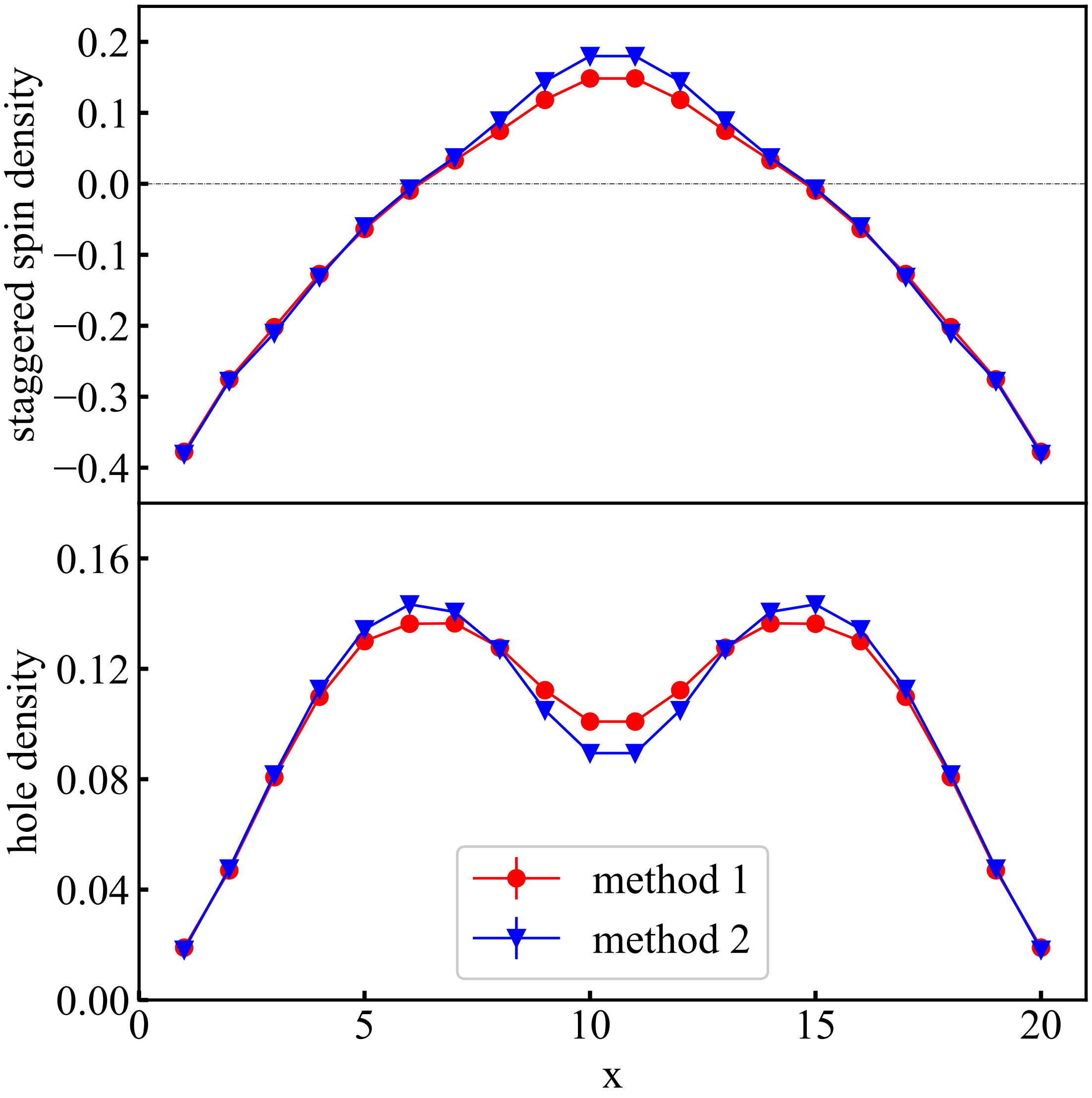

FIG. 3.3: Insensitivity of the long-range order to the choice of self-consistent method. Method 1 is the independent particle self-consistent method, and method 2 is the natural orbital self-consistent method. Although two results have a little discrepancy in spin and charge density, they get exactly the same spin and charge pattern.

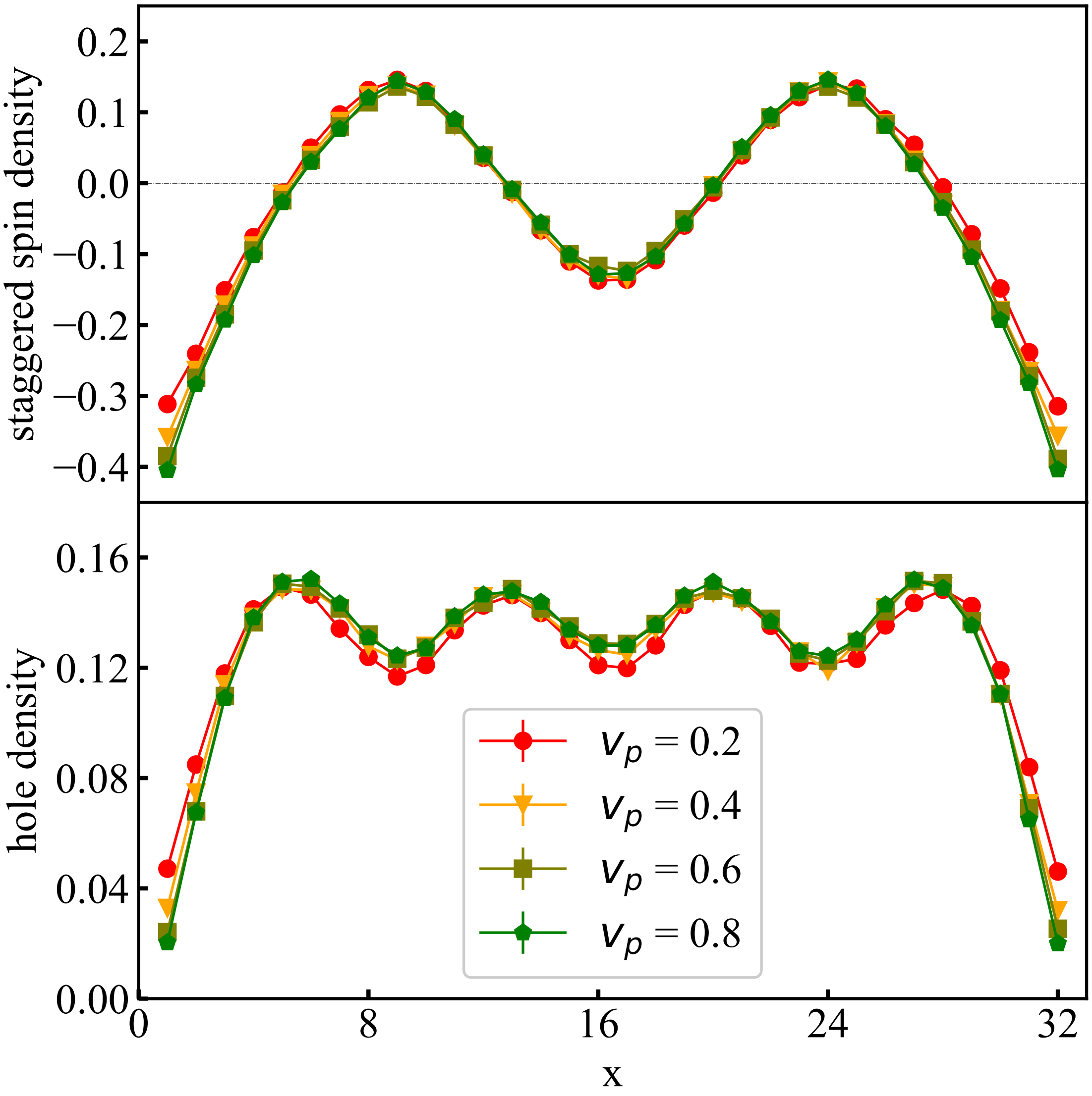

FIG. 3.4: Insensitivity of the long-range order to the strength of the spin local pinning field. Staggered spin density (up) and hole density (down) are shown for a $32 \times 6$ cylinder with $1/8$ doping and $U = 6$. The strengths of the pinning field ranges from 0.2 to 0.8. Converged results from self-consistent CP-AFQMC are shown for each system. The pinning field has little effect on the spin and hole density, especially in the "bulk" of the system.

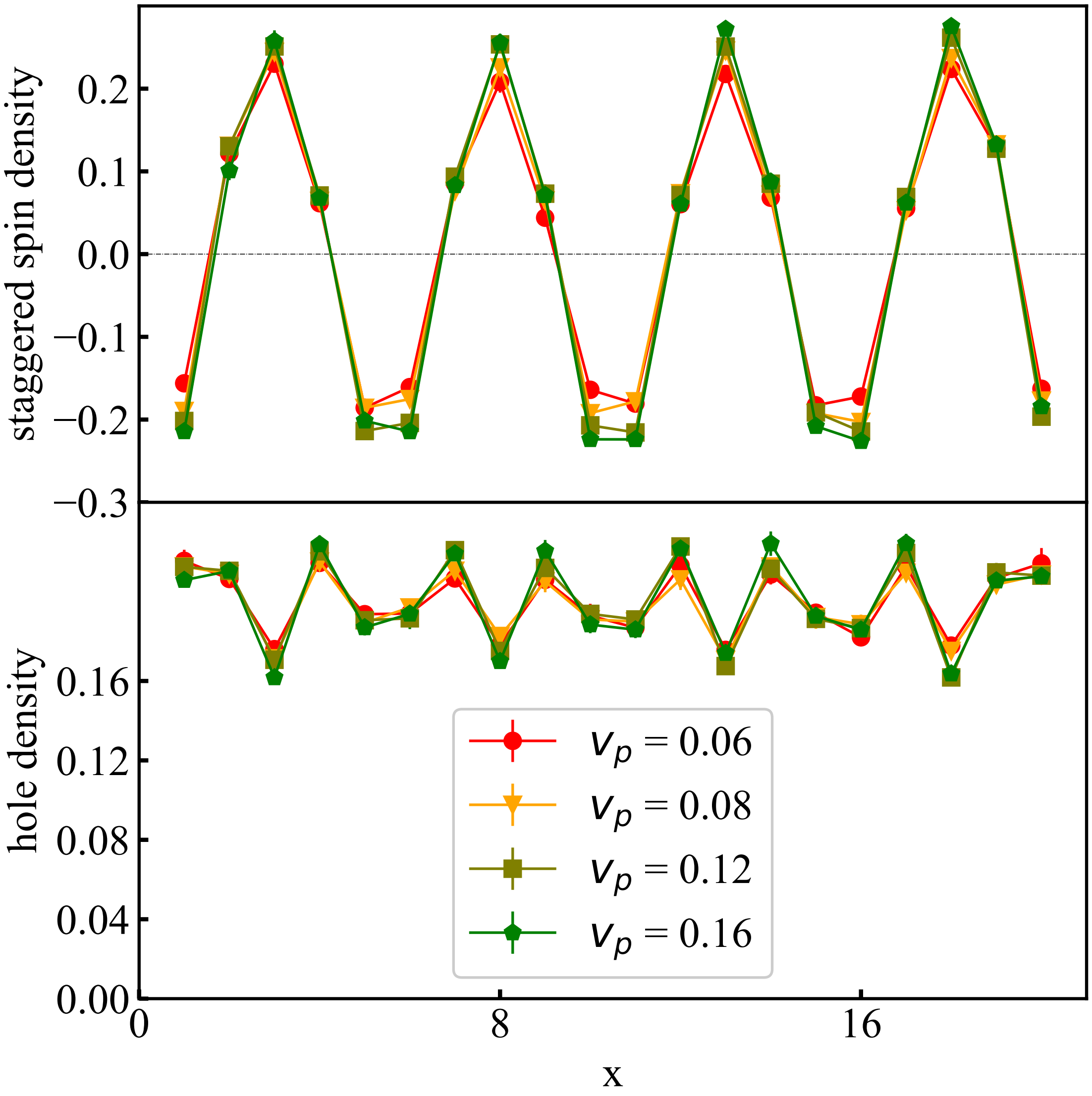

FIG. 3.5: Insensitivity of the long-range order to the strength of the local pinning field. Staggered spin density (up) and hole density (down) are shown for a $32 \times 6$ cylinder with 1/8 doping and $U = 6$. The strengths of the pinning field ranges from 0.2 to 0.8. Converged results from self-consistent CP-AFQMC are shown for each system. The pinning field has little effect on the spin and hole density, especially in the "bulk" of the system.

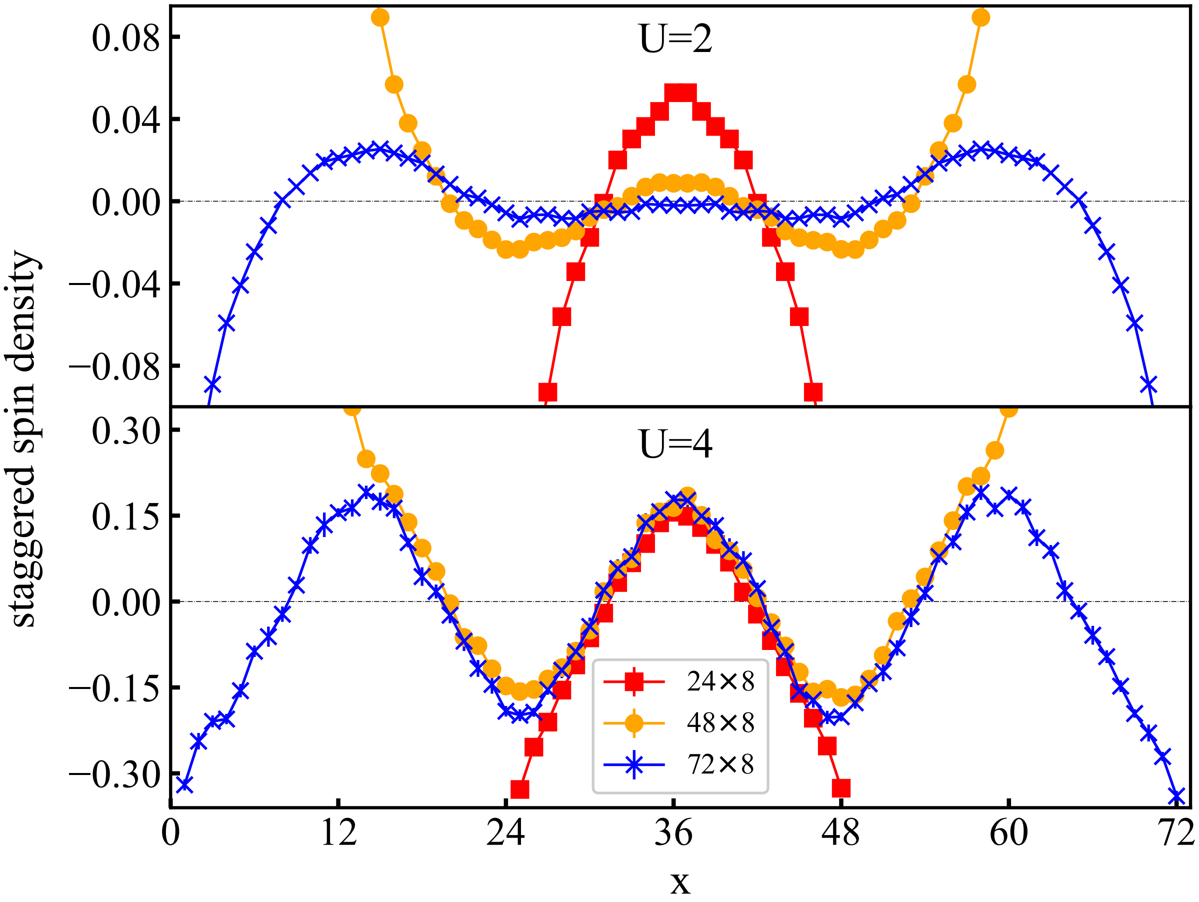

FIG. 3.6: Presence and absence of long-range order with supercell system size. The staggered spin density is shown for two interaction strengths, $U = 2$ (top) and $U = 4$ (bottom), at $h = 1/12$ doping, each for a sequence of supercell sizes. All results are for cylinders with width 8, and the staggered spin densities are plotted along the long ($x$) direction. As the length of the cylinder is increased, the staggered spin density vanishes for $U = 2$ but remains a constant for $U = 4$.

while a short-range correlation induced by the local pinning field will die out as the system size grows. This is shown in Fig. 3.6, in which the spin orders are computed in width-8 cylinders at $\delta = 1/12$ doping, with $U = 2$ and $U = 4$, respectively. At $U = 2$ the spin density in the "bulk" of the system appears to tend to zero as the length of the system is increased, while it is almost unchanged at $U = 4$ for $L_x$ from 24 to 72, displaying a spin-density wave (SDW) with a consistent wavelength.

As a more quantitative probe of the order, we calculate the spin structure factor $S_s(\mathbf{k}) = \frac{1}{N}\sum_{\mathbf{r}_i} e^{i\,\mathbf{k}\cdot\mathbf{r}_i}\langle n_{i\uparrow} - n_{i\downarrow}\rangle$, where $\mathbf{k} = (k_x, k_y)$, with $k_x = n_x\, 2\pi/L_x$ and $k_y = n_y\, 2\pi/L_y$ ($n_x \in [0, L_x)$ and $n_y \in [0, L_y)$ are integers). The results are shown in Fig. 3.7. At $U = 4$, a peak is seen in the spin structure factor at $\mathbf{k}_p = ((1-\delta)\pi, \pi)$, i.e., $(\frac{11}{12}\pi, \pi)$ in this case, which agrees with the wave-length of the SDW in Fig. 3.6. The height of the peak grows with the system size, and saturates among the larger supercells. At $U = 2$, a smaller peak is also present at $\mathbf{k}_p$. However, the value of the peak decays as system size $L_x$ is increased.

We next perform a finite size scaling of the values of the spin structure factor at $\mathbf{k}_p$ (the peak position). In order to reach the TDL, we extrapolate $S_s(\mathbf{k}_p)$, first as a function of the width($L_y$) of the system, followed by an extrapolation as a function of the length($L_x$). This procedure is shown in Fig. 3.8. At $U = 2$ (left panel), the extrapolated values for $L_x = 24, 48$, and 72 are $0.060(1), 0.029(5)$, and $0.018(3)$ respectively, while at $U = 4$ (middle panel), the corresponding values are $0.120(5), 0.117(6)$, and $0.125(3)$. Extrapolations of these results with $L_x$ yield the following values of the spin structure factor at the TDL: $-0.003(5)$ at $U = 2$ and $0.123(9)$ at $U = 4$. From these results we conclude that, for doping $\delta = 1/12$, a spin order is absent at $U = 2$ but present at $U = 4$. (These two points are indicated as points A and B in the phase diagram in Fig. 3.12.) We systematically apply this procedure to determine the presence of order for each set of Hamiltonian parameters, hence an estimate of the critical interaction strength $U_c$ for the appearance of an SDW or stripe order, and map out a phase diagram for $U \lesssim 12$.

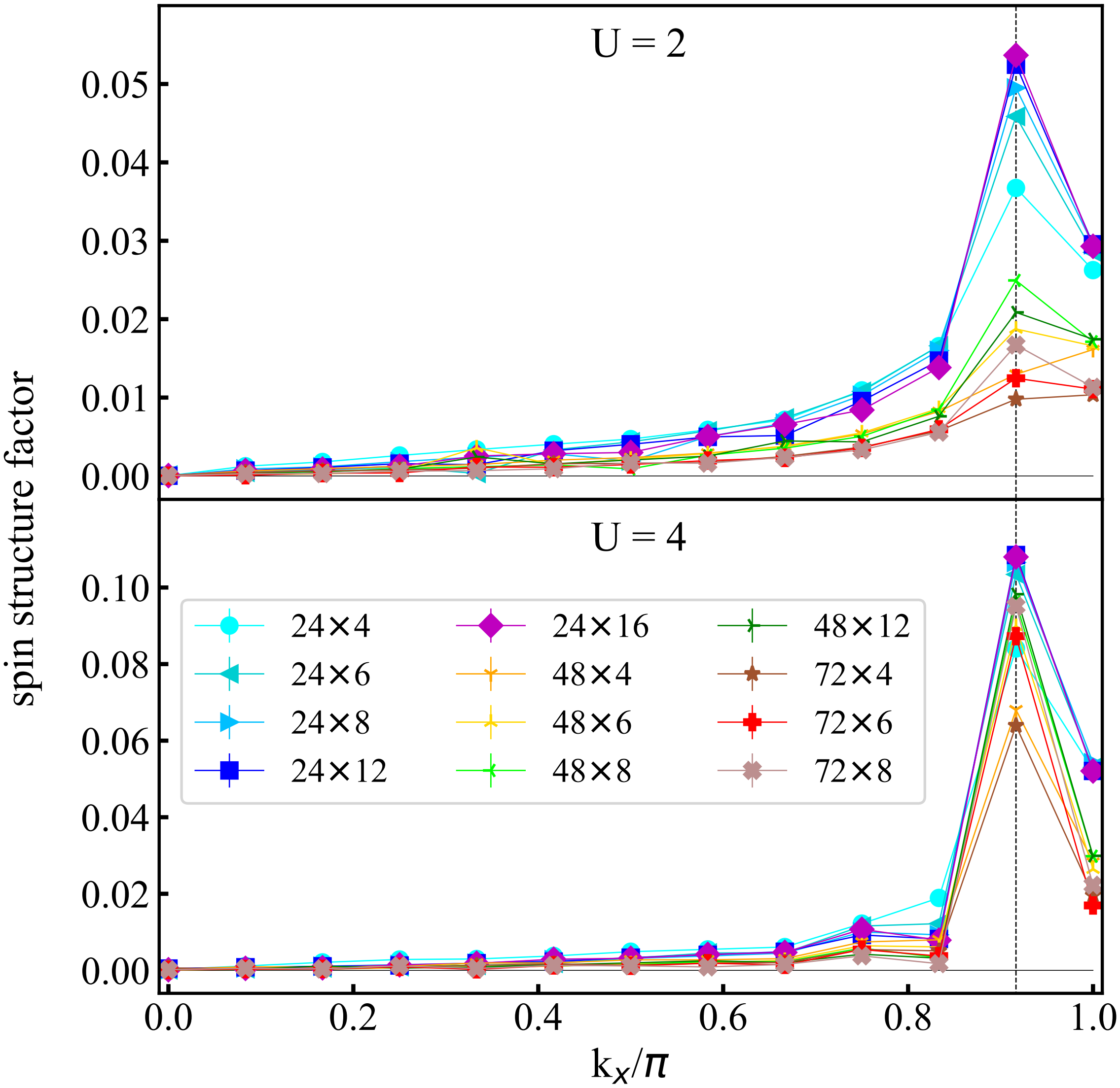

FIG. 3.7: Spin structure factor $S_s(k_x, \pi)$ for a variety of simulation cell sizes, at two interaction strengths, $U = 2$ (top) and $U = 4$ (bottom). All systems are at $\delta = 1/12$ doping. A peak is seen at $k_x = \frac{11}{12}\pi$. With the increase of systems size, the peak descreases and vanishes at $U = 2$ but increases and saturates at $U = 4$. Note the different vertical scales in the two panels.

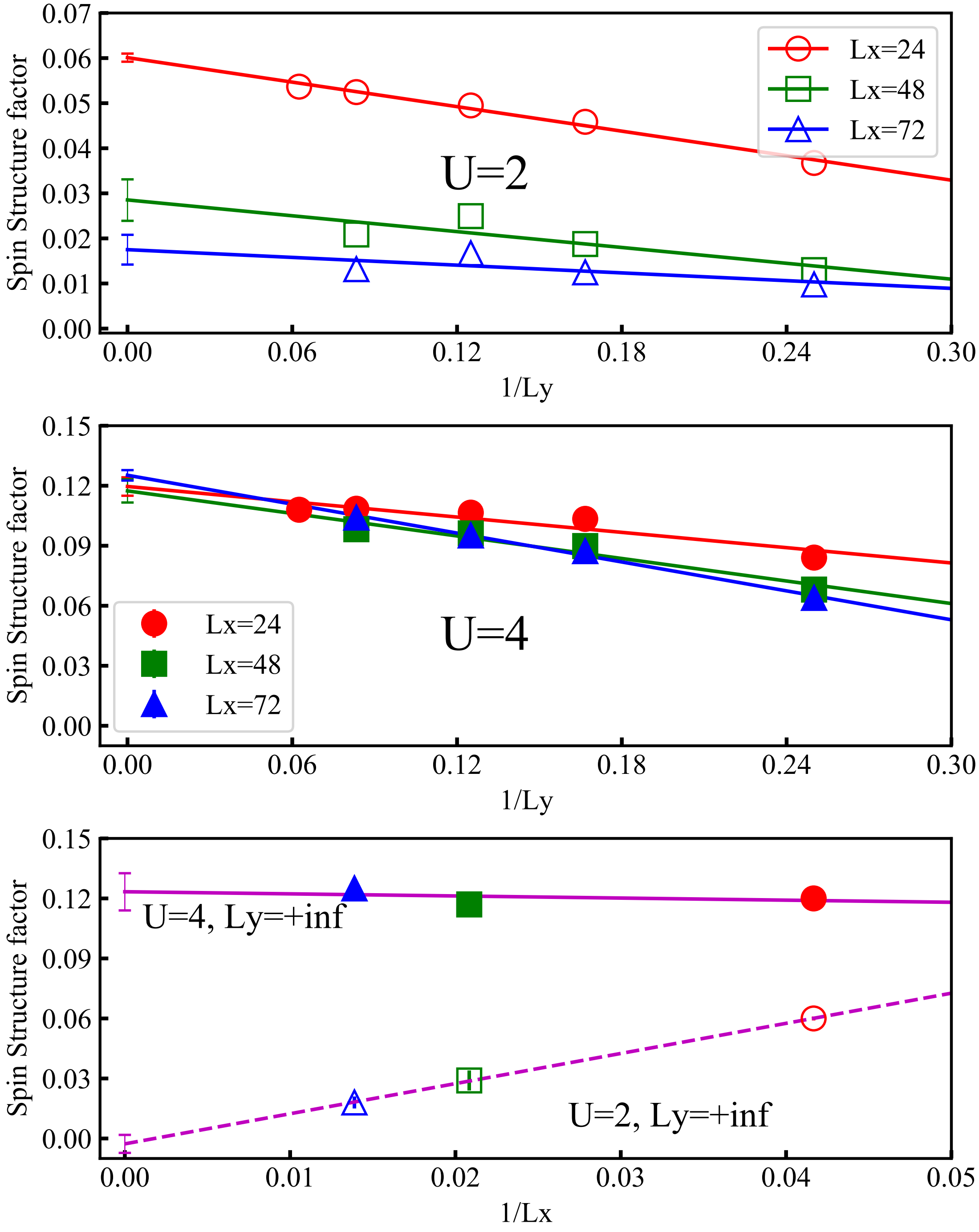

FIG. 3.8: Finite size scaling of the spin structure factors in Fig. 3.7. An extrapolation with $L_y$ is performed for each set of cylinders with the same length, shown in the left panel for $U = 2$ and middle panel for $U = 4$. This is followed by an extrapolation with respect to the length of the cylinders, $L_x$, shown in the right panel for both $U$ values. At the TDL, the peak value of the spin structure factor vanishes for $U = 2$, while it reaches a finite value for $U = 4$.

## 3.3 Determining the wavelength of the collective modes

We find that a modulated spin order appears for doping values up to about $\delta \sim 1/5$, often accompanied by charge orders. We will further discuss the properties of these collective modes and provide a detailed phase diagram below.

Here we describe our investigation of the wavelength of the collective mode in the spin and charge order in the ground state. We first illustrate the procedure using the case of $\delta = 1/12$ and $U = 4$ as an example. In Fig. 3.9, we vary the length of the cylinder (hence also $N_e$, in order to maintain the same $\delta$) while keeping the width fixed at $L_y = 6$. A pinning field of strength $v_p = 0.5$ is applied only at the left edge ($i_x = 1$) and periodic boundary condition (PBC) is used along x direction. For y direction, twist average boundary condition (TABC) is used to further reduce the finite size effects [45]. From Fig. 3.9, we see that the staggered spin density becomes strongest, and frustration is minimized when $L_x = 24$. The corresponding charge order also forms a regular wave with hole density peaks at the nodal position of the spin order. This is consistent with a wavelength of $2/\delta$ for the SDW and $1/\delta$ for the CDW. At larger interaction strengths, the SDW evolves into a stripe order [15], and our results suggest that the stripes are filled. We use this procedure, combined with finite-size scaling as discussed in Sec. 3.2, to establish the order in the TDL and determine its wavelength. More examples are shown in the appendix.

Recent studies from DMRG [46] and the minimally entangled typical thermal states (METTS) [27] methods have found half-filled stripes in width-4 cylinders. For example, at $U = 12$ half-filled stripes are identified as the ground state for all doping values below $\sim 1/9$ [46], while from METTS $\delta = 1/16$ at $U = 10$ is seen to exhibit half-filled stripe order at very low temperatures [27]. Our calculations suggest that, in the pure Hubbard model, the half-filled stripe state appears to be special to width-4 cylinders, and we see filled stripes become the ground state in wider cylinders. In Fig. 3.10, we show an example of $\delta = 1/12$ and $U = 12$, in four different simulation cells — two with-4 cylinders, $24 \times 4$ and $48 \times 4$, and two width-8 cylinders $24 \times 8$ and $48 \times 8$. Each calculation is performed following the same procedure that we have outlined. We see that the half-filled stripe is indeed the ground state for width-4 cylinders upon convergence of the self-consistent AFQMC. For width-8 cylinders, however, the ground state corresponds to filled stripes. We also compare the computed energies of half-filled and filled stripes at $U = 12$ and $\delta = 1/12$ in Table. 3.3. We find that the energy for half-filled stripe is lower than that of the filled stripe in width-4 systems but this trend is reversed in width-8 systems. These results indicate that the half-filled stripes in width-4 cylinder are affected by finite size effects, and the stripe are filled at the TDL.

Recent studies in larger cells, for example using variational Monte Carlo [20], have suggested that the spin order might show wavelengths of $\alpha/\delta$, where $\alpha$ is neither 1 (half-filled) nor 2 (filled), for instance displaying a metallic state with $\alpha$ being a fraction. We searched in a few such cases but did not find a stripe state with fractional $\alpha$. Below we show an example at $U = 8$ and $\delta = 1/12$. We computed the energies using trial wave functions with several different wavelengths, without invoking the self-consistency loop in the constraint. (In these cases the QMC results turned to stay with the same wavelength, indicating that such a state is close in energy to the true ground state, as seen from the results below.) PBC is applied along both directions and the pinning field is removed, in order to allow direct comparison of the energies. As seen in Table 3.3, in the $48 \times 6$ lattice, the energy from the 2/3 filled stripe state ($\lambda = 8$) is slightly lower than filled stripe state ($\lambda = 12$), and both state are lower than half-filled stripe state ($\lambda = 6$), which is consistent with the result obtained in Ref. [20]. (Note that the best variational wave function gives an energy that is $\sim 0.013t$ per site higher.) In the $48 \times 8$ lattice, the energies of the filled and 2/3 filled stripe state are almost degenerate. We next performed a calculation with a trial wave function constructed from a linear combination of all three states, and the result is a filled stripe state. We thus conclude that, to within our resolution, the ground state is a filled stripe state.

There are other systems with different doping provide the same conclusion above, these result are included in the appendix A.

| lattice | half-filled stripe | filled stripe |
|---|---|---|
| $24 \times 4$ | -0.5639(1) | -0.5630(1) |
| $48 \times 4$ | -0.5583(2) | -0.5569(2) |
| $24 \times 8$ | -0.5596(2) | -0.5613(2) |
| $48 \times 8$ | -0.5532(2) | -0.5541(2) |

TABLE 3.1: Comparison of the computed total energies (per site) in the half-filled and filled stripe states at $U = 12$ and $\delta = 1/12$, in cylinders with widths 4 and 8, and lengths 24 and 48. The system setup is the same as in Fig. 3.10. Half-filled stripe state has lower energy in width-4 systems but higher energy in width-8 systems. A correction has been applied to the energies to account for finite Trotter step size [1].

| lattice | $\lambda = 6$ | $\lambda = 8$ | $\lambda = 12$ |
|---|---|---|---|
| $48 \times 6$ | -0.6820(2) | -0.6862(2) | -0.6855(2) |
| $48 \times 8$ | -0.6821(2) | -0.6854(2) | -0.6852(2) |

TABLE 3.2: Comparison of the energy per site in the half-filled ($\lambda = 6$), 2/3 filled ($\lambda = 8$) and filled ($\lambda = 12$) stripe states at $U = 8$ and $\delta = 1/12$ in two different lattice sizes. Fully periodic supercells are studied here, with no pinning fields. Half-filled stripe state has the highest energy in both systems. The 2/3-filled stripe state has the lowest energy in the width-6 supercell, while its energy is indistinguishable from that of the filled stripe state in the width-8 supercell. Both self-consistency and the use of a linear combination of trial wavefunctions with different stripe fillings lead to the filled stripe state as the ground state.

## 3.4 Phase diagram

Using the procedure described in the previous section, we map out the phase diagram of the spin and charge orders in the ground state of the pure two-dimensional Hubbard model ($t' = 0$) in the TDL, from weak ($U \sim 0$) to fairly strong ($U \sim 12$). The results are summarized in Fig. 3.12. We find that, up to a doping value of $\delta \sim 0.2$, there exists

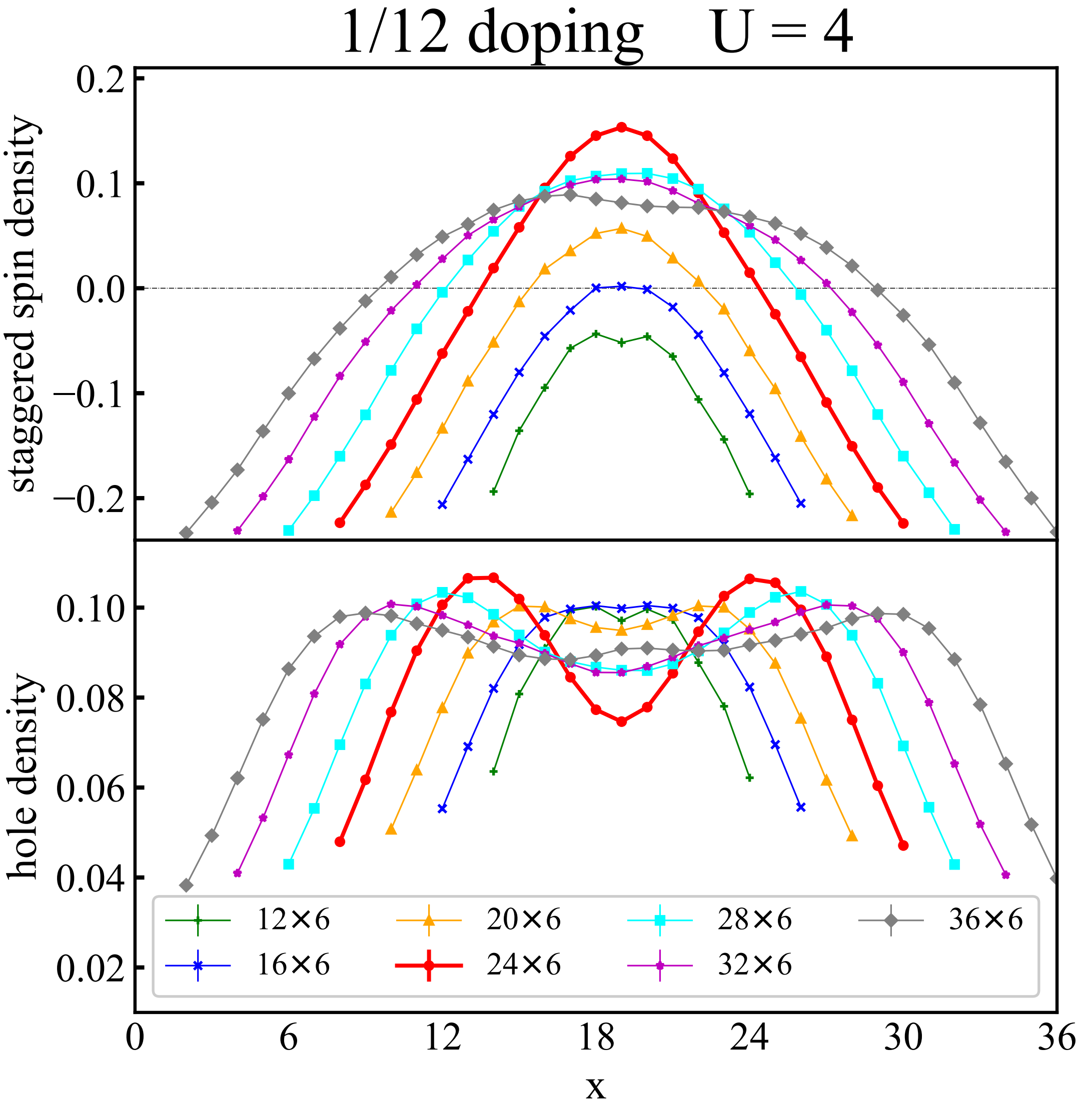

FIG. 3.9: Staggered spin (top panel) and hole (bottom) densities at $\delta = 1/12$ doping and $U = 4$, in width-6 cylinders as the length $L_x$ is varied. Results are omitted at the left edge ($i_x = 1$), where the pinning field is applied. When $L_x$ is commensurate with the expected wavelengths for spin and charge orders ($1/\delta$ and $2/\delta$), the spin and charge density waves are least frustrated and have the largest amplitude.

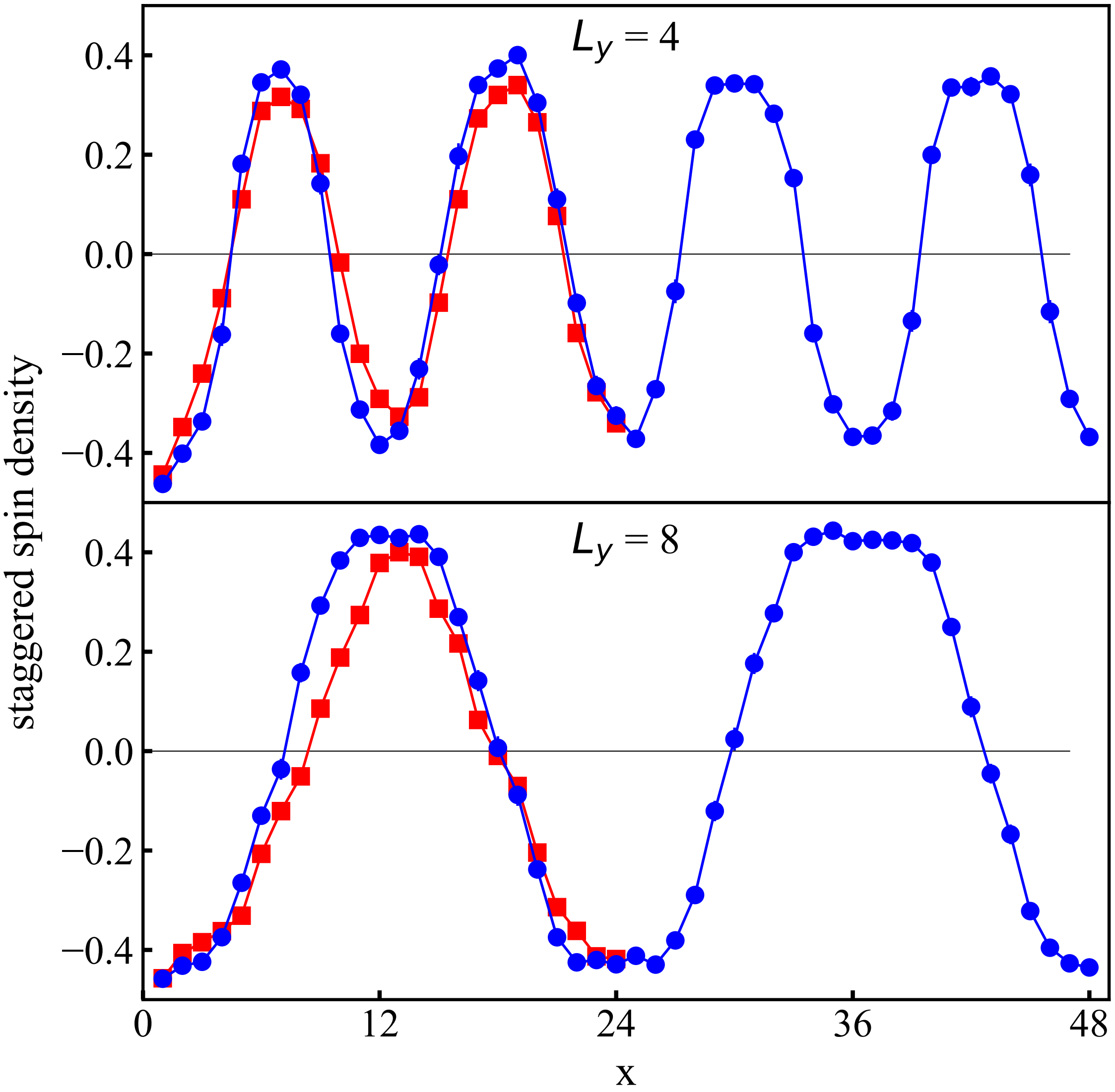

FIG. 3.10: Different behaviors in width-4 (top panel) and width-8 (bottom) cylinders. Staggered spin densities are shown for $\delta = 1/12$ doping with $U = 12$. The red curves show results for cylinders of length $L_x = 24$, while the blue curves show those with $L_x = 48$.

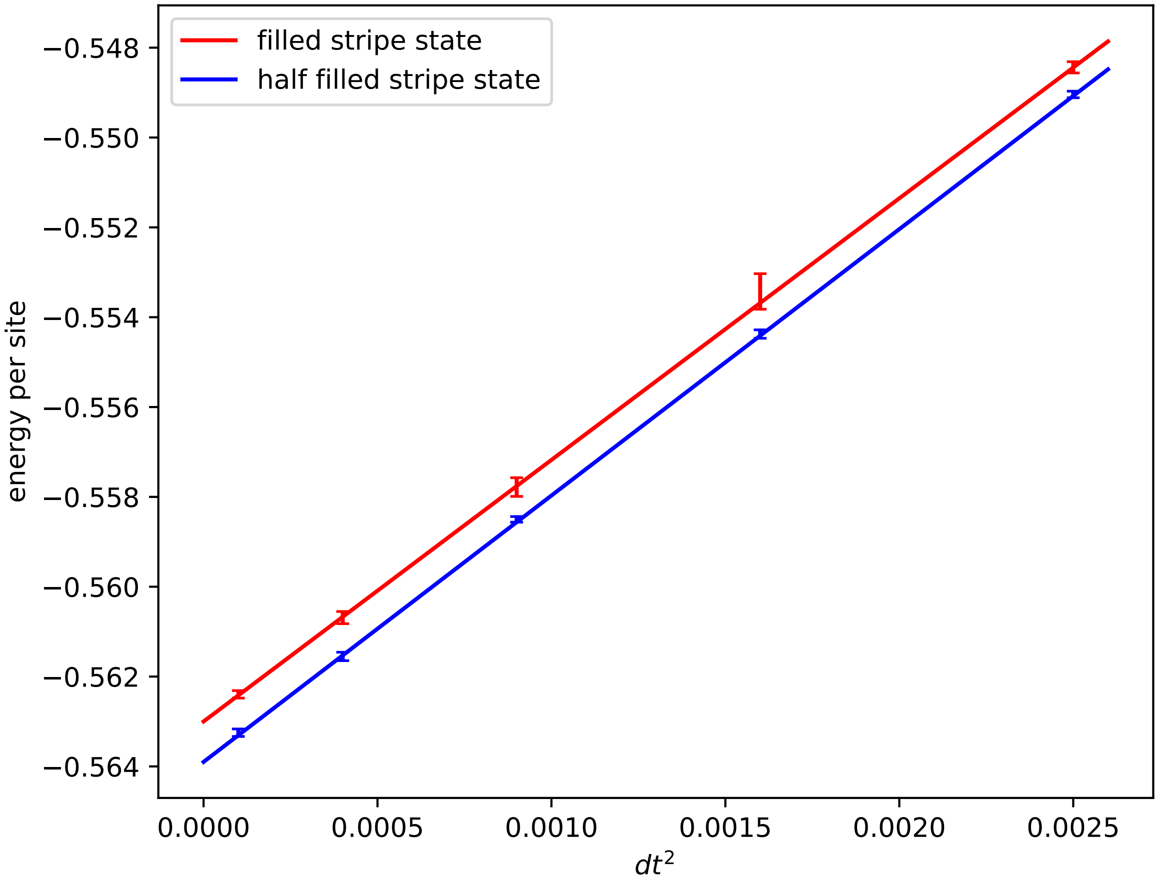

FIG. 3.11: Example of energy per site calculation with different $\Delta\tau$ in $24 \times 4$ lattice, U=12, 1/12 doping. By the linear extrapolation of the result with $\Delta\tau^2$, we can greatly reduce the Trotter error and get more precise energy calculation.

a critical interaction strength $U_c(\delta)$, above which the system exhibits a collective mode of a modulated AFM order. The spin order has wavelength $2/\delta$, and is accompanied by a charge order of wavelength $1/\delta$, in which the hole density tends to be higher at the nodes of the spin order.

At weaker $U$ (above $U_c(\delta)$) or larger doping, the charge order is weak. In these states the hole density is not vanishingly small at the node of spin order; in fact the hole density remains substantial throughout space and only shows a slow-varying wave with modest peaks at the nodes of the modulated AFM. We have referred to such states as SDWs (which can have charge order). As the interaction strength is increased and the doping is reduced, the SDW states evolve into stripe states, where the holes become more and more localized at the nodes. The distinction between the SDW and stripe states is not absolute, but it is important to emphasize that a modulated AFM order can exist with two different kinds of behaviors for the holes: mobile and wavelike vs. localized and particle-like [15].

In Fig. 3.12, green squares represent parameters which lead to a ground state with SDW or stripe order in the TDL, while red circles represent those which do not. Within Hartree-Fock diagonal stripes are found to be more stable than linear (along $x$- or $y$-direction) stripes at large $U$ [3]; diagonal stripes were also found to be close in energy with linear stripe state in the doped $t$-$J$ model [16, 47]. We searched for diagonal stripes in the Hubbard model in the parameter regime studied here, but did not find them to be the ground state. (More details are given in the appendix.) Note that results from an inhomogeneous dynamical mean-field theory (iDMFT) study [48] are in reasonable agreement with our results.

Based on our results, we show an estimate for the phase boundary as a solid black line in Fig. 3.12, whose position is not to be taken literally but which is bracketed by the data points around it.

From the results, we see that the critical interaction strength $U_c(\delta)$ increase with the doping level $\delta$. Nothing special is seen around the doping value of $\delta = 1/8$. The SDW or stripe order persists from small doping near half-filling to doping level as large as 1/5.

As discussed in more detail in Sec. 3.3, we did not find phase separation or non-filled SDW/stripe orders which survived in our finite-size scaling procedure. This of course does not completely rule out such phases, because of the delicate nature of the different competing states and sensitivity to finite-size and other effects, as well as possible systematic errors in the calculation. However, it does provide a rather stringent screening of other possible states, given the high accuracy and extensive nature of these calculations. In the appendix B, we also investigate the possibility of existence of the diagonal stripe at small $\delta$ and large interaction.

Next we will show some examples of parameter scans of phase diagram. In Fig. 3.13, we show how the spin and charge orders evolve as a function of $U$ at fixed doping $\delta = 1/12$. The system is a cylinder with size $8 \times 48$. A modulated AFM order develops only when $U \geq 4$. Similarly, in Fig. 3.14, we show the results of a scan at fixed interaction strength $U = 6$, in systems of size $L_x \times 6$, with $L_x$ from 32 to 48 to accommodate 1/4, 1/8 1/10, and 1/12 doping. As can be seen, no order is present until $\delta \leq 1/8$.

Other than the stripe and spin density wave study of the pure Hubbard model, we also investigate the double occupancy, and the conductivity of Hubbard model. These results are included in the appendix C and D.

The computing is mostly carried out at the Flatiron Institute, with message passing interface (MPI). The estimated computational time various by several factors, the number of walkers, the system size, etc... The largest system we have conducted in the stripe study is $72 \times 12$, with $1/12 doping$ and $U = 4t$. The running time for each iteration is 32 hours, with 1024 cores and 2 walkers distributed on each core. Usually, It takes less than 30 minutes to run a small system like $16 \times 4$, and several hours to run a medium system like $32 \times 8$

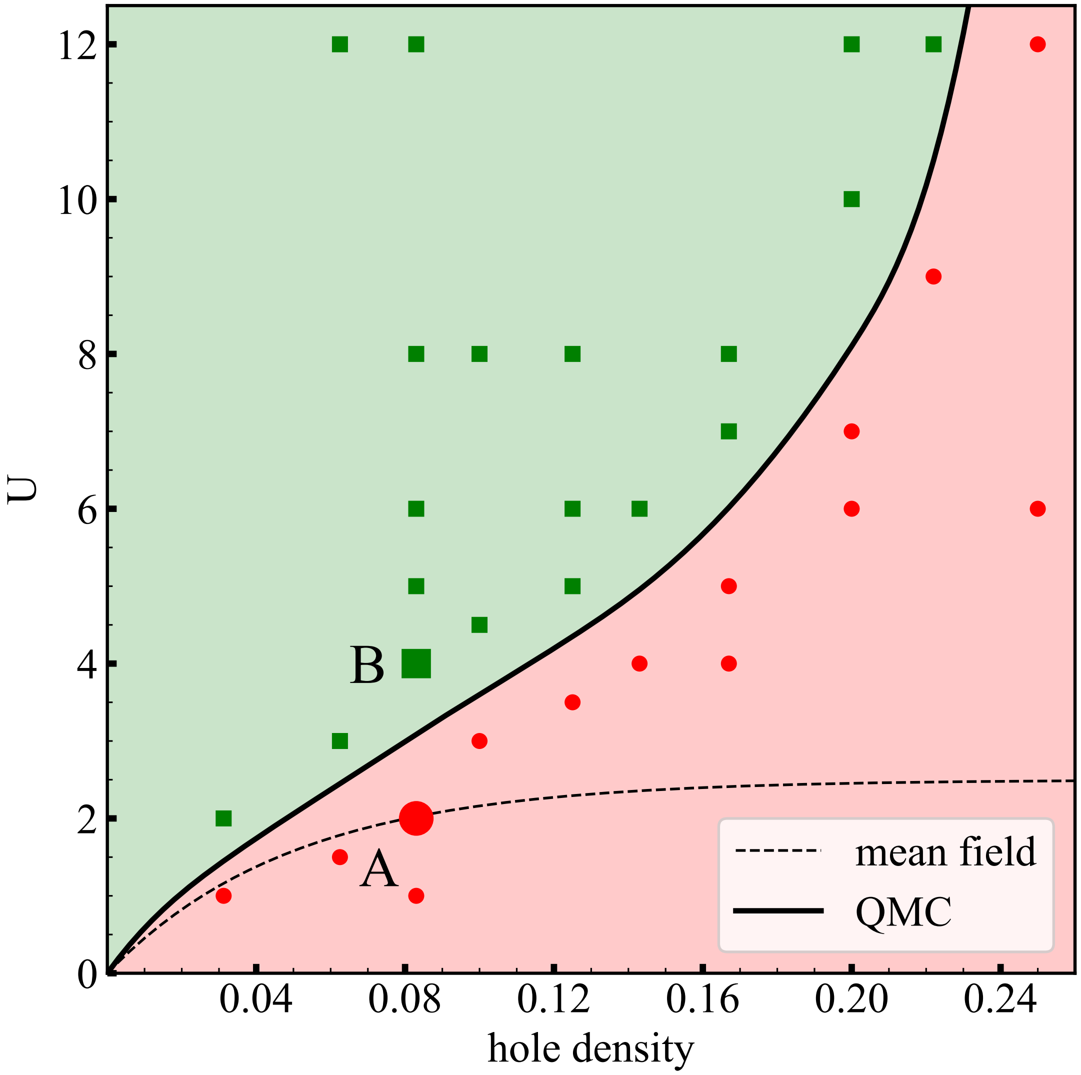

FIG. 3.12: Phase diagram of spin and charge orders in the pure Hubbard model. The black curve gives a rough estimation of the phase boundary based on the green squares representing parameters with modulated AFM spin and charge order and red cycles representing those without. The black dashed curve is the phase boundary from unrestricted Hartree-Fock [3] for reference. A ($U = 2$, $\delta = 1/12$) and B ($U = 4$, $\delta = 1/12$) denote the two examples shown in Figs. 3.6, 3.7, and 3.8.

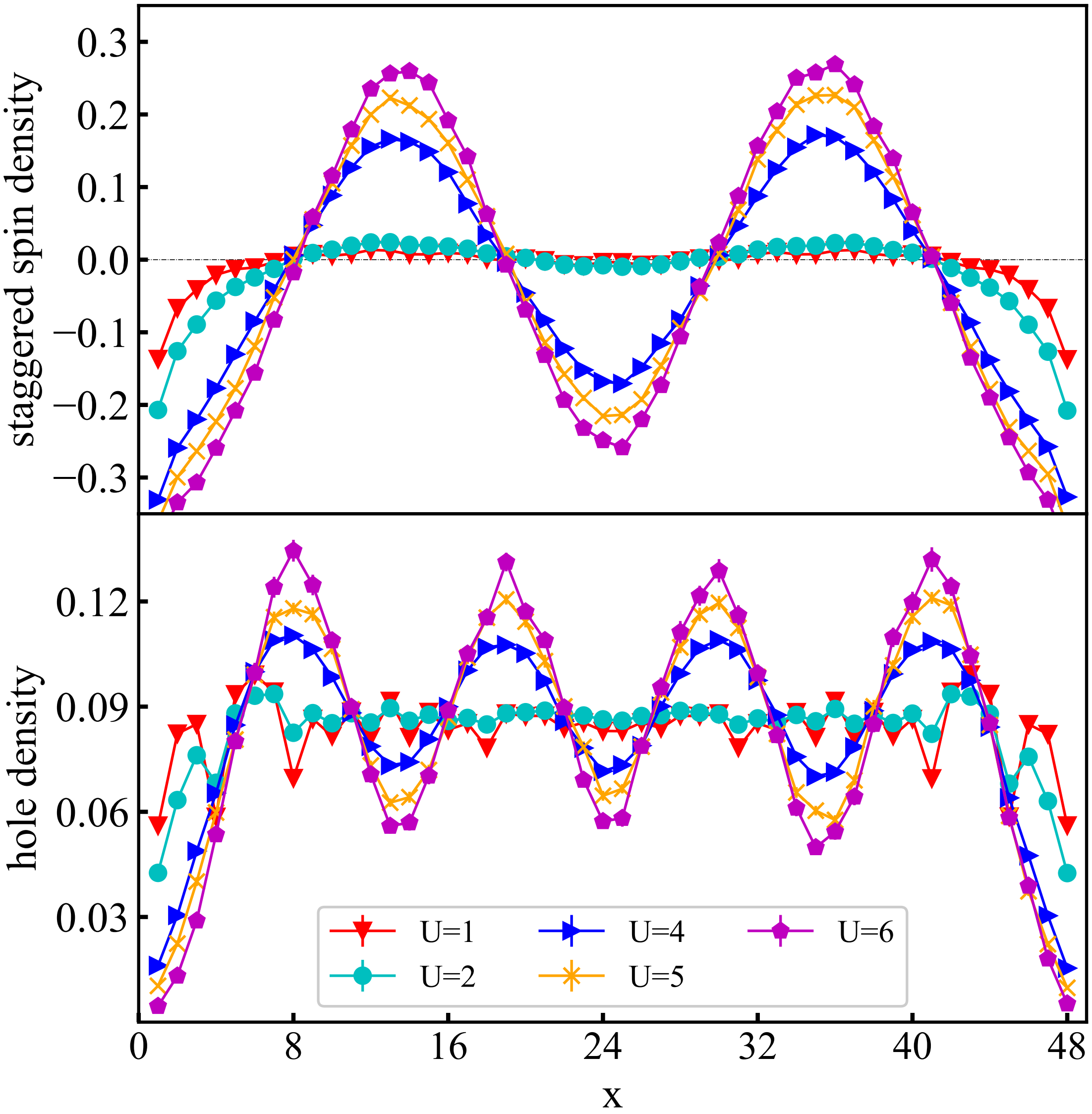

FIG. 3.13: Staggered spin (up) and hole (down) density at 1/12 doping for different $U$ values. We can find that the stripe order develops only with $U \geq 4$.

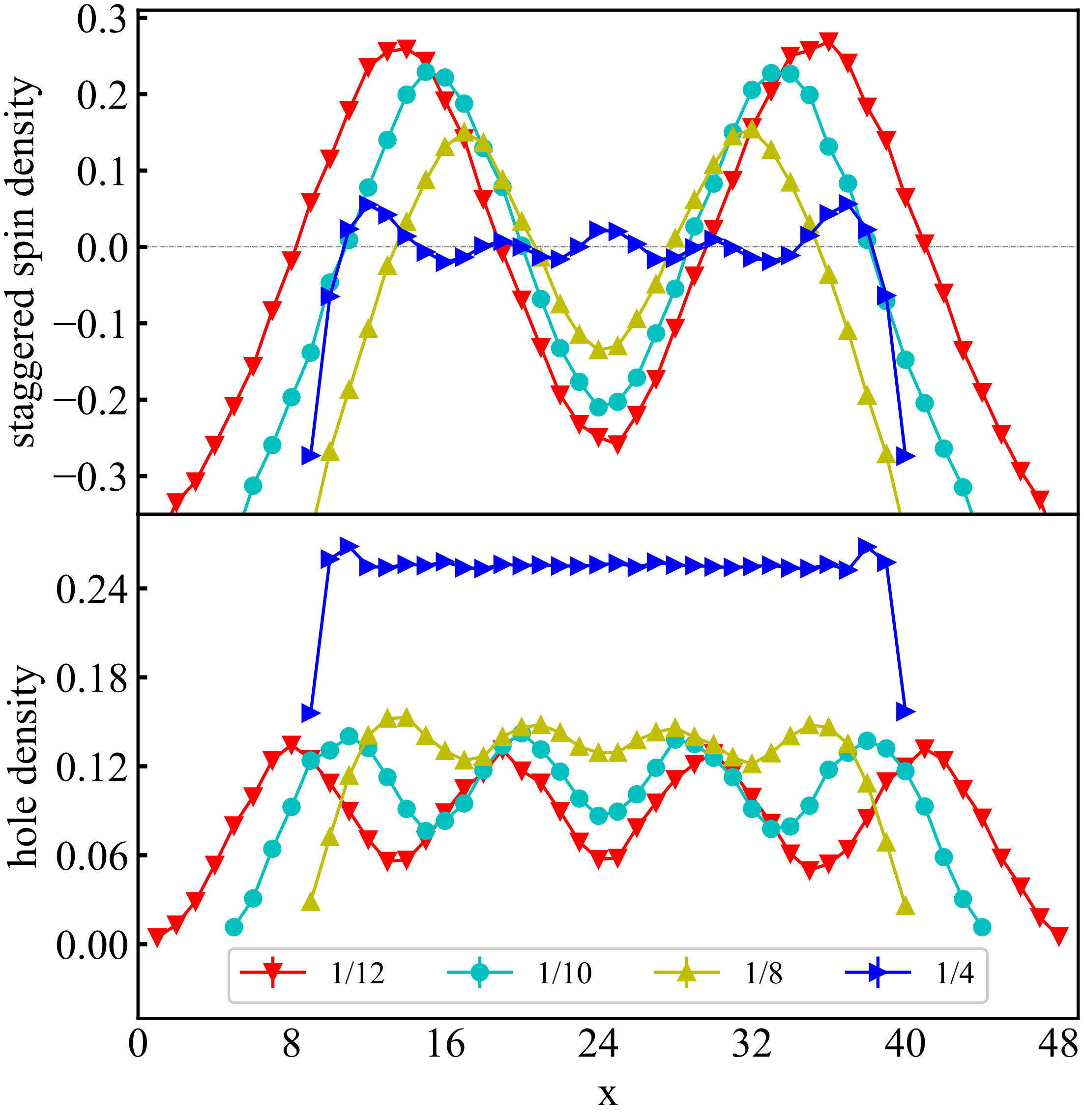

FIG. 3.14: taggered spin (up) and hole (down) density at $U = 6$ for different dopings. We can find that the stripe order only develops with $\delta \leq 1/8$.

# CHAPTER 4

# Superconductivity pairing order in Hubbard model with next nearest hoping

In the previous chapter, we focus mainly on the stripes and spin/charge density waves of the pure Hubbard model. In this chapter, following the previous study on superconducting pairing order of the pure Huubard model [33], we further investigate the superconducting pairing order of the $t'$ Hubbard model.

## 4.1 Computation of the pairing order parameter

The understanding of high-temperature superconductivity in materials, such as the cuprates, is of highly interest among theoretical condensed matter physicists. Hubbard model, along with its sister model, the t-J model [49], were argued to be paradigmatic models for the study of this problem in the early years. Many properties, like charge density waves which we studied carefully in the previous chapter, can be mirrored to the Hubbard model.

The long range order in superconductivity itself is a very delicate property that needs to be carefully treated. Highly accurate numerical methods are required, and that is why it is one of the greatest challenges in the modern condensed matter physics. The relationship between stripes and pairing is more subtle and controversial. Some studies give positive arguments about its co-existence with a stripes order [31, 50], while others advance counter arguments [51, 52]. In Mingpu Qin's paper, the $d_{x^2-y^2}$ wave superconducting order is actually short-ranged at the interaction and doping region related to cuprates[33], regardless of whether it has spin density wave or not in the thermal dynamic limit [42]. This result indicates that the pure Hubbard model is not sufficient to describe the superconducting behavior of electrons, and additional terms (like next nearest hoping) is required.

First, we again introduce the Hamiltonian of the $t'$ Hubbard model

$$H = -t \sum_{\langle i,j \rangle;\sigma} \hat{c}^{\dagger}_{i\sigma} \hat{c}_{j\sigma} - t' \sum_{\langle\langle i,j \rangle\rangle;\sigma} \hat{c}^{\dagger}_{i\sigma} \hat{c}_{j\sigma} + U \sum_{i} \hat{n}_{i\uparrow} \hat{n}_{i\downarrow} - \mu \sum_{i} \hat{n}_{i\sigma} \tag{4.1}$$

where the last term of the equation includes the chemical potential.

Also, as before, we again employ two complementary, state-of-the-art methods, density matrix renormalization group (DMRG) method and auxiliary field quantum Monte-Carlo method (AFQMC), to compute the superconducting pairing correlations of the Hubbard model.

To study the superconducting properties of Hubbard model, we use the pairing order parameter. The Hamiltonian for the pairing order parameter is defined as

$$\Delta_{i,j} = \langle (\hat{\Delta}_{ij} + \hat{\Delta}^{\dagger}_{ij})/2 \rangle \tag{4.2}$$

Where the $\langle\rangle$ means the expectation value and $\hat{\Delta}_{ij}$ denotes the pairing order operator on nearest neighbor sites $ij$:

$$\hat{\Delta}_{ij} = \frac{\hat{c}_{i\uparrow}\hat{c}_{j\downarrow} - \hat{c}_{i\downarrow}\hat{c}_{j\uparrow}}{\sqrt{2}} \tag{4.3}$$

To include the pairing order parameter, we need to add a superconducting(SC) field term in Hamiltonian. That is:

$$\hat{H}_p = -\sum_{<i,j>} h_p^{ij} \frac{\hat{\Delta}_{ij} + \hat{\Delta}_{ij}^{\dagger}}{2} \tag{4.4}$$

In this study, the amplitude of the pairing order field $h_p^{ij}$ is constant across all the lattice sites, given by $h_p$, and the sign is positive with the vertical bond (along y direction) and negative with horizonal bond (along x direction). By this way, we can probe the d-wave pairing field $d_{x^2-y^2}$.

In AFQMC study, like double occupancy calculation in Appendix C, the superconducting pairing order is also obtained from the total energy calculation with the Hellmann-Feynman theorem:

$$\Delta(h_p) = \langle \frac{d(H + H_p)}{dh_p} \rangle_{|\psi_0(h_p)>} = \frac{dE(h_p)}{dh_p} \tag{4.5}$$

where $|\psi_0(h_p) >$ represents the ground state of the Hamiltonian $\hat{H} + \hat{H}_p$ with pairing field amplitude $h_p$.

### 4.1.1 Particle hole transformation

Since $c_{i\sigma}^{\dagger}$ and $c_{i\sigma}$ represents the creation and annihilation operators for an electron with spin $\sigma$ at the $i$ th lattice, the particle-hole transformation is the following:

$$\hat{c}_{i\uparrow}^{\dagger} \rightarrow \hat{d}_{i\uparrow}^{\dagger} \tag{4.6}$$

$$\hat{c}_{i\uparrow} \to \hat{d}_{i\uparrow} \tag{4.7}$$

$$\hat{c}^{\dagger}_{i\downarrow} \to \hat{d}_{i\downarrow}(-1)^{i} \tag{4.8}$$

$$\hat{c}_{i\downarrow} \to \hat{d}^{\dagger}_{i\downarrow}(-1)^{i} \tag{4.9}$$

After this transformation, the Hamiltonian term in equation 4.1 will be represented as

$$H = -t\sum_{\langle i,j\rangle}(\hat{d}^{\dagger}_{i\uparrow}\hat{d}_{j\uparrow}+\hat{d}^{\dagger}_{i\downarrow}\hat{d}_{j\downarrow})-t'\sum_{\langle\langle i,j\rangle\rangle}(\hat{d}^{\dagger}_{i\uparrow}\hat{d}_{j\uparrow}-\hat{d}^{\dagger}_{i\downarrow}\hat{d}_{j\downarrow})+U\sum_{i}(\hat{m}_{i\uparrow}-\hat{m}_{i\uparrow}\hat{m}_{i\downarrow})-\mu\sum_{i}(\hat{m}_{i\uparrow}+1-\hat{m}_{i\downarrow}) \tag{4.10}$$

Where $\hat{m}_{i\sigma} = \hat{d}^{\dagger}_{i\sigma}\hat{d}_{i\sigma}$.

Then, the pairing operator $\Delta_{ij}$ ($\Delta^{\dagger}_{ij}$) in equation 4.4 can be expressed as

$$\Delta_{ij} = \frac{(-1)^{j+1}\hat{d}^{\dagger}_{j\downarrow}\hat{d}_{i\uparrow} - (-1)^{i}\hat{d}^{\dagger}_{i\downarrow}\hat{d}_{j\uparrow}}{\sqrt{2}} \tag{4.11}$$

$$\Delta^{\dagger}_{ij} = \frac{(-1)^{j+1}\hat{d}^{\dagger}_{i\uparrow}\hat{d}_{j\downarrow} - (-1)^{i}\hat{d}^{\dagger}_{j\uparrow}\hat{d}_{i\downarrow}}{\sqrt{2}} \tag{4.12}$$

Which keeps the “creation” and “annihilation” operator balanced. In this new Hamiltonian, the sign of the interaction strength is flipped from positive to negative, which describe an ”attractive” interaction. Therefore, we can use a $2N \times\ N_e$ matrix to represent the Slater-determinants in CP-AFQMC calculation, and each orbital is actually a mixture of up and down orbitals in the original form. In the spin balanced model (number of up and down electrons equal, $S_z = 0$), it can be inferred that $N_e = N$.

### 4.1.2 Twist average boundary condition

The twist average boundary condition (TABC) is more complicated to implement. For this boundary condition, when a particle wrap around the periodic boundary, it will also pick up a phase shift $\theta_x$

$$\psi(r_1 + L\hat{x}, r_2, ...r_N) = e^{i\theta_x}\psi(r_1, r_2, ...r_N) \tag{4.13}$$

There are two ways of picking up a phase. One way (type A) is picking up a phase only when a particle crosses the boundary, and the other way (type B) is to split the phase over all the lattices evenly. I will express both ways with a 1-D condition. With L lattices and phase difference $\theta$, we have

$$c^\dagger_{L+x,\sigma} = e^{i\theta}c^\dagger_{x,\sigma}(x = 1, 2......N) \tag{4.14}$$

$$c_{L+x,\sigma} = e^{-i\theta}c_{x,\sigma}(x = 1, 2......N) \tag{4.15}$$

In the first way (type A), we have $c^\dagger_{x+1,\sigma} = c^\dagger_{x,\sigma}$ for x in $1 \leq x \leq N - 1$ and $c^\dagger_{x+1,\sigma} = e^{i\theta}c^\dagger_{x,\sigma}$ for $x = N$, while in the second way, we have $c^\dagger_{x+1,\sigma} = e^{i\frac{\theta}{L}}c^\dagger_{x,\sigma}$ for all $x$s. The annihilation operator is treated in a similar way.

The pairing operator in equation 4.11 can be rewritten as

$$\hat{\Delta}_{x,x+1} = \frac{\hat{c}_{x,\uparrow}\hat{c}_{x+1,\downarrow} - \hat{c}_{x,\downarrow}\hat{c}_{x+1,\uparrow}}{\sqrt{2}}(x \neq L) \tag{4.16}$$

and

$$\hat{\Delta}_{L,1} = \frac{\hat{c}_{L,\uparrow}\hat{c}_{1,\downarrow} - \hat{c}_{L,\downarrow}\hat{c}_{1,\uparrow}}{\sqrt{2}}e^{-i\theta} \tag{4.17}$$

When using the particle hole transformation, we have

$$\hat{d}_{L+1,\uparrow} = \hat{c}_{L+1,\uparrow} = \hat{c}_{1,\uparrow}e^{-i\theta} = \hat{d}_{1,\uparrow}e^{-i\theta} \tag{4.18}$$

$$\hat{d}_{L+1,\downarrow} = (-1)^{L+1}\hat{c}^{\dagger}_{L+1,\downarrow} = (-1)^{L+1}\hat{c}^{\dagger}_{1,\downarrow}e^{i\theta} = \hat{d}_{1,\downarrow}e^{i\theta} \tag{4.19}$$

$$\hat{d}^{\dagger}_{L+1,\uparrow} = \hat{c}^{\dagger}_{L+1,\uparrow} = \hat{c}^{\dagger}_{1,\uparrow}e^{i\theta} = \hat{d}^{\dagger}_{1,\uparrow}e^{i\theta} \tag{4.20}$$

$$\hat{d}^{\dagger}_{L+1,\downarrow} = (-1)^{L+1}\hat{c}_{L+1,\downarrow} = (-1)^{L+1}\hat{c}_{1,\downarrow}e^{-i\theta} = \hat{d}^{\dagger}_{1,\downarrow}e^{-i\theta} \tag{4.21}$$

In the case of the $-U$ Hubbard model, we shall choose $\theta_{\uparrow} = \theta$ and $\theta_{\downarrow} = -\theta$

Now, we can see how the pairing order parameter transforms in the $-U$ Hubbard model. Consider the equation 4.11 again, we have

$$\Delta_{L,1} = \frac{(-1)^{L+1+1}\hat{d}^{\dagger}_{L+1,\downarrow}\hat{d}_{L,\uparrow} - (-1)^{L}\hat{d}^{\dagger}_{L\downarrow}\hat{d}_{L+1,\uparrow}}{\sqrt{2}} = \frac{(-1)^{L}\hat{d}^{\dagger}_{1,\downarrow}\hat{d}_{L,\uparrow} - (-1)^{L}\hat{d}^{\dagger}_{L\downarrow}\hat{d}_{1,\uparrow}}{\sqrt{2}}e^{-i\theta} \tag{4.22}$$

and

$$\Delta^{\dagger}_{L,1} = \frac{(-1)^{L}\hat{d}^{\dagger}_{L,\uparrow}\hat{d}_{1,\downarrow} - (-1)^{L}\hat{d}^{\dagger}_{1,\uparrow}\hat{d}_{L,\downarrow}}{\sqrt{2}}e^{i\theta} \tag{4.23}$$

Thus, we can use these formula above to conduct the pairing order computation.

In the second way (type B), we use $\bar{\hat{c}}^{\dagger}$ $(\bar{\hat{c}})$ rather than $\hat{c}^{\dagger}$ $(\hat{c})$ to represent the creation (annihilation) operator. We have

$$\bar{\hat{c}}_{x\sigma} = \hat{c}_{x\sigma}e^{i(x-1)\frac{\theta}{L}}(2 \leq x \leq L+1) \tag{4.24}$$

$$\bar{\hat{c}}^{\dagger}_{x\sigma} = \hat{c}^{\dagger}_{x\sigma}e^{-i(x-1)\frac{\theta}{L}}(2 \leq x \leq L+1) \tag{4.25}$$

And at the boundary we require $\bar{\hat{c}}_{L+1,\sigma} = \bar{\hat{c}}_{1,\sigma}$ and $\bar{\hat{c}}^{\dagger}_{L+1,\sigma} = \bar{\hat{c}}^{\dagger}_{1,\sigma}$

| TBC | energy per site | pairing order per site | density |
|---|---|---|---|
| Type A | -1.15861112 | 0.01108939 | 0.82422077 |
| Type B | -1.15861112 | 0.01108939 | 0.82422077 |

TABLE 4.1: benchmark comparison of a non-interacting system using two types of twist boundary conditions, type A (picking up a phase only when particles cross the boundary) and type B (splitting the phase over all the lattice cites evenly). The system is $20 \times 4$, $t' = -0.2t$, with chemical potential $\mu = 0.8$ and twist angle $k_x = 1.2994\pi, k_y = 0.6026\pi$. These results shows two type of boundary conditions are equivalent.

Then the pairing operator equation 4.11 can be written as

$$\hat{\Delta}_{x,x+1} = \frac{\bar{\hat{c}}_{x,\uparrow} e^{-i(x-1)\frac{\theta}{L}} \bar{\hat{c}}_{x+1,\downarrow} e^{-ix\frac{\theta}{L}} - \bar{\hat{c}}_{x,\downarrow} e^{-i(x-1)\frac{\theta}{L}} \bar{\hat{c}}_{x+1,\uparrow} e^{-ix\frac{\theta}{L}}}{\sqrt{2}} = \frac{\bar{\hat{c}}_{x,\uparrow}\bar{\hat{c}}_{x+1,\downarrow} - \bar{\hat{c}}_{x,\downarrow}\bar{\hat{c}}_{x+1,\uparrow}}{\sqrt{2}} e^{-i(2x-1)\frac{\theta}{L}} \tag{4.26}$$

Next, we go back to the $-U$ model, and we plug in

$$\bar{\hat{c}}^{\dagger}_{x\uparrow} \to \bar{\hat{d}}^{\dagger}_{x\uparrow} \qquad \bar{\hat{c}}_{x\uparrow} \to \bar{\hat{d}}_{x\uparrow} \qquad \bar{\hat{c}}^{\dagger}_{x\downarrow} \to \bar{\hat{d}}_{x\downarrow}(-1)^x \qquad \bar{\hat{c}}_{x\downarrow} \to \bar{\hat{d}}^{\dagger}_{x\downarrow}(-1)^x \tag{4.27}$$

to obtain

$$\Delta_{x,x+1} = \frac{(-1)^{x+1}\bar{\hat{d}}^{\dagger}_{x+1,\downarrow}\bar{\hat{d}}_{x,\uparrow} - (-1)^{x}\bar{\hat{d}}^{\dagger}_{x,\downarrow}\bar{\hat{d}}_{x+1,\uparrow}}{\sqrt{2}} e^{i(2x-1)\frac{\theta}{L}} \tag{4.28}$$

$$\Delta^{\dagger}_{x,x+1} = \frac{(-1)^{x+1}\bar{\hat{d}}^{\dagger}_{x,\uparrow}\bar{\hat{d}}_{x+1,\downarrow} - (-1)^{x}\bar{\hat{d}}^{\dagger}_{x+1,\uparrow}\bar{\hat{d}}_{x,\downarrow}}{\sqrt{2}} e^{-i(2x-1)\frac{\theta}{L}} \tag{4.29}$$

Above is the twisted version of the one-dimension Hamiltonian with pairing field after the particle-hole transformation. We can obtain higher dimension Hamiltonian similarly.

In fact, the two ways of distributing the phase are equivalent, which means in exactly the same model, changing the way of distributing the phase from type A (picking up a phase only when particle cross the boundary) to type B (splitting the phase over all the lattices evenly) or from type B to type A will not change any of the observables in the system. One model example is shown in Table 4.1.

### 4.1.3 AFQMC approach with self-consistent constraint

After introducing the particle hole transformation, the AFQMC method can implement the pairing order with Hamiltonian 4.1 and 4.4. Instead of using back-propagation to obtain the pairing order parameter directly, we use the Hellman-Feynman theorem, as discussed in equation 4.5, which leads to much more accurate results.

The traditional way of computing the derivative in equation 4.5 is using finite difference $\Delta(h_p) = (E(h_p - \delta) - E(h_p + \delta))/(2\delta) + O(\delta^2)$, as done in article [33]. However, this way requires much more accurate AFQMC calculation, since a very small $\delta$ leads to a diverging uncertainty, and a large $\delta$ leads to a finite difference error. To obtain smoother results, we compute the pairing order using the derivative of the fitted energy curve. For each $h_p$, we fit the energy curve with quadratic function using four nearby points, $E(h_p - (2i-3)\delta)(i = 0, 1, 2, 3)$, or five nearby points, $E(h_p - (2i-4)\delta)(i = 0, 1, 2, 3, 4)$. The total uncertainty is obtained from the combination of fitting error and QMC errors.

Similar to the independent-particle self-consistent constraint used to obtain spin and hole density in Chapter 3, we also develop a similar self-consistent procedure for the paring order parameter calculation.

The trial wave function used in obtaining the ground state of $H + H_p(h_p)$ is the ground state of the non-interacting Hamiltonian with pairing field $\alpha h_p$.

$$H_{non}(\alpha h_p) = -t \sum_{\langle i,j \rangle} (d^\dagger_{i\uparrow} d_{j\uparrow} + d^\dagger_{i\downarrow} d_{j\downarrow}) - t' \sum_{\langle\langle i,j \rangle\rangle} (d^\dagger_{i\uparrow} d_{j\uparrow} - d^\dagger_{i\downarrow} d_{j\downarrow}) - \mu \sum_i (m_{i\uparrow} + 1 - m_{i\downarrow}) + H_p(\alpha h_p) \tag{4.30}$$

where $H_p$ is given by equation 4.4.

In each iteration, $\mu$ is constant during all iterations. $\alpha$ is a an extra parameter determined by the self-consistent procedure and is determined by minimizing

$$\Delta' = \sum_{h_p} |\Delta_H(h_p) - \Delta_{H_{non}}(\alpha h_p)| \tag{4.31}$$

Thus, the whole self-consistent procedure is the following: First, we set up $H$ and corresponding non-interacting Hamiltonian $H_{non}$ using different $\mu$ that target the same density, and an arbitrary $\alpha_{init}$ value for $H_{non}$. We obtain the ground state of $H_{non}(h_p, \alpha)$ for the trial wave function of each $h_p$ energy calculation. Then, we obtain the QMC energy results, calculating the pairing order using equation 4.5 and find a new $\alpha$ value to minimize the difference (as equation 4.31 states). We repeat step one using $\alpha_{new}$ value, until it converges. Finally, we output the last step for the energy and pairing order result. The detailed procedure is visualized in Fig. 4.1.

In fact, it turns out that the converged $\alpha$ value is independent of the initial $\alpha_{init}$ value chosen. We take an example of a $16 \times 4$ cylinder with $U = 8$, $t' = -0.2t$ and $\delta = 1/4$ to illustrate our procedure and accuracy with DMRG. In order to target the 1/4 doping, a fixed value of chemical potential $\mu = 0.8$ is used in both the DMRG and AFQMC calculations. The results for the pairing order parameter $\Delta$ are shown in Fig. 4.2.

Besides, we can see the perfect agreement of pairing order with DMRG in Fig. 4.2. The energy per site obtained by QMC with $h_p = 0.156$ is $-1.5071(1)$ in both cases, while the corresponding DMRG result is $-1.5017$. With only 0.36% of discrepancy, we can see that AFQMC has good agreement with DMRG.

With a robust procedure and good agreement with DMRG in the example case, we can move on to investigate systems with both $t' = 0.2$ and $t' = -0.2$ with various dopings.

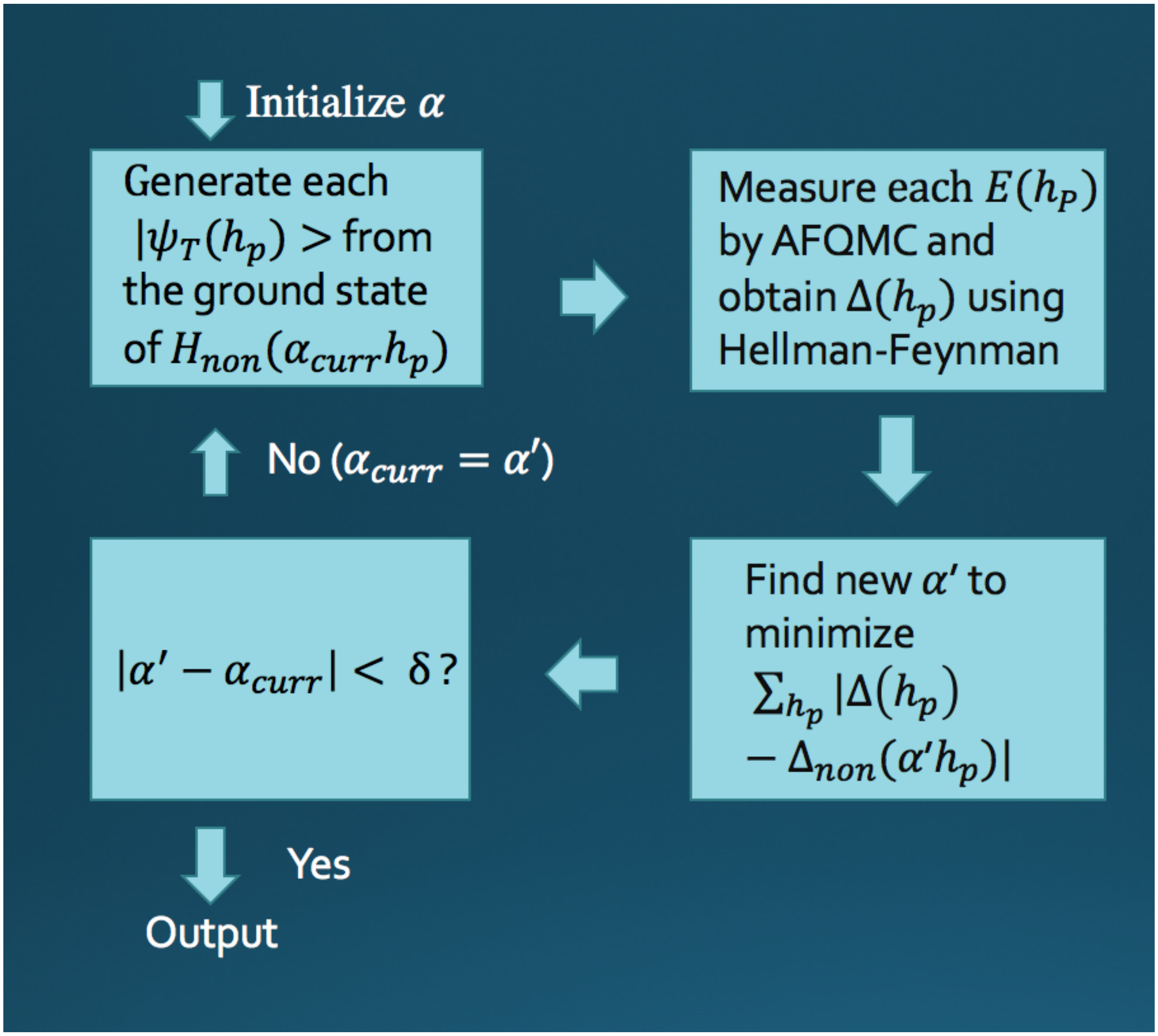

FIG. 4.1: The detailed self-consistent iteration procedure for calculating pairing order for each $h_p$.

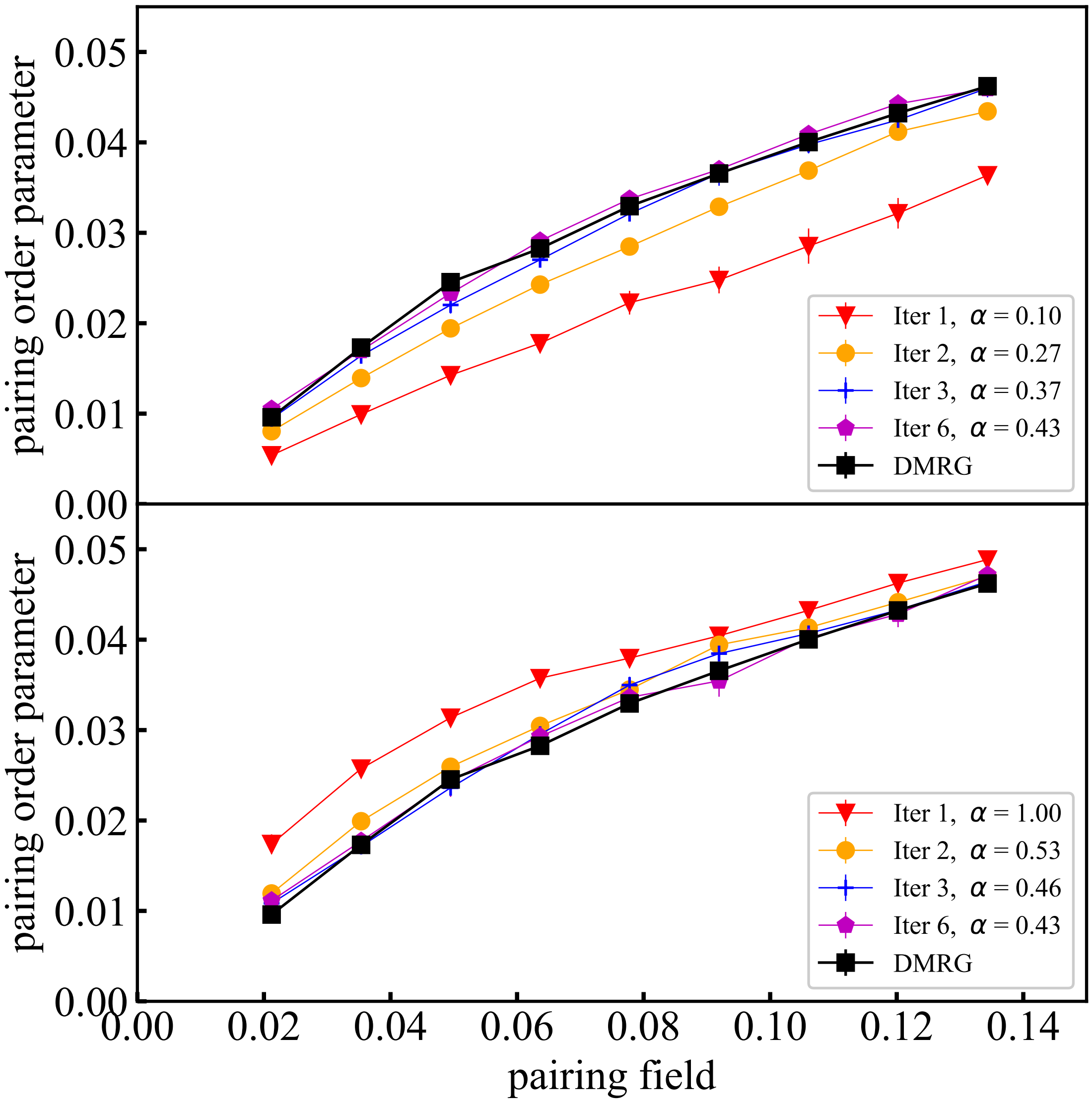

FIG. 4.2: The example of $16 \times 4$ cylinder with $U = 8$, $t' = -0.2t$ and $\delta = 1/4$ to illustrate our procedure and accuracy with DMRG. Top: the iteration procedure using initial $\alpha = 0.1$. Bottom: iteration procedure using initial $\alpha = 1.0$. It turns out that final pairing order and $\alpha$ value is independent of the initial value chosen, and have excellent agreement with DMRG calculation.

## 4.2 Benchmark study with AFQMC and DMRG

Previously we introduce a background description of the pairing order parameter calculation and our most advanced self-consistent iteration procedure. In this section, we will use our procedure to investigate the superconducting pairing correlation for various dopings with both $t' = 0.2t$ and $t' = -0.2t$. As we discussed in the previous chapter, systematic error is introduced in the AFQMC calculation due to treating the Fermi sign problem approximately. Therefore, comparisons with DMRG method on width-4 system is essential. In the previous section, we obtained an excellent agreement with DMRG for $t' = -0.2t$ with 1/4 doping system, but more benchmark comparisons are needed. All results, from now on, are with interaction strength $U = 8t$.

The overall comparison is promising, though there are some disagreement between the two methods in a few cases. However these discrepancies can all be explained by competition between the ground state and the nearest excited states, and these have little effect on the finite size scaling extrapolation.

### 4.2.1 t'=-0.2t

In Fig. 4.2, we see the excellent agreement for 1/4 doping, but a discrepancy appear with DMRG increases at 1/5 doping, $20 \times 4$ lattice. The results are shown in Fig.4.3

This discrepancy can be explained by the intertwined states near the ground state. In the DMRG calculation, there is a small kink between the pairing field $h_p = 0.12$ and $h_p = 0.13$. This kink can be explained by the competition between two different states. They have different pairing order parameter but very close energies, since in the lower panel of Fig. 4.3 , no energy kink is observed anywhere including the ”kinked” pairing order parameter area, and the excited state energy is at most 0.05% higher than the ground state (at $h_p = 0$). In the AFQMC calculation, we find no order parameter kink, and the paring

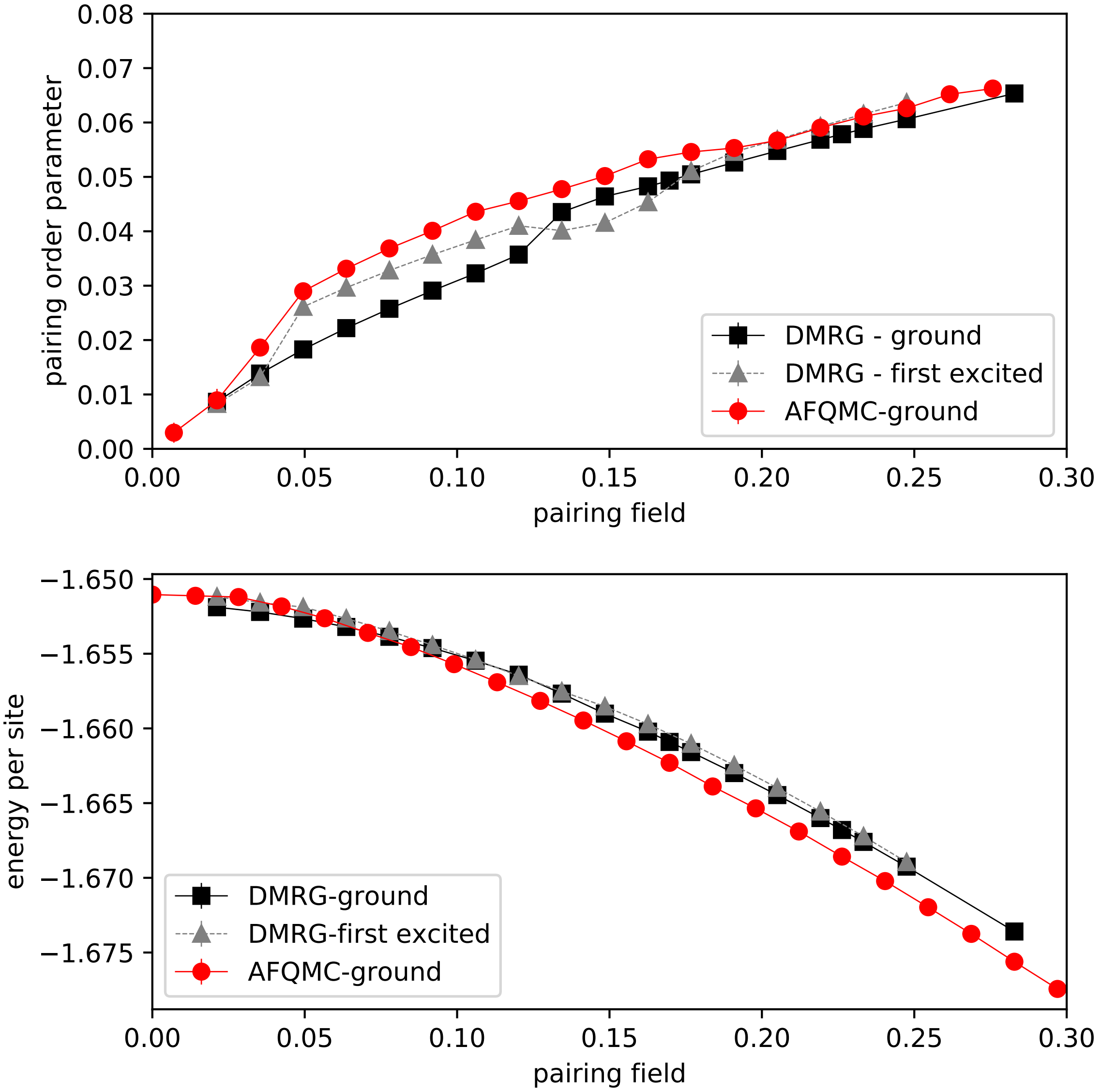

FIG. 4.3: The AFQMC and DMRG energy and pairing order result for $1/5$ doping and $t' = -0.2$ with PBC. Although the discrepancy between DMRG and QMC is greater than that for $1/4$ doping, we find that two states are competing in DMRG, with very close energy (only 0.2% relative error). In fact, AFQMC is more consistent with the first excited state of DMRG with $h_p < 0.12$, while AFQMC agrees better with DMRG ground state with $h_p > 0.13$

order parameter is more consistent with the first excited state of DMRG with pairing field $h_p < 0.12$ while agrees better with DMRG ground state with pairing field $h_p > 0.13$.

This behavior also happens in 4-width systems with different twist boundary condition. Fig. 4.4 shows the pairing order parameter with pairing field $h_p = 0.205$ with different twists. Left is the PBC result, and right is anti-PBC result. The figure shows that the QMC and DMRG ground and first few excited states ranges overlap, or at least are very close to each other. The twist average order parameter value for this pairing field is 0.054(3) for DMRG and 0.052(3) for QMC, which means the discrepancies between DMRG and QMC on each twist bond cancel each other out when using a twist average value for this system.

Next, we compare the twist average order parameter results for other $h_p$ results, and thus eventually we have twist boundary conditions along both the $x$ and $y$ direction instead of only $y$, to further reduce finite size effects. We then do calculations on wider systems, from 4 legs to 6,8..... up to 16 legs. These results are shown in Fig. 4.5. It turns out that twist average DMRG on cylindrical $20 \times 4$ systems have excellent overall agreement with AFQMC, and the twist average value $20 \times 4$ cylinder system is nearly the same as systems with both sides periodic, which means a length of 20 is long enough for finite size scaling. However, the finite size effect on the width of system is crucial, since there is huge difference between $20 \times 4$ and $20 \times 16$ twist average results.

The stripe order of the ground state for the same doping and the same $t' = -0.2$ but without superconducting pairing field is also studied. As with the previous spin density wave study, the magnetic pinning fields $v_p = 0.25$ are also added on the shorter side of the cylinder to break the symmetry. Figure 4.6 shows the comparison. As a result, all figures with both methods show a stripe pattern, but the wavelength of DMRG and QMC with PBC is different. It turns out that in QMC, the energy of the stripe state, which is same as DMRG, is only 0.001 above the energy of the ground state, which thus indicate the the

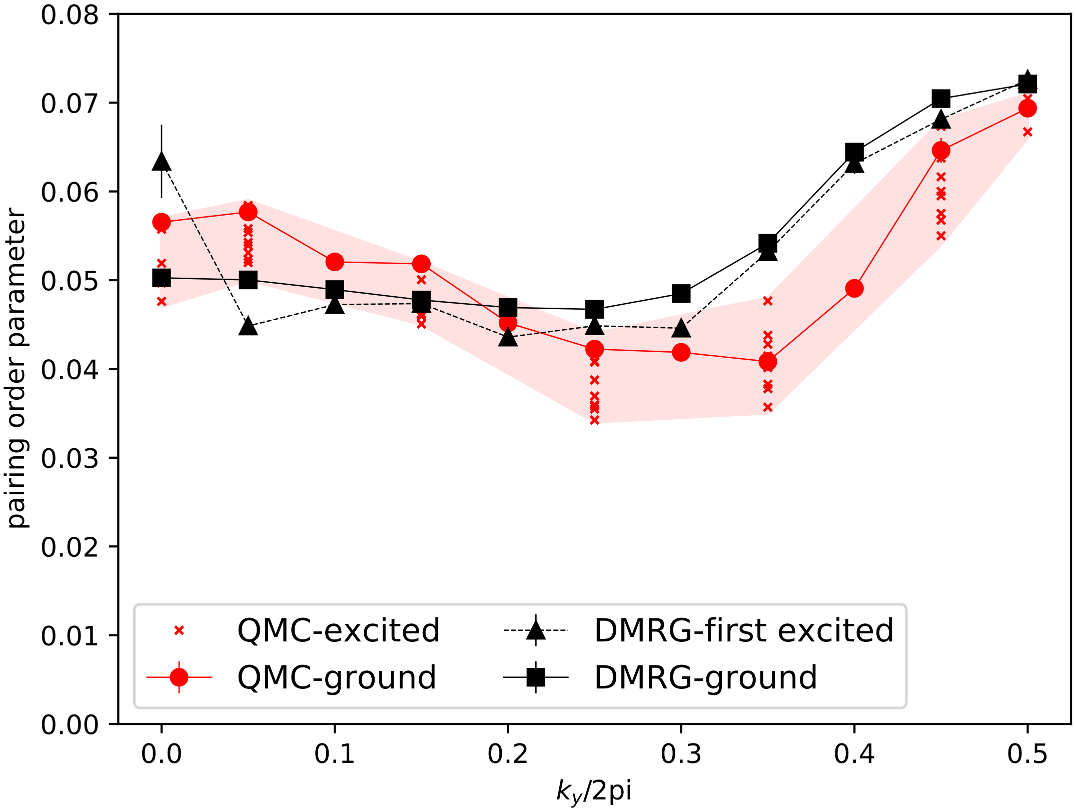

FIG. 4.4: The pairing order parameter for each twist value in the $y$ direction with pairing field $h_p = 0.205$. The twists in the $y$ direction ranges for 0(PBC) to $\pi$(Anti-PBC). The red shaded area is where the first few QMC excited states falls, while black dashed line is the DMRG first excited state. The figure shows that the QMC and DMRG ground and first few excited states range overlaps, or at least they are very close to each other. The twist average order parameter value for this pairing field is 0.054(3) for DMRG and 0.052(3) for QMC, which means the discrepancies between DMRG and QMC on each twist bond cancel each other out when using twist average value for this system.

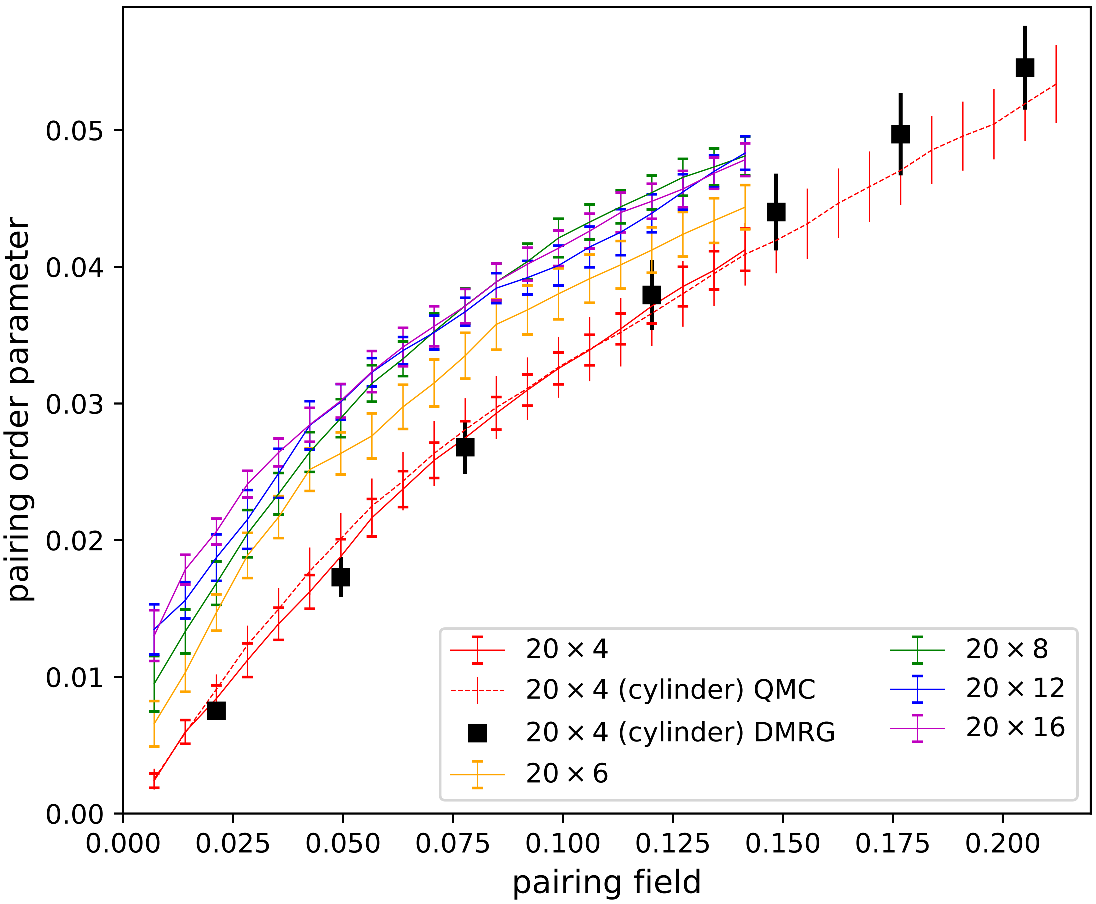

FIG. 4.5: The twist average order parameter results on different lattice sizes and different boundary condition, with $t' = -0.2t$ and 1/5 doping. The twist average DMRG on a cylinder $20 \times 4$ system have excellent overall agreement with AFQMC, and the twist average value $20 \times 4$ cylinder system is nearly the same as systems with both sides periodic, which means 20 is long enough for finite size scaling. However, the finite size effect from the width of system is crucial, since there is huge difference between $20 \times 4$ and $20 \times 16$ twist average results.

competition between ground state and excited state in the PBC lattice. In the anti-PBC lattice calculation, the DMRG and QMC results have excellent agreement.

Overall, we have excellent agreement on the pairing order for QMC and DMRG for 1/4 doping. Although we have a noticeable discrepancy between DMRG and QMC in the PBC lattice with 1/5 doping, for both the spin and superconducting patterns, there is good evidence that it is a matter of competition between the ground and excited states. Next we show that this discrepancy has little impact when using finite size scaling with twist averaged boundary conditions.

### 4.2.2 t'=0.2t

Past research using DMRG in the t-J model, one of the Hubbard descendants model, shows that superconductivity may exists with next nearest hoping $t' = 0.2t$ [53], which makes further investigation on this $t'$ important.

The benchmark comparison of this $t'$ is excellent on the PBC lattice with both 1/5 doping and 1/8 doping, which is shown in Fig. 4.7. However, the finite size effect is significant in $16 \times 4$ and $16 \times 6$ cylinder. With 1/8 doping, it turns out that PBC and anti-PBC give absolutely different responses with the same pairing field. Both QMC and DMRG state on the $16 \times 4$ cylinder, system with anti-PBC have much stronger superconducting properties than system with PBC. While, in $16 \times 6$, system with PBC have stronger superconducting properties than that with APBC. These results are included in Fig.4.8

We investigate the fluctuation of the pairing order parameter for different twist angles, due to the same pairing field, the results will be shown in Fig.4.9. We can see things become reversal in width 4 and width 6 systems. In width 4 systems, PBC system have stronger superconducting properties and it goes down quickly as twist angle $k_y$ increase, while in 6

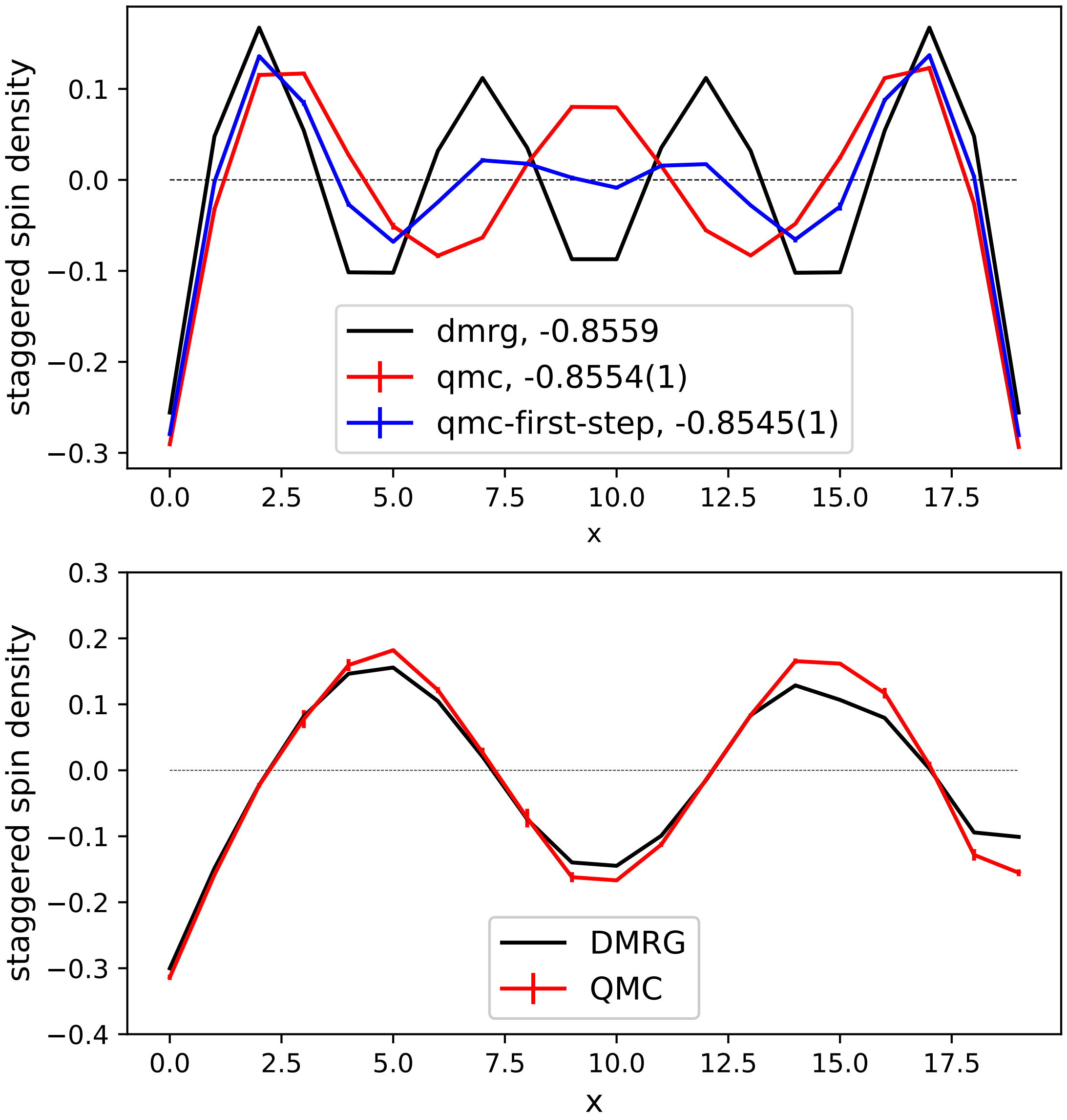

FIG. 4.6: The staggered spin density benchmark comparison of DMRG and QMC results for 1/5 doping with $t' = -0.2t$, with PBC(above) and Anti-PBC(below). The magnetic pinning fields $v_p = 0.25$ are added on both periodic sides of the PBC lattice, and only one side in Anti-PBC lattice. As a result, all figures with both methods shows stripe pattern, but the wavelength for DMRG and QMC with PBC are different. It turns out that in QMC, the energy of the stripe state, which is same as DMRG, is only 0.001 above the energy of the ground state. In APBC calculation, the DMRG and QMC have excellent agreement.

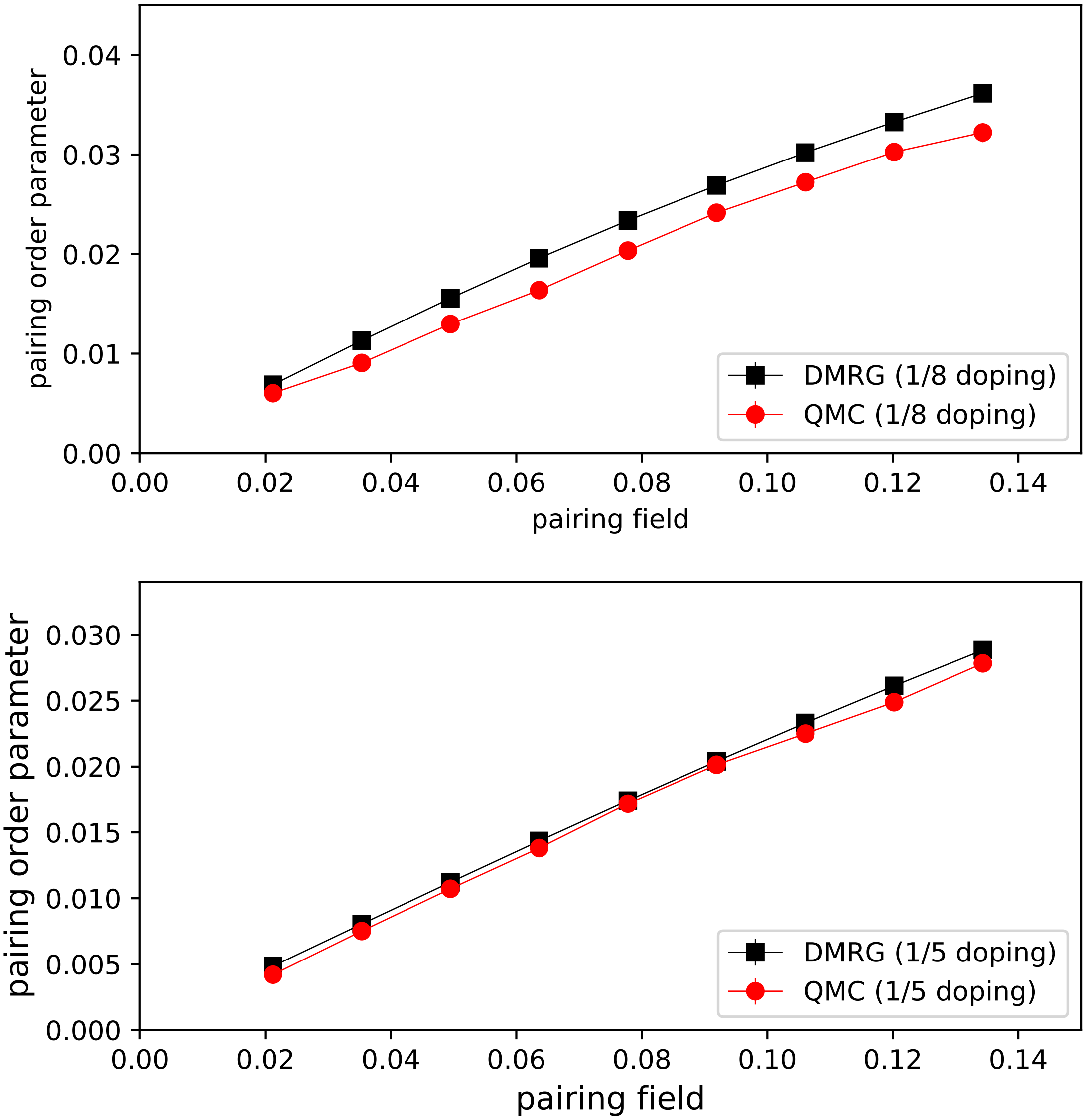

FIG. 4.7: The bencmark comparison of DMRG and QMC result for 1/8 doping (upper panel) and 1/5 doping (lower panel) with $t' = 0.2t$, with lattice sizes $16 \times 4$ and $20 \times 4$ and both PBC. Both methods have good agreement at both doping.

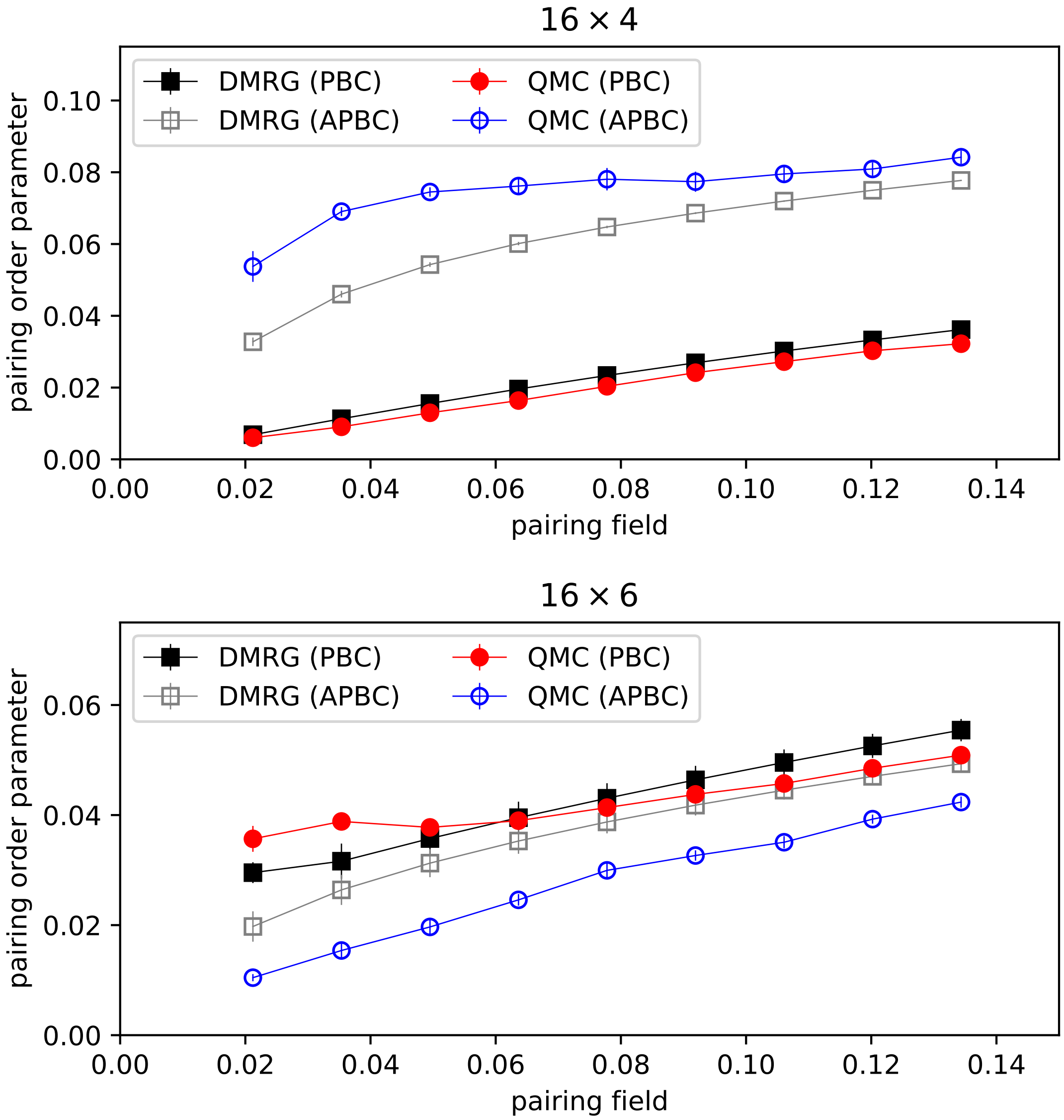

$16 \times 4$

$16 \times 6$

FIG. 4.8: The benchmark comparison of DMRG and QMC result for 1/8 doping with $t' = 0.2t$, with PBC and Anti-PBC. The upper panel shows the $16 \times 4$ result and the lower panel shows the $16 \times 6$ results. In this figure, both DMRG and AFQMC shows stronger superconducting properties in PBC lattice of 4 legs cylinder, and Anti-PBC lattice in 6 legs cylinder.

systems, there is a sharp peak at $k_y = \pi$, which corresponds to anti-PBC system.

On the other hand, the pairing order fluctuation is smaller in 6 legs system, because the wider system have smaller size effect. This is shown in both figure 4.9 and 4.8, with both AFQMC and DMRG methods. However, the discrepancy become larger in Anti-PBC in both 4 and 6 legs system, which means more efforts are needed to further this.

For the stripe study, like $t' = -0.2$ study, we also plot the staggered spin density result of DMRG and QMC, details are shown in Fig.4.10. Both figure shows the excellent agreement, and the different spin pattern (AFM from PBC and filled stripe from Anti-PBC) indicates the large finite size effects on the $16 \times 4$ cylinder. All these results show the importance and necessity of finite size scaling in our study.

## 4.3 Finite size scaling of pairing order parameter

After benchmark comparison with DMRG, we now move on to finite size scaling with AFQMC. Figure 4.5 has already shown that finite size scaling is critical in obtaining the thermaldynamic limit for the pairing order parameter in response of pairing field, especially in the shorter $y$ direction. We would continue take this as an example to show our detailed steps.

In Fig.4.11, we use a system with $U = 8$, $t' = -0.2t$ and $1/5$ doping as an example to show the extrapolation result to thermaldynamic limit. First, we calculate twist average results for the pairing order parameter with respect to the pairing field, with various lattice sizes from $16 \times 4$ to $16 \times 20$. Then, the extrapolation with respect to the inverse of the system width $1/L_y$ is performed with same $h_p$, and the resulting pairing order parameter $\Delta_\infty(h_p)$ is shown on the left. Then, in third figure, both linear and quadratic extrapolation of $h_p$ are performed to obtain $\Delta_\infty(0)$, with results 0.016(2) (linear) and 0.015(3) (quadratic). Thanks to our latest advanced algorithm, we have much better

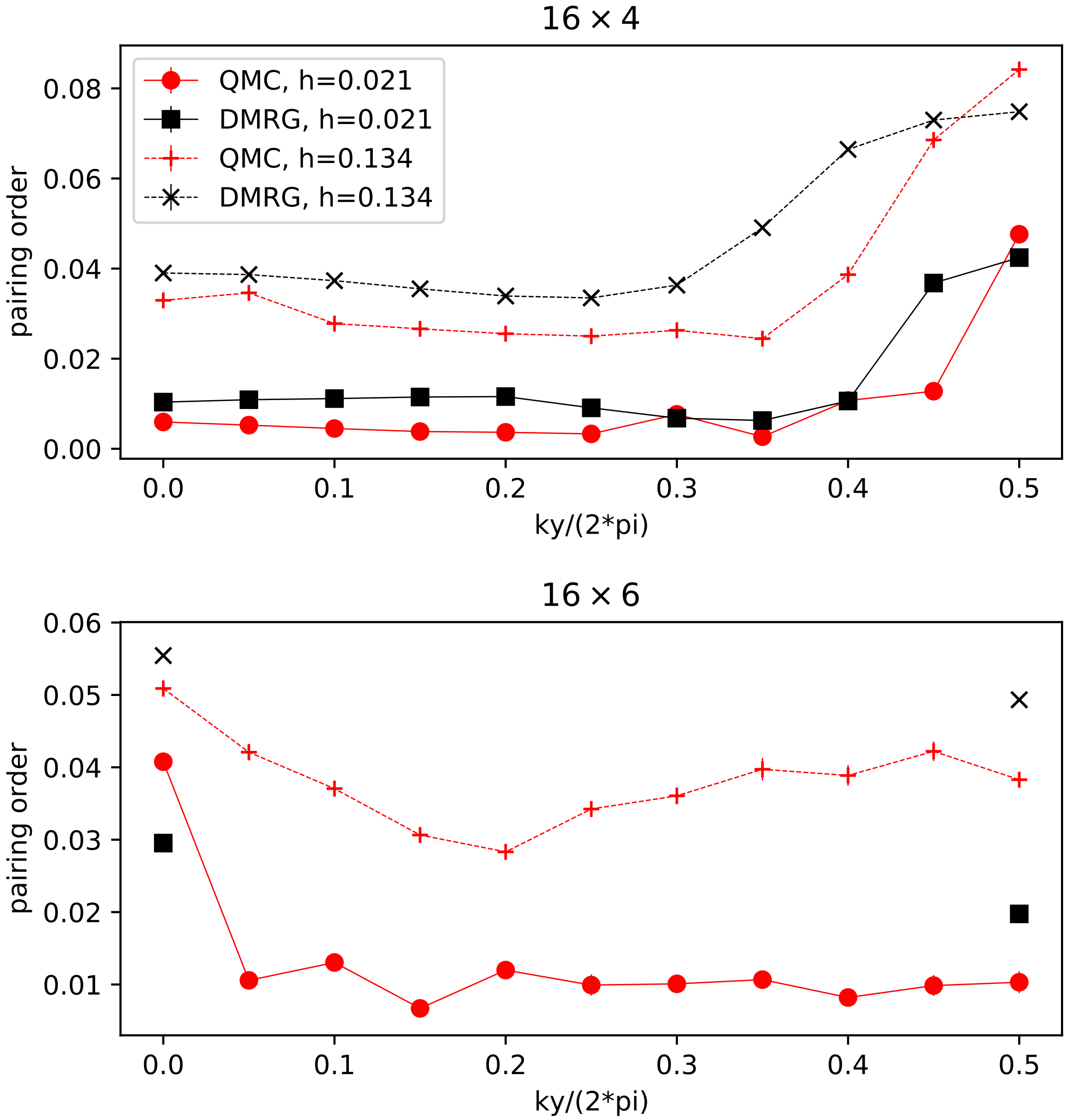

FIG. 4.9: The benchmark comparison of DMRG and QMC result for 1/8 doping with $t' = 0.2t$, with pairing field strengths $h_p = 0.021$ and $h_p = 0.134$ at each twist value. The upper panel shows 16 × 4 result and the lower panel shows 16 × 6 results. In this figure, both QMC and DMRG shows a sharp peak at $k_y = 0$ in the 4 legs cylinder, and $k_y = \pi$ in the 6 legs cylinder.

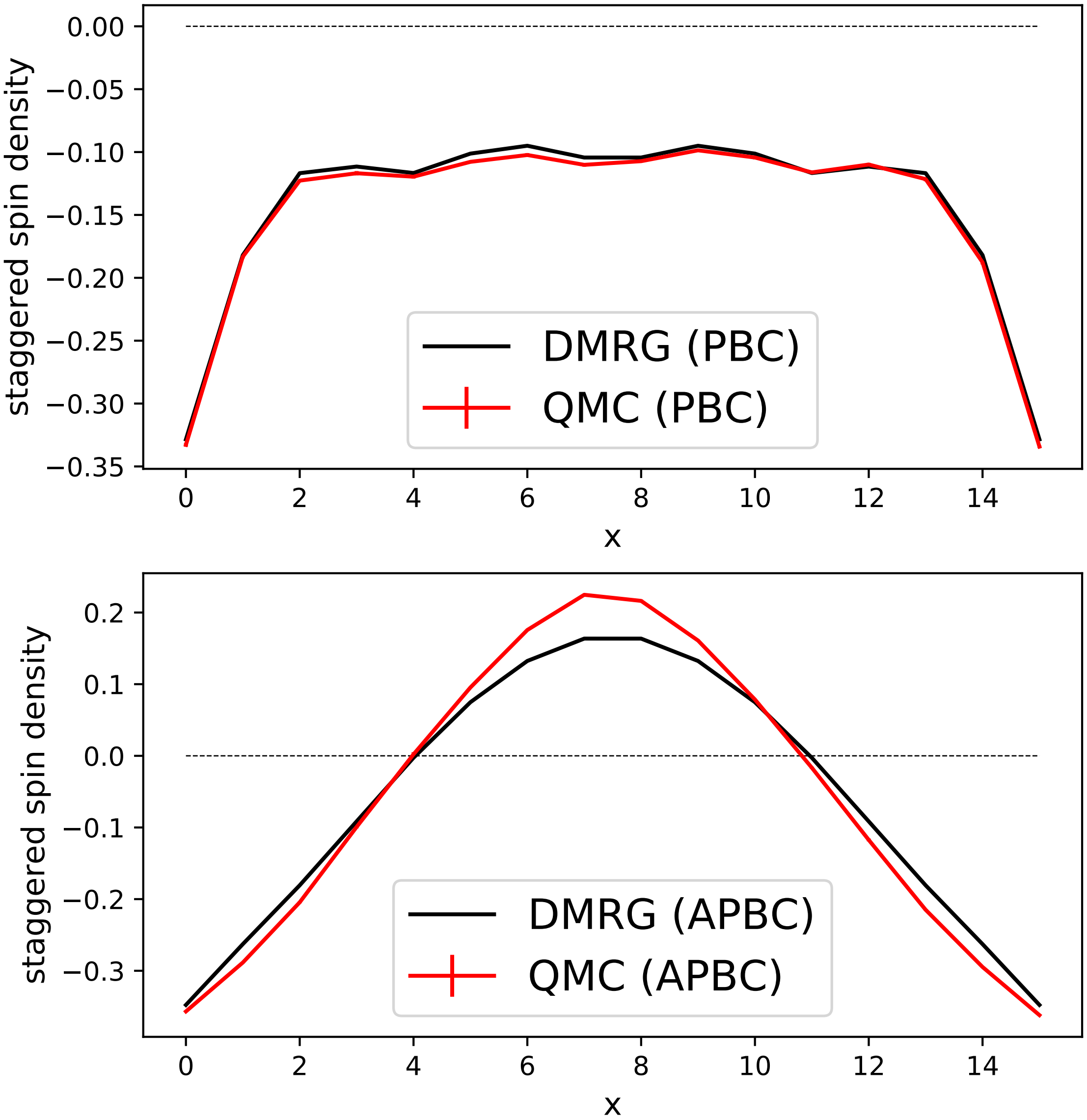

FIG. 4.10: The staggered spin density benchmark comparison of DMRG and QMC results for 1/8 doping with $t' = 0.2t$, with PBC(above) and Anti-PBC(below). Magnetic pinning fields $v_p = 0.25$ are added on both periodic sides in both figures. Both figure shows the excellent agreement between DMRG and AFQMC.

data quality than previous $t' = 0$ calculation. [33]. Most data points are within one error bar away from the extrapolation in the second and third figures, which both show the robustness of our extrapolation. These results shows there are good prospects for superconductivity exists in the Hubbard model with $U = 8$, $t' = -0.2t$ and 1/5 doping.

Another example, with positive $t' = 0.2t$ and 1/8 doping, is shown in Fig .4.12. It follows the same procedure as above, but gives a different result. The superconducting pairing order at infinite lattice without pairing field $\Delta_\infty(0)$ is 0.006(3) with linear extrapolation and 0.006(4) with quadratic extrapolation, which is much weaker than the $t' = -0.2t$ and 1/5 doping system.

We also conduct simulations with different dopings for both $t' = 0.2t$ and $t' = -0.2t$, with all the results included in the Fig. 4.13. Overall, the superconductivity pairing order at $t' = -0.2t$ is stronger than that at $t' = 0.2t$, which seems in contradiction with the previous DMRG investigation with t-J model [53]. This research, however, has not concluded, and more efforts is needed to further understand these systems.

## 4.4 Stripe order and its relationship with superconductivity in t' model

In previous studies, superconductivity seems to have a subtle competition and/or coexistence with stripe order [30, 31, 32, 33]. In the previous chapter, we already showed that with the sufficient interaction $U$, stripe order would exists as the form of filled stripes in the ground state of pure Hubbard model. However, with next nearest hopping, the stripe pattern may change, and phase separation could occur. Thus, it is necessary to study the stripe order of both $t' = 0.2t$ and $t' = -0.2t$ model.

First, we compute the spin density pattern for $t' = -0.2t$ and $t' = 0.2$ lattice. The

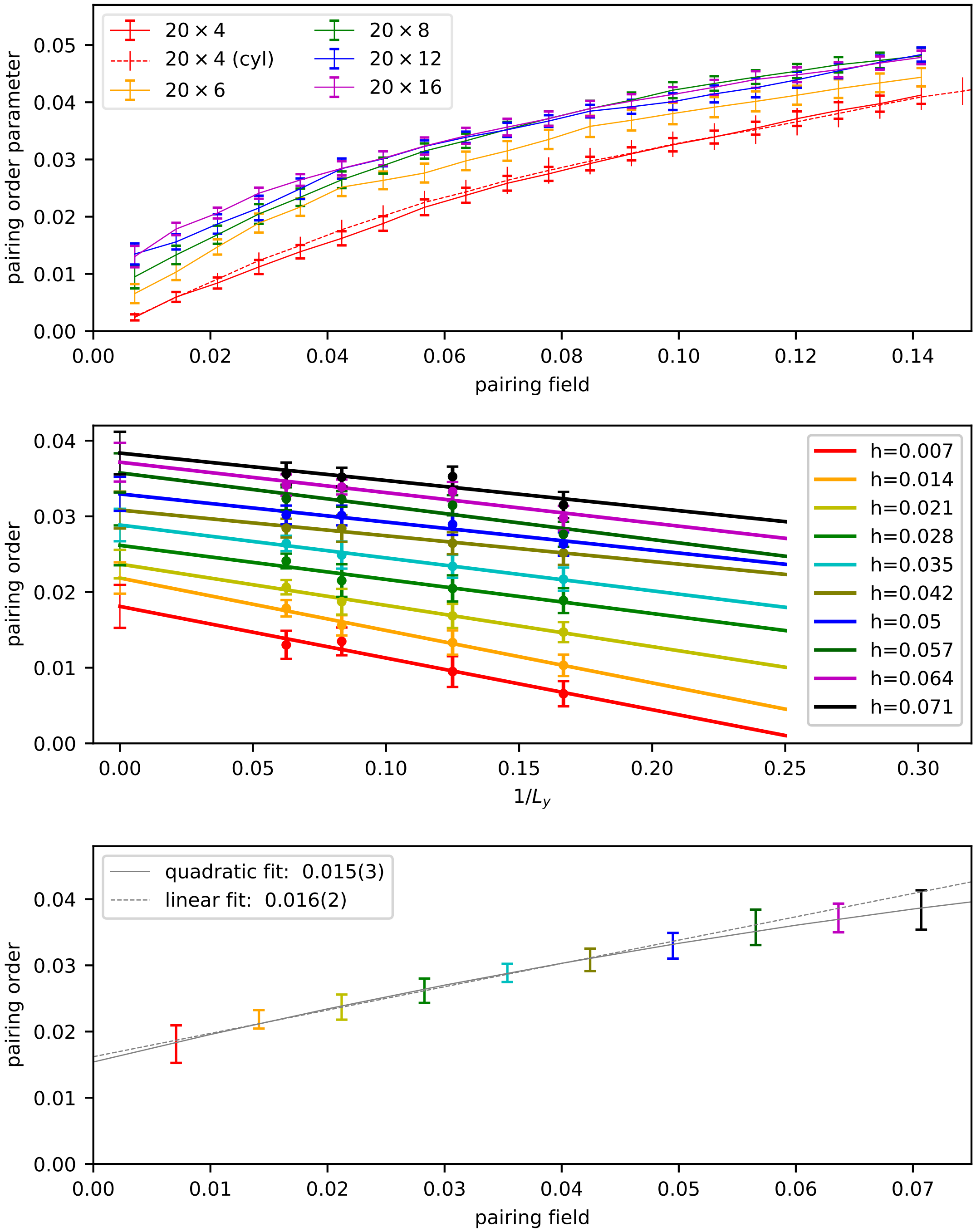

FIG. 4.11: Finite size scaling of the pairing order parameter with $t' = -0.2t$ and $1/5$ doping. The top plot shows the twist average results for the pairing order parameter due to the pairing field in various lattice sizes(cyl represents cylinder boundary condition), and the middle plot is the linear extrapolation results from the top plot, which is performed with respect to the inverse of system width $1/L_y$. The resulting pairing order parameter $\Delta_\infty(h_p)$ is shown on the left. Then, in the bottom plot, for each $h_p$, both linear and quadratic extrapolation are performed to obtain $\Delta_\infty(0)$, with results 0.016(2) and 0.015(3). These results shows significant evidence for superconductivity exists in the Hubbard $U = 8$, $t' = -0.2t$ and $1/5$ doping system.

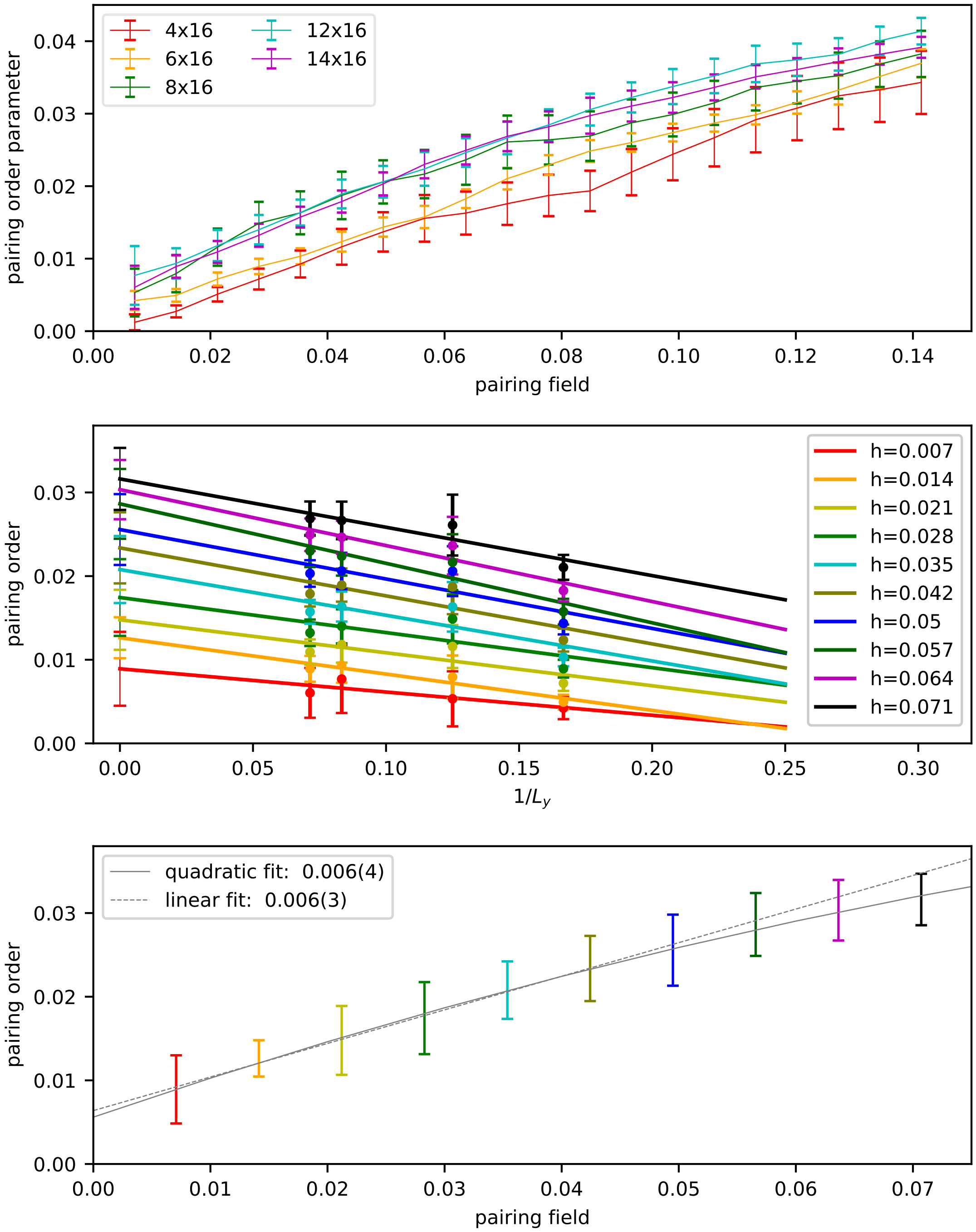

FIG. 4.12: Finite size scaling of the pairing order parameter with $t' = -0.2t$ and $1/5$ doping. The top plot shows the twist average results for the pairing order parameter due to the pairing field in various lattice sizes(cyl represents cylinder boundary condition), and the middle plot is the linear extrapolation results from the top plot, which is performed with respect to the inverse of system width $1/L_y$. The resulting pairing order parameter $\Delta_\infty(h_p)$ is shown on the left. Then, in the bottom plot, for each $h_p$, both linear and quadratic extrapolation are performed to obtain $\Delta_\infty(0)$, with results 0.006(4) and 0.006(3). These results shows little superconducting pairing order in Hubbard $U = 8$, $t' = 0.2t$ and $1/8$ doping system.

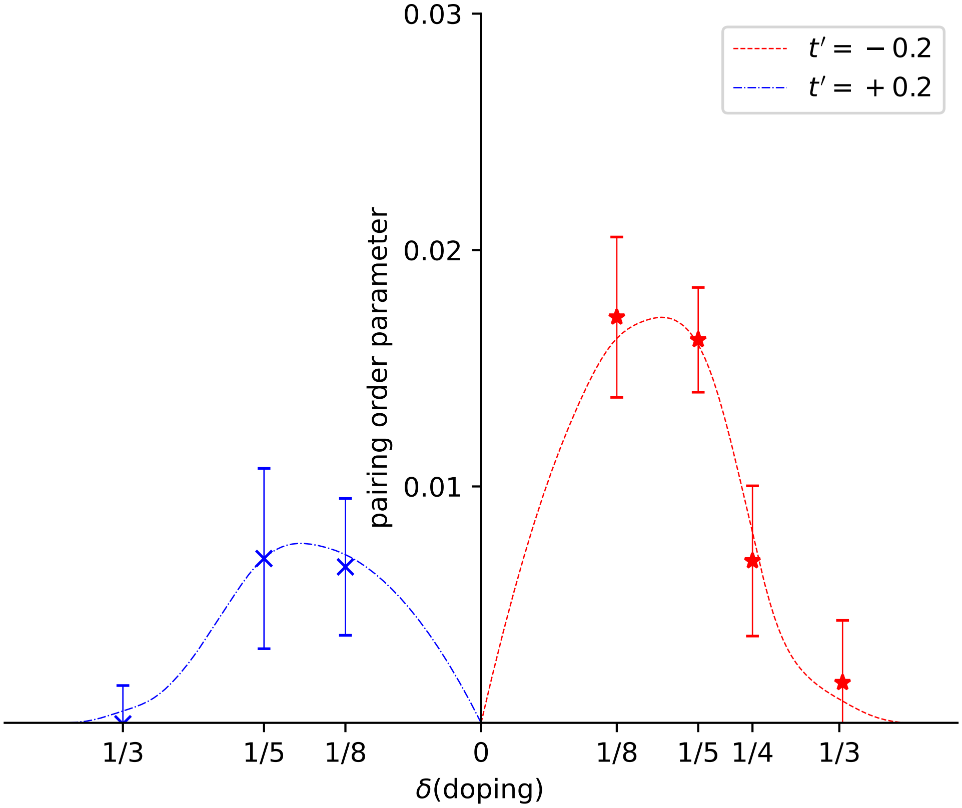

FIG. 4.13: The pairing order parameter $\Delta_\infty(0)$ for each doping with $t' = 0.2t$ and $t' - 0.2t$. The plot indicates that at $t' = -0.2t$, superconductivity pairing is stronger than that of $t' = 0.2t$. Besides, both $t' = 0.2t$ and $t' - 0.2t$ see vanishing superconducting order with the doping increases above $1/4$ doping.

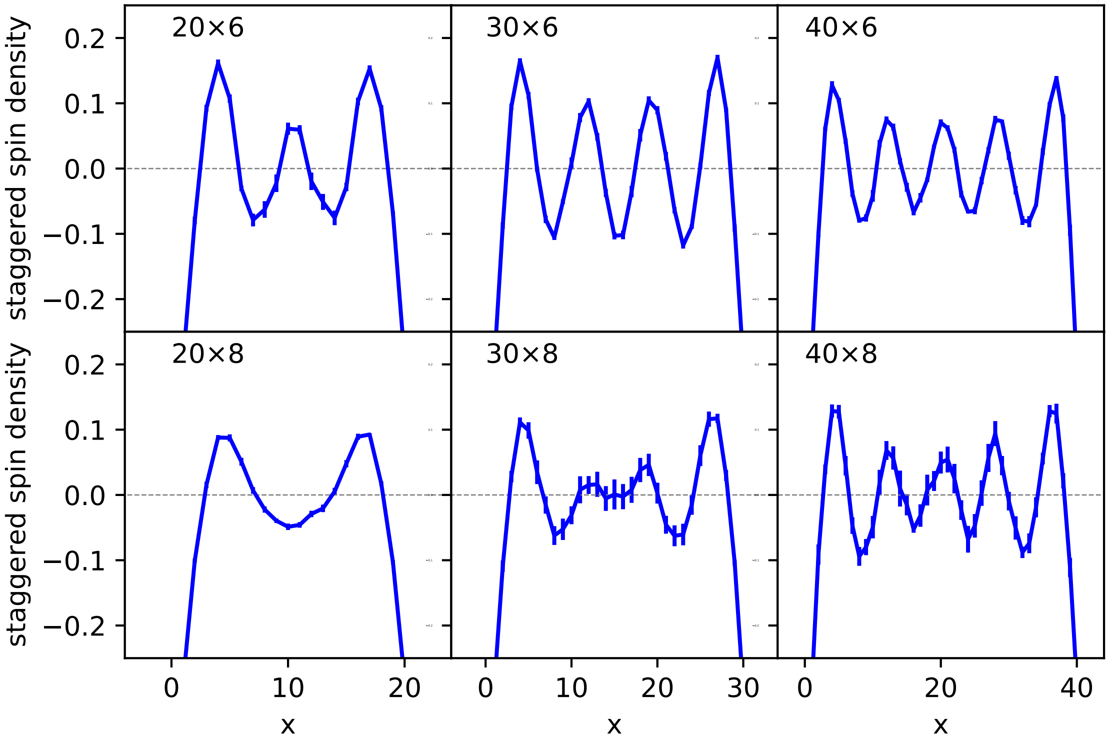

FIG. 4.14: Staggered spin density of 1/5 doping and $t' = -0.2t$ with various lattice sizes, from $20 \times 6$ to $40 \times 8$. We can see spin density wave exists, which the wavelength $1.5/h$ is different from pure Hubbard model with $2/h$

Fig.4.14 shows the staggered spin density of 1/5 doping and $t' = -0.2t$ with various lattice sizes, from $20 \times 6$ to $40 \times 8$. In these figures, we can see that the modulated antiferromagnetic(AFM) order persists with $t' = -0.2t$ and $U = 8$, from $16 \times 6$ to $32 \times 8$, similar to our previous investigation at pure Hubbard model. However, the wavelength of the spin density wave is about $1.5/h$, which is different from that of pure Hubbard model. Similar spin density wave with wavelength about $1.5/h$ can be also observed for a lattice with $t' = -0.2t$ with 1/8 doping.

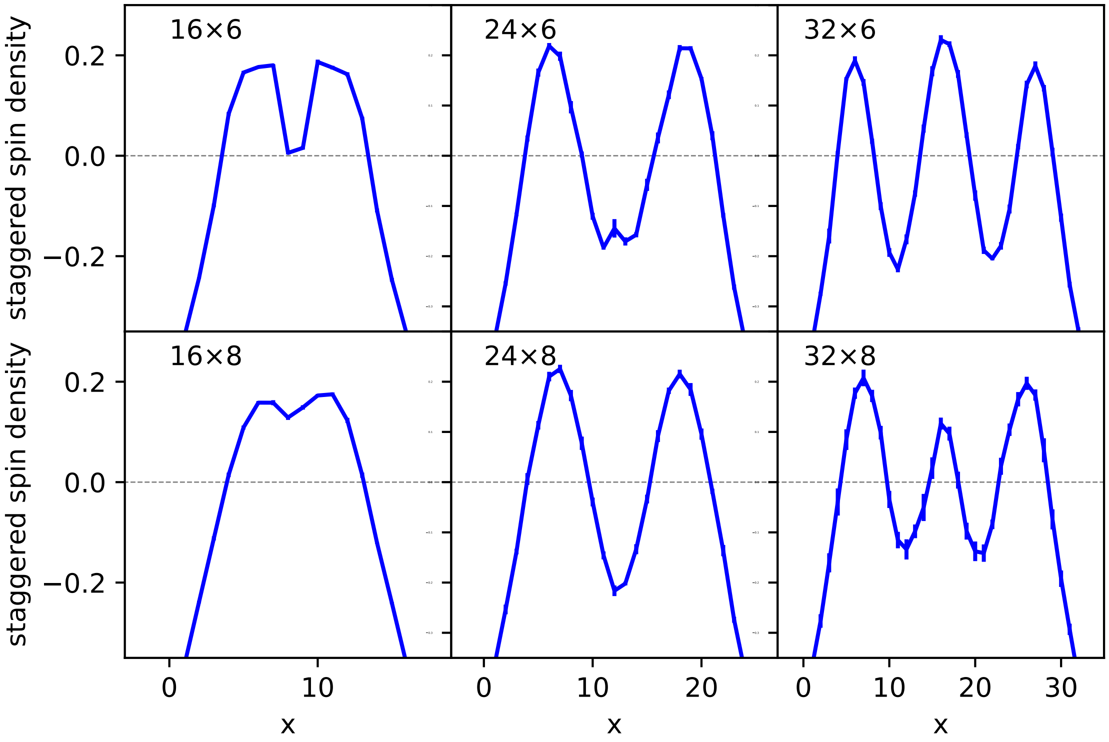

FIG. 4.15: Staggered spin density for 1/8 doping and $t' = -0.2t$ with various lattice sizes, from $16 \times 6$ to $32 \times 8$. We can see spin density wave exists, but the wavelength is $1.5/h$, which is different from pure Hubbard model with $2/h$

Notably, for $t' = 0.2t$, we cannot see the stable stripe pattern. The $16 \times 4$ lattice shows AFM order with PBC, but with anti-PBC, the ground state sees clearly filled stripes. With wider systems, from $16 \times 6$ to $32 \times 8$, we also observe different ground state spin patterns. These results are shown in Fig. 4.16.

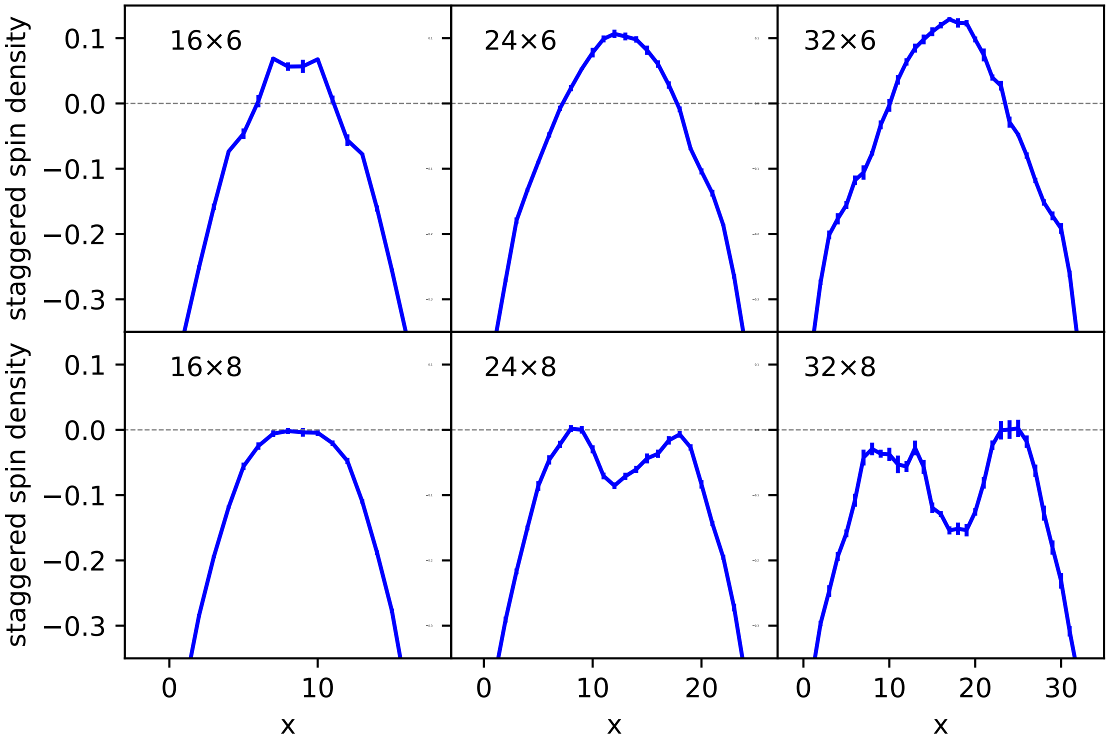

FIG. 4.16: Staggered spin density for 1/8 doping and $t' = 0.2$ with various lattice sizes, from $16 \times 6$ to $32 \times 8$. No clear common spin pattern is observed in these lattice sizes

In order to observe the behavior of the stripe/SDW order with the superconductivity pairing order, we add magnetic pinning fields on all lattices to further strengthen the amplitude of the spin density to see the variation of pairing order. We take $16 \times 4$ cylinder with 1/8 doping and $t' = 0.2t$ as an example, since Fig. 4.10 QMC results shows excellent agreement with DMRG. We add a AFM type spin pinning field in lattice with PBC, and filled stripe type pinning to a lattice with anti-PBC (consistent with their ground state spin type). The results are shown in Fig. 4.17. After the pinning fields added, the QMC agreement with DMRG becomes better, but the relationship of the stripe order with superconducting pairing order is unclear, since in the PBC lattice, the growth of the spin density pattern contributes to the growth of the pairing order. On the contrary, in Anti-PBC lattice, the growth of the spin density results in the pairing order to decrease.

In all, we can see that the existence of next nearest hopping changes the ground state spin and stripe pattern of Hubbard model. The ground state is no longer a $2/h$ spin density wave or filled stripes. For $t' = -0.2t$ the wavelength of the stripe pattern changes, and for $t' = 0.2t$ the stripe pattern vanishes. The relationship of the stripe order with the superconducting pairing order is intriguing and requiring further study to understand how they relate to each other.

The computing is mostly carried out at the Flatiron Institute, with message passing interface (MPI). The estimated computational time various by several factors, the number of walkers, the system size, etc... The largest system we have conducted in the superconducting study is $20 \times 16$, with 1/5 doping and $U = 8t$. The running time for each k-point is 16 hours, with 40 walkers distributed on each core and 256 cores for each k-point, and 10 k-points for each system. Usually, given the computational resources we have, it usually takes less than 12 hours to fully conduct a small system (like $16 \times 4$) run, and about one or two weeks to fully run a large system like $20 \times 16$.

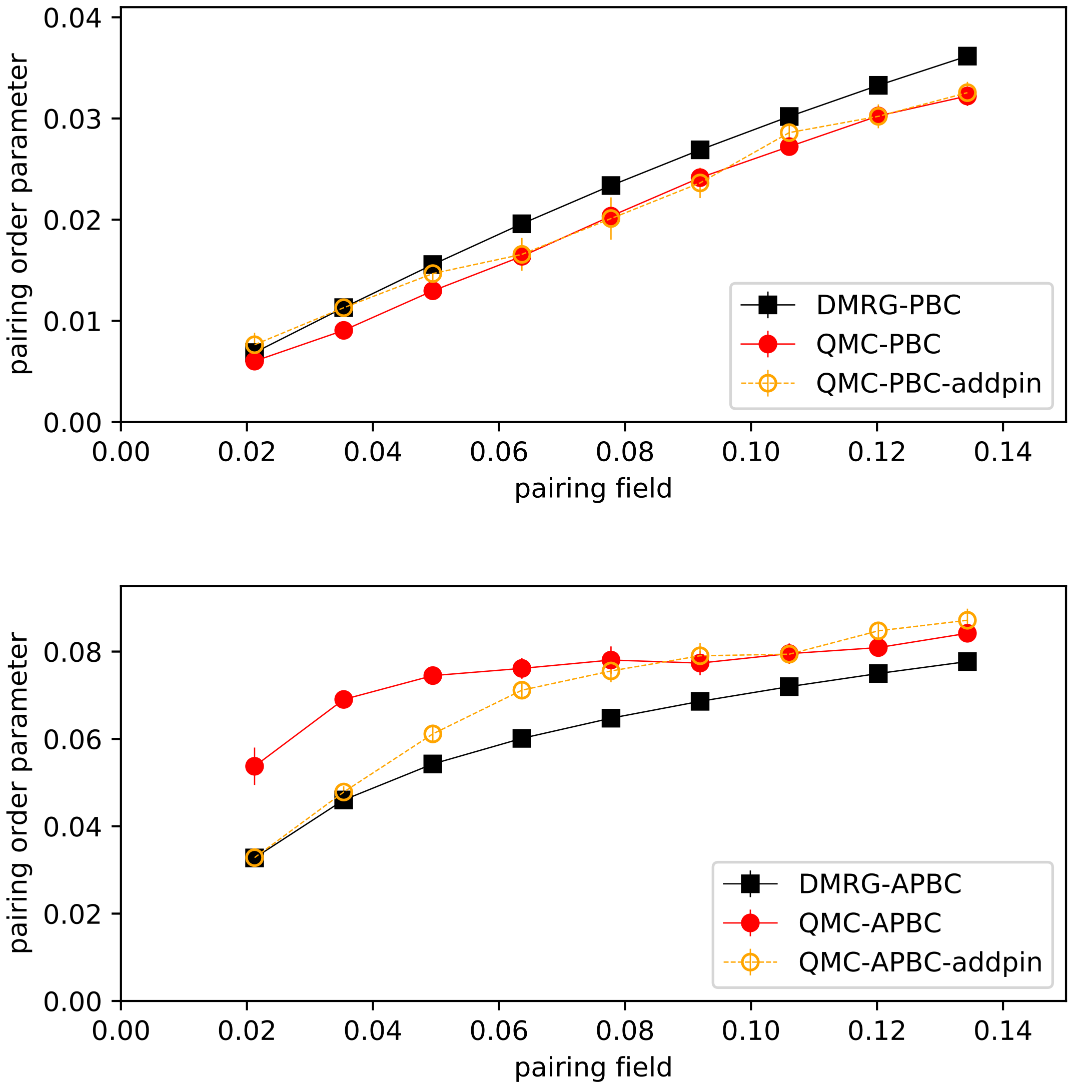

FIG. 4.17: The superconducting pairing order for PBC (upper) and APBC (lower) in $16 \times 4$ cylinder with 1/8 doping and $t' = 0.2$. The red solid curve is the original QMC result while orange dashed lines represents the results with spin-like pinning fields similar with the ground state spin pattern added on all of the lattices. The results shows better agreement with DMRG after the spin-like pinning fields added, but the relationship of the stripe order with the superconducting pairing order is unclear, since in the PBC lattice, the growth of spin density pattern contributes to the growth of pairing order, while in the Anti-PBC lattice, the growth of spin density waves occurs as the pairing order decreasing.

# CHAPTER 5

# Summary and perspective

In this thesis, our main focus is on the stripes, spin/charge density waves and superconducting pairing order in the 2D doped repulsive Hubbard model, which have already drawn great interests in the realm of condensed matter physics. We use one of the most accurate methods - auxiliary field quantum monte-carlo (AFQMC) method, with our most recent advanced algorithm. Excellent benchmark comparison with density matrix renormalization group (DMRG) makes our results convincing.

We systemically study the stripes and spin density waves in the doped 2D Hubbard model with only nearest hoping. Modulated SDW or stripe orders are found to exists for sufficient large interaction $U$ with doping $\delta$ up to 1/5. The period of the SDW(CDW) is found to be $2/\delta$ ($1/\delta$ ). After carefully performing finite size scaling to large simulation cells sizes, we mapped out the ground state phase diagram as a function of $U$ and $\delta$.

Apart from the stripe order, we also investigate double occupancy and effective hoping of the Hubbard model. We measure the conductivity of the Hubbard model by calculating the charge gap and quantum metric tensor. Both the charge gap and quantum metric tensor results indicate that the Hubbard model is conducting in the paramagnetic state (without stripe order). However, the quantum metric tensor calculation cannot determine whether this model is conductive or not.

Following the precedent study of “pure” Hubbard model [33], we further investigate the superconducting pairing correlation of the Hubbard model with next nearest hoping, as well as the stripe order. Our algorithmic advances include a more robust procedure for self-consistent constraints in AFQMC and twist average boundary conditions which can handle finite size effects more effectively. As a result, we see much stronger superconducting pairing order in $t' = -0.2t$ than that of $t' = 0.2t$, though more study is still needed to consolidate this result. We compute the superconducting order parameter in the ground state for a number of parameter sets ($t'$, $\delta$) and discuss its interplay with magnetic and charge orders.

In the future, we will further study the Hubbard model with next nearest hoping. And, hopefully, obtain the stripe ground state phase diagram as a function of $U$, $\delta$ and $t'$. For investigating superconducting, we will also study models with $t'$ other than -0.2 and 0.2. More advanced techniques will also be developed for calculating properties more precisely.

# APPENDIX A

# Additional filling of stripes

In the Fig. 3.9, we vary the length of the cylinder (hence also Ne, in order to maintain the same $\delta$) while keeping the width fixed at 6 and see the staggered spin density became strongest and fluctuation is minimized at length 24, The corresponding charge order also forms a regular wave with hole density peaks at the nodal position of the spin order. This is consistent with the conclusion that SDW wavelength 2 $\delta$ and CDW wavelength 1 $\delta$.

Below are the Additional results shown in Fig.A.1, Fig.A.2 and Fig.A.3. These results correspond to $h = 1/10$ doping and $U = 5$, $h = 1/8$ doping and $U = 6$, and $h = 1/6$ doping and $U = 8$.

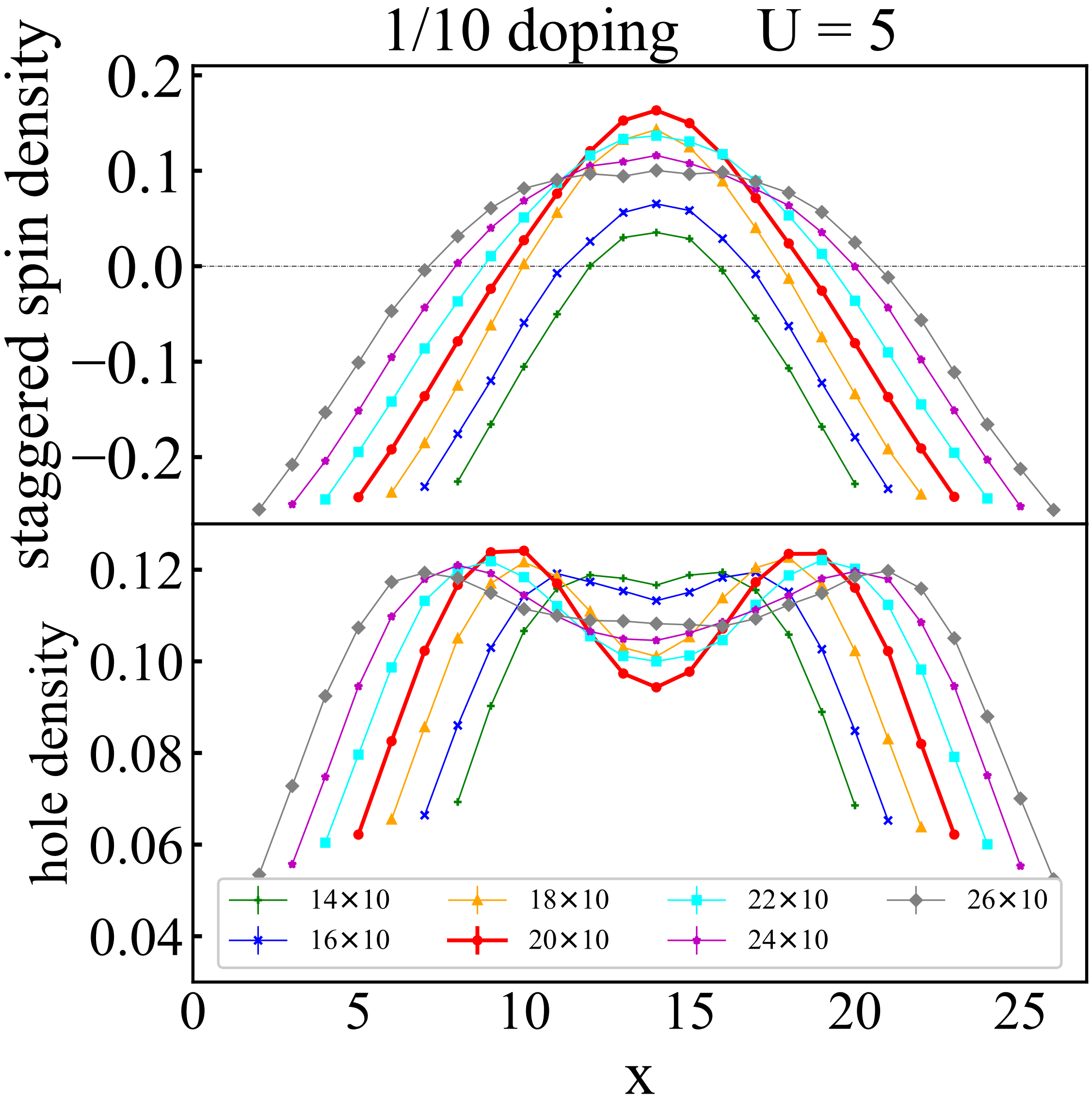

FIG. A.1: Staggered spin (top panel) and hole (bottom) densities at $\delta = 1/10$ doping and $U = 5$, in width-6 cylinders as the length $L_x$ is varied. Results are omitted at the left edge ($i_x = 1$), where the pinning field is applied. When $L_x$ is commensurate with the expected wavelengths for spin and charge orders ($1/\delta$ and $2/\delta$), the spin and charge density waves are least frustrated and have the largest amplitude.

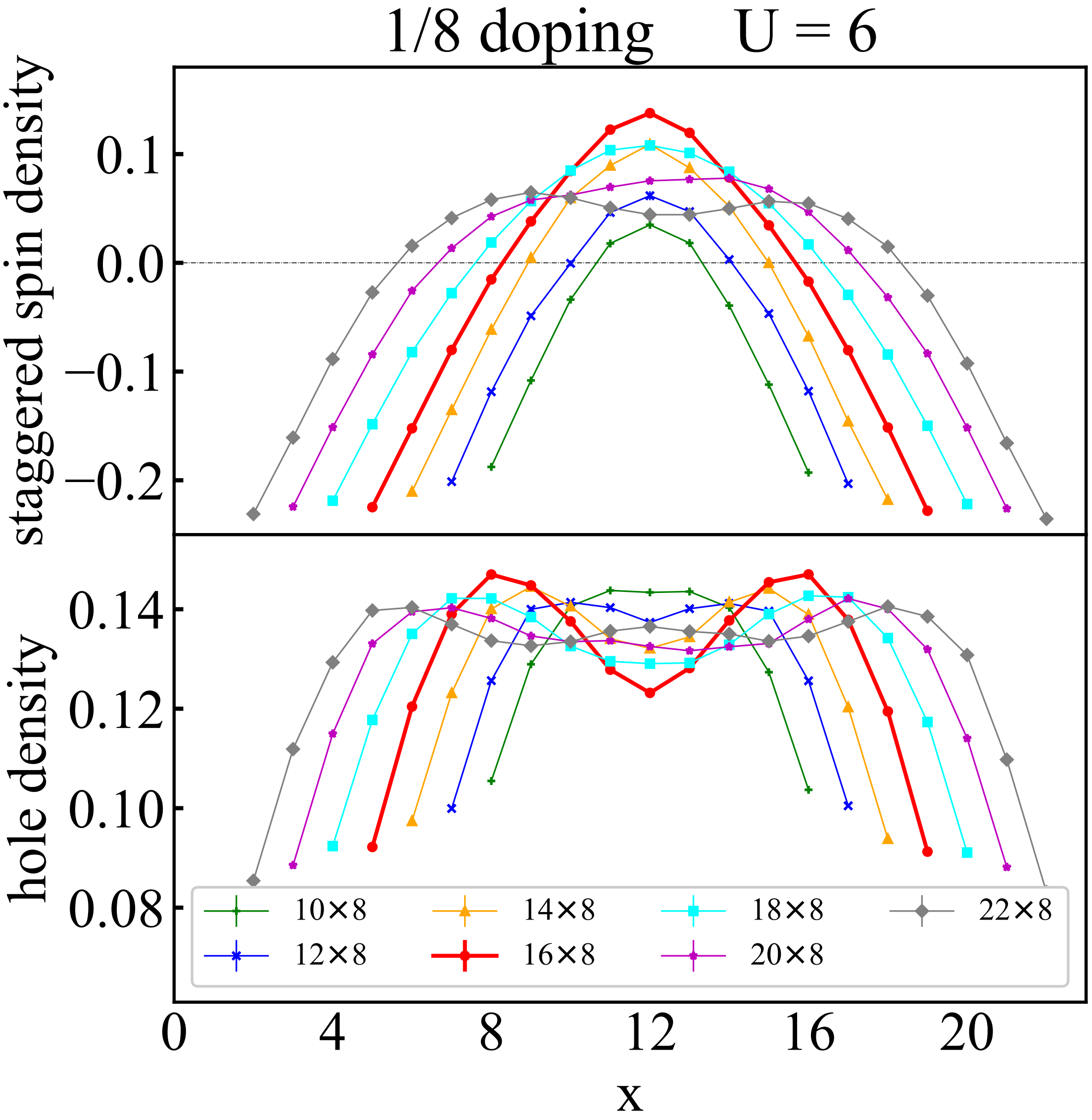

FIG. A.2: Staggered spin (top panel) and hole (bottom) densities at $\delta = 1/8$ doping and $U = 6$, in width-6 cylinders as the length $L_x$ is varied. Results are omitted at the left edge ($i_x = 1$), where the pinning field is applied. When $L_x$ is commensurate with the expected wavelengths for spin and charge orders ($1/\delta$ and $2/\delta$), the spin and charge density waves are least frustrated and have the largest amplitude.

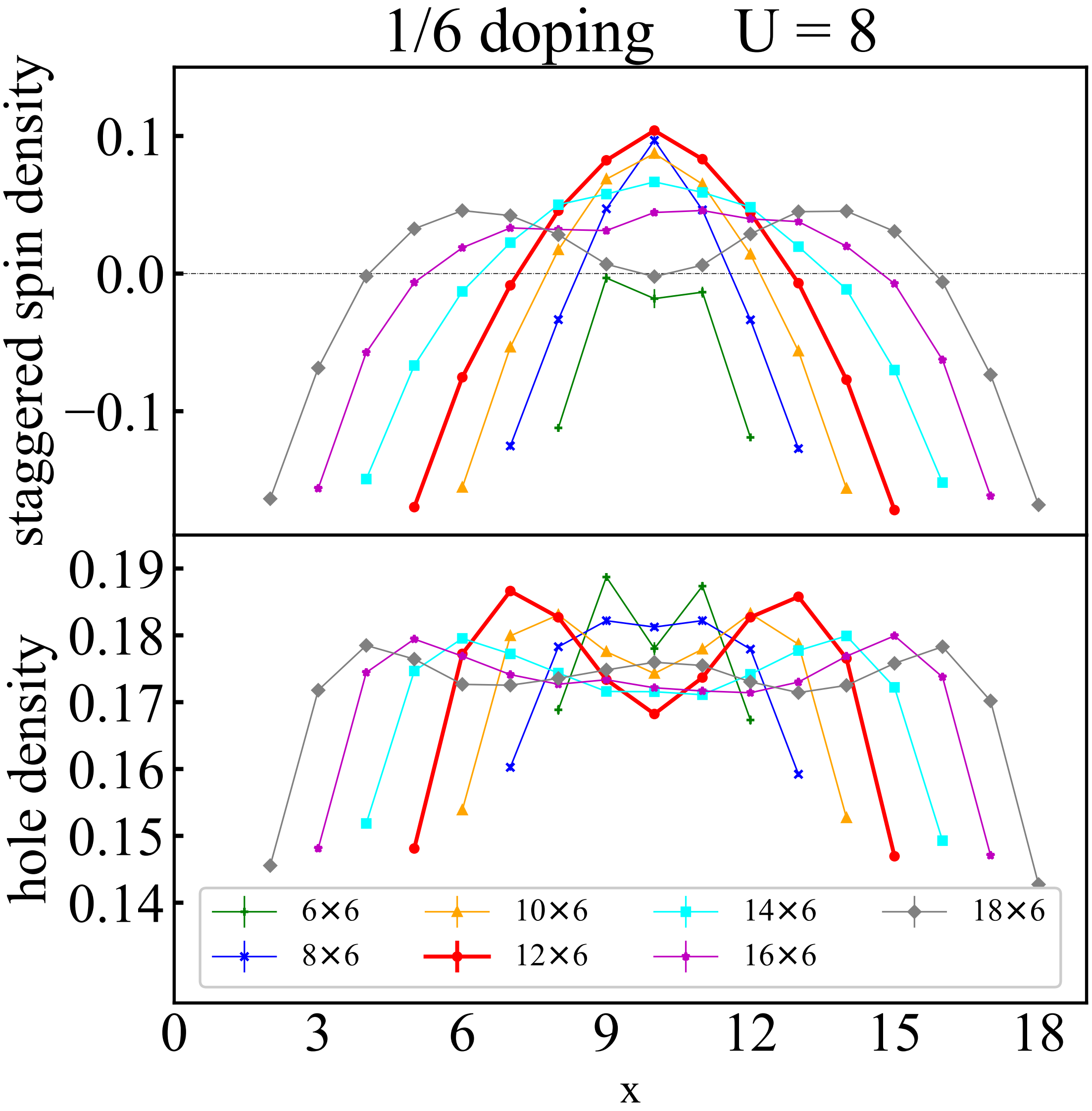

FIG. A.3: Staggered spin (top panel) and hole (bottom) densities at $\delta = 1/6$ doping and $U = 8$, in width-6 cylinders as the length $L_x$ is varied. Results are omitted at the left edge ($i_x = 1$), where the pinning field is applied. When $L_x$ is commensurate with the expected wavelengths for spin and charge orders ($1/\delta$ and $2/\delta$), the spin and charge density waves are least frustrated and have the largest amplitude.

# APPENDIX B

# Diagonal vs. linear stripes

In Hartree-Fock calculations, stripe states in the diagonal direction were observed at small doping and large $U$ [3]. Diagonal stripe states were also found to be close in energy with linear stripe state in the doped t-J model [16, 47]. In Table. B, we list the comparison of energy for linear stripe and diagonal stripe state at $U = 12$ for 1/16, 1/24, and 1/32 dopings. The energies are calculated with TABC to minimize the finite size effect [45]. As we can see in Table. B, in our calculations the linear stripe order always has a lower energy than the diagonal stripe for doping as low as $\delta = 1/32$.

| doping | 1/16 | 1/24 | 1/32 |
|---|---|---|---|
| lattice | $32 \times 8$ | $48 \times 6$ | $64 \times 6$ |
| linear stripe | -0.5095(1) | -0.4611(1) | -0.4371(2) |
| diagonal stripe | -0.5076(1) | -0.4565(1) | -0.4362(1) |

TABLE B.1: Energy comparison for linear and diagonal stripe states at $U = 12$. We can see linear stripe state always has lower energy.

# APPENDIX C

# Double occupancy and effective doping of model

The double occupancy of Hubbard model $D = \langle \sum_i n_{i\uparrow} n_{i\downarrow} \rangle / N$ measure the overall probabilities of two electrons of opposite doping occupy the same lattice. Since the interaction U describe the punishment given when two electron come together, it is very natural to conclude that double occupancy will decrease as U increases. Also, when the doping increases, the electrons have more freedom, which will lower the probability of two electrons coming together. Thus, it is also natural to refer that double occupancy will decrease with doping.

However, is there any quantitative relation between U and doping? What we are interested in the most is not any finite lattice, but thermodynamic limit. Instead of using the extrapolation of various sizes of the lattices, which is very time consuming, we use twist average boundary condition of a single large lattice. We also use Hellman-Feynman theorem to obtain the double occupancy from energies rather than back propagation, which has much larger errorbar.

Given the Hamiltonian of Hubbard model in equtaion (1.1), we obtain the double occupancy from the total energy calculations:

$$D(U) \equiv \langle \frac{dH}{dU} \rangle = \frac{dE(U)}{dU} \tag{C.1}$$

In this method, we can avoid using back-propagation, which causes greater system error and fluctuations. The higher accurate results is obtained by the derivative of energy. To compute the derivative of energy, we use the following equation, which $\delta$ is chosen to be sufficiently small to ensure the error is smaller than statistical error.

$$\frac{dE(U)}{dU} = \frac{9}{8\delta}(E(U+\delta) - E(U-\delta) + E(U-2\delta) + E(U+2\delta)) + O(\delta^4) \tag{C.2}$$

This method is also used in the computation of pairing order in Chapter 5.

First, we would like to prove the correctness of this method and our AFQMC accuracy, the Fig.C.1 shows the comparison of double occupancy of Hubbard model at half-filling, between AFQMC and Metropolis. In half-filling case, due to the particle hole symmetry, the metropolis works and can get highly accurate results without any system error, since the metropolis does not set any constraint in path.

The double occupancy with increased U and different doping is shown in Fig.C.2

We also show the effective hoping with respect to doping and U, which the effective hoping $t_{eff}$ is defined as

$$\frac{t_{eff}}{t} = \frac{\langle K \rangle_U}{\langle K \rangle_{U=0}} = \frac{E(U) - UdE(U)/dU}{E(0)} \tag{C.3}$$

The effective hoping result is shown in Fig.C.3

Below is the detailed result of Fig.C.2, the table is to be filled later

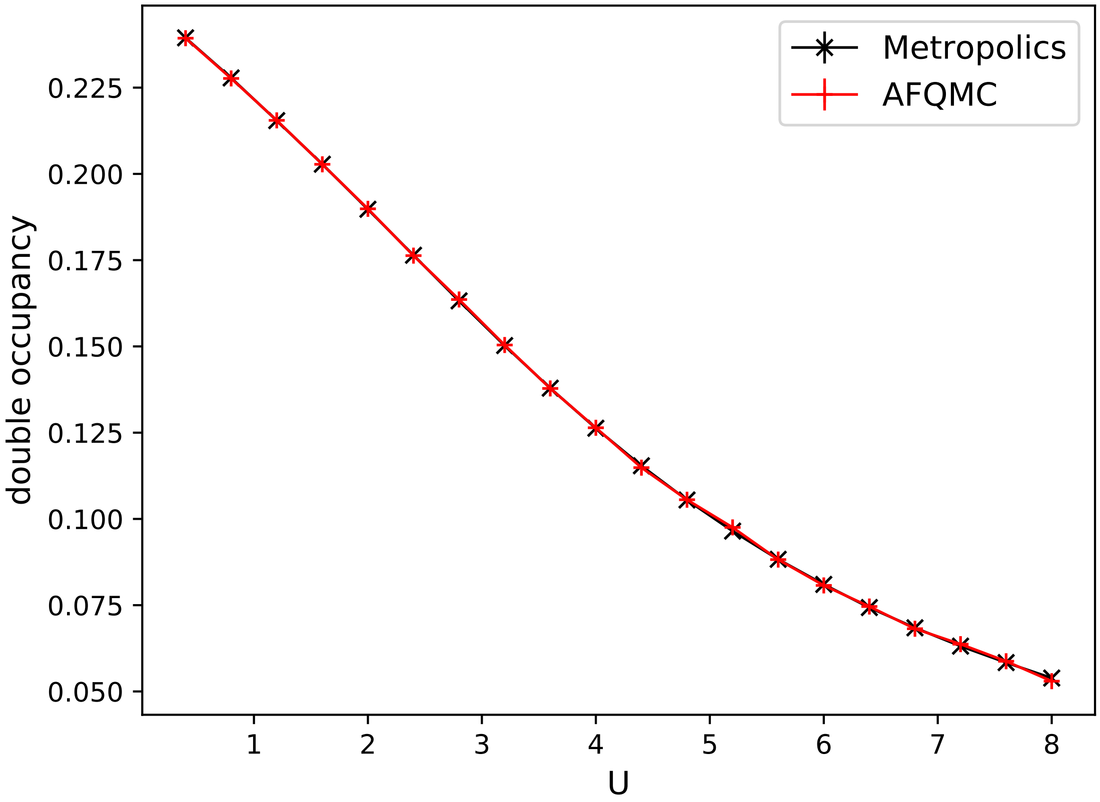

FIG. C.1: The comparison of double occupancy of Hubbard model at half-filling, between AFQMC and Metropolis, which can get results without system error since t does not constraint the path. The results the highly accuracy of double occupancy calculation.

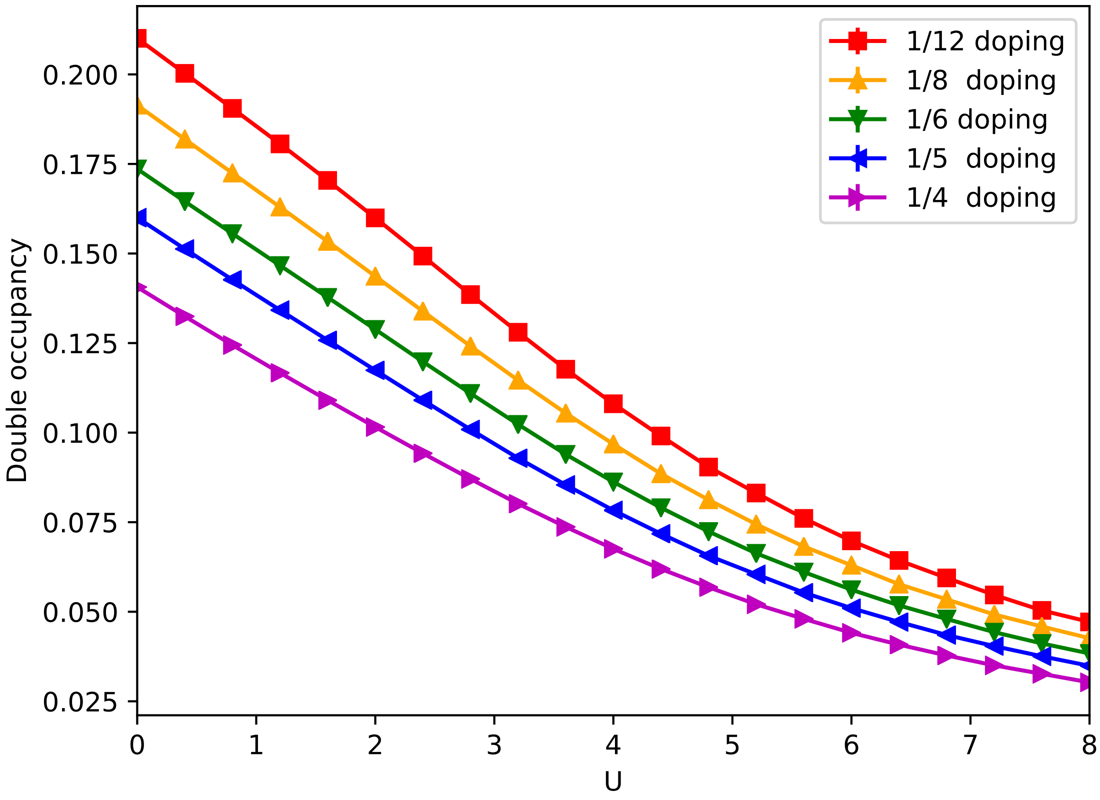

FIG. C.2: Double occupancy of pure Hubbard model with respect to U in different doping.

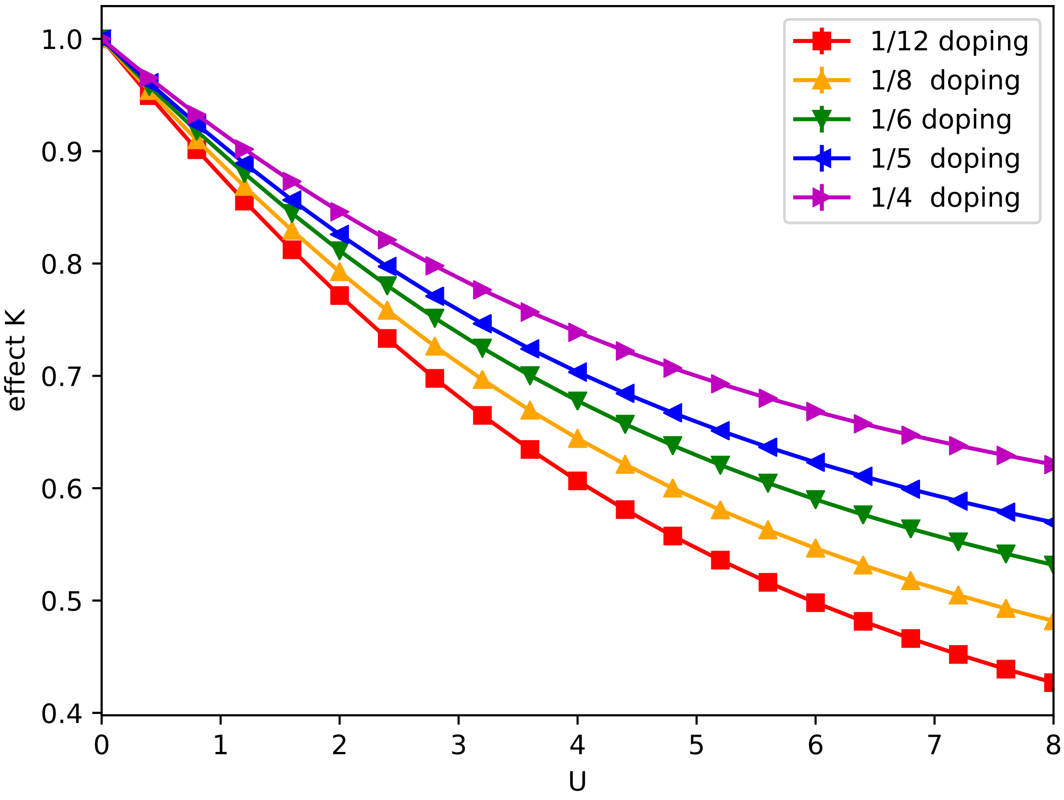

FIG. C.3: Effetive hoping of pure Hubbard model with respect to U in different doping.

| doping | 0 | 1/12 | 1/8 | 1/6 | 1/5 | 1/4 |
|---|---|---|---|---|---|---|
| U=0.0 | 0.2500 | 0.2101 | 0.1914 | 0.1736 | 0.1600 | 0.1406 |
| U=0.4 | 0.2397(1) | 0.2003(1) | 0.1819(1) | 0.1645(1) | 0.1513(1) | 0.1324(1) |
| U=0.8 | 0.2291(2) | 0.1905(1) | 0.1724(1) | 0.1556(1) | 0.1427(1) | 0.1245(0) |
| U=1.2 | 0.2179(4) | 0.1806(1) | 0.163(1) | 0.1466(1) | 0.1342(1) | 0.1167(0) |
| U=1.6 | 0.2054(6) | 0.1704(1) | 0.1534(1) | 0.1378(1) | 0.1258(1) | 0.1090(1) |
| U=2.0 | 0.1921(5) | 0.1599(0) | 0.1436(1) | 0.1288(1) | 0.1174(1) | 0.1016(1) |
| U=2.4 | 0.1780(4) | 0.1493(1) | 0.1339(1) | 0.1198(1) | 0.1091(1) | 0.0942(1) |
| U=2.8 | 0.1643(3) | 0.1385(1) | 0.1241(1) | 0.1109(2) | 0.1009(2) | 0.0871(1) |
| U=3.2 | 0.1503(3) | 0.1280(2) | 0.1146(1) | 0.1023(2) | 0.0929(2) | 0.0801(1) |
| U=3.6 | 0.1382(4) | 0.1177(2) | 0.1054(2) | 0.0939(2) | 0.0854(2) | 0.0737(1) |
| U=4.0 | 0.1260(5) | 0.1081(2) | 0.0968(2) | 0.0862(2) | 0.0783(2) | 0.0675(2) |
| U=4.4 | 0.1156(6) | 0.0991(3) | 0.0885(2) | 0.0790(3) | 0.0718(2) | 0.0619(2) |
| U=4.8 | 0.1055(5) | 0.0904(4) | 0.0812(2) | 0.0724(3) | 0.0656(2) | 0.0568(2) |
| U=5.2 | 0.0969(5) | 0.0831(4) | 0.0744(3) | 0.0663(3) | 0.0604(2) | 0.0521(2) |
| U=5.6 | 0.0882(5) | 0.0761(5) | 0.0682(3) | 0.0611(3) | 0.0553(2) | 0.0480(2) |
| U=6.0 | 0.0805(7) | 0.0698(5) | 0.0630(3) | 0.0562(3) | 0.0510(2) | 0.0441(2) |
| U=6.4 | 0.0750(7) | 0.0643(5) | 0.0577(3) | 0.0518(3) | 0.0471(2) | 0.0408(2) |
| U=6.8 | 0.0680(6) | 0.0594(5) | 0.0534(3) | 0.0480(3) | 0.0435(3) | 0.0378(2) |
| U=7.2 | 0.0637(6) | 0.0547(6) | 0.0492(3) | 0.0443(3) | 0.0404(2) | 0.0350(2) |
| U=7.6 | 0.0582(6) | 0.0504(6) | 0.0459(4) | 0.0411(3) | 0.0376(3) | 0.0327(2) |
| U=8.0 | 0.0537(7) | 0.0472(6) | 0.0426(4) | 0.0384(3) | 0.0349(3) | 0.0303(2) |

TABLE C.1: Detailed double occupancy result in Fig.C.2

# APPENDIX D

# Conductivity of model

Apart from the double occupancy of Hubbard model, it is also crucial to decide the conductivity of the Hubbard model. Is the positive U pure Hubbard conductor or insulator? There are several ways of determining the conductivity of the model. One way is to calculate the charge gap, which is defined as

$$\Delta = \frac{1}{2}(E(N_e+1) - E(N_e)) + \frac{1}{2}(E(N_e-1) - E(N_e)) = \frac{E(N_e+1) + E(N_e-1)}{2} - E(N_e) \tag{D.1}$$

Where $N_e$ is number of electrons.

The non-zero charge gap in infinite lattice indicates the insulation of Hubbard model, especially in the half-filling case [11]. The charge gap in the doped case is as below.

We illustrate several examples, one indicates absence of SDW state in the TDL and others in with SDW, which is shown in Fig.3.12. The charge gap of these examples is shown in Fig.D.1. In these examples, we can see the all systems, whether SDW exists or not, show that charge gap become zero with the increase of system size, which indicates Hubbard model is conductive regardless of the existence of SDW.

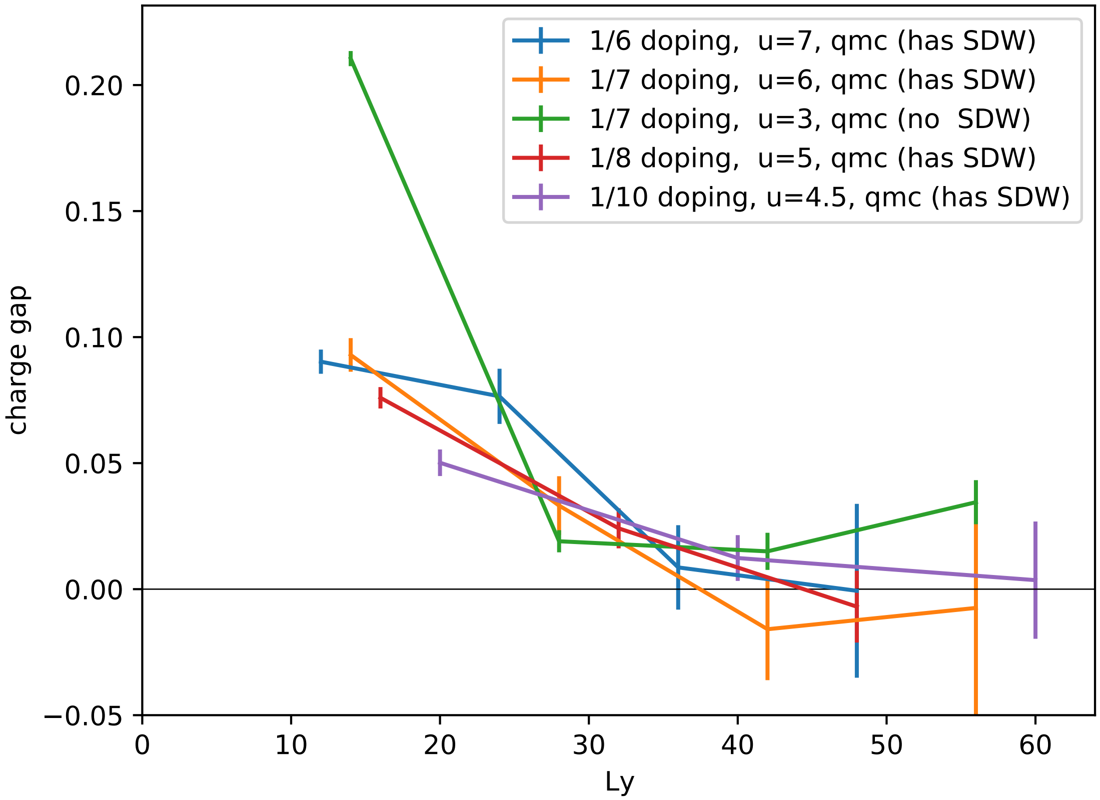

FIG. D.1: The charge gap of several examples, one (U=3, 1/7 doping) is paramagnetic in the TDL and others (U=4.5 with 1/10 doping, U=5 with 1/8 doping, U=6 with 1/7 doping, U=7 with 1/6 doping) indicates the existence of SDW in the TDL according to the Fig.refphase-diagram. All results are with-8 cylinder. With the increase of size, all results, whether have SDW or not, see the charge gap vanishes to zero. This indicates the conductive state of doped Hubbard model, regardless the existence of SDW.

Besides the charge gap calculation, we also have the Quantum metric tensor calculation to depict the conductivity. In the cylinder boundary condition, we have the location operator as

$$\hat{r} = \sum_{i=1}^{N} r_i \tag{D.2}$$

And the quantum metric tensor is defined as

$$\eta_{\alpha\beta} = \langle \psi_0 | \hat{r}_\alpha \hat{r}_\beta | \psi_0 \rangle - \langle \psi_0 | \hat{r}_\alpha | \psi_0 \rangle \langle \psi_0 | \hat{r}_\beta | \psi_0 \rangle \tag{D.3}$$

Where $\alpha$ and $\beta$ is the dimension of the lattice model. In cylinder boundary condition, we calculate the $\eta_{xx}$ since we have open boundary condition in $x$ . More details about this equation can be found in Raffaele Resta's paper [54]. In the conductor, we expect the diverge $\eta_{xx}$ value with the increase of the length of cylinder, while in the insulator, we expect the converge value.

The figure D.2 below is the quantum metric tensor calculation in different systems. In the systems that SDW is absent in TDL, we observe clearly diverge value of quantum metric tensor (QM tensor) with the increase of cylinder length (x-direction), which has strong indication that the doped Hubbard models which are paramagnetic, are conductor. However, we cannot decide quantitatively if QM tensor value converge when SDW is present. We cannot decide whether systems are conducting or not based on our present QM tensor data. However, we can see the QM tensor value is much smaller when U is increased, and the behavior is more like converging. The probability of SDW state is insulating, is higher than that of paramagnetic state.

In all, for the paramagnetic state, both charge gap and QM tensor calculation indicates the conducting state of the Hubbard model in the TDL. However, in the SDW state, the charge gap indicates that it is conductor, but QM tensor calculation shows the possibility

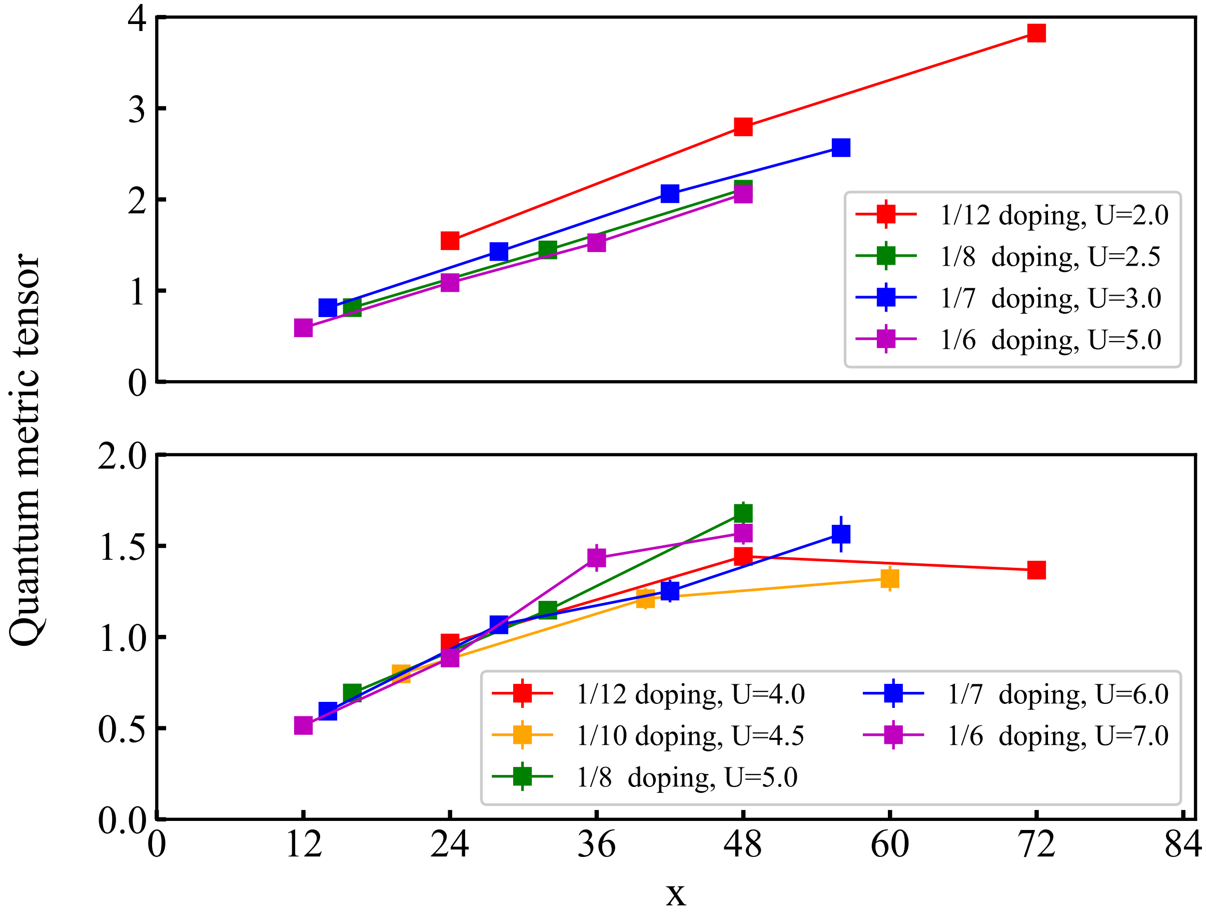

FIG. D.2: The quantum metric tensor (QM tensor) of all the systems. The lower panel includes systems that have SDW in TDL, while systems which is paramagnetic in TDL is included in the upper panel. We observe clearly diverge QM tensor value in the upper panel, which indicates the strong conductivity in the paramagnetic model. However, although the value is much smaller, we cannot decide quantitatively whether the QM tensor value converge in the lower panel. Thus we cannot decide whether system is conducting or not in our present QM tensor data.

of insulator, and we cannot safely determine the conductivity in the state which SDW presents.

# BIBLIOGRAPHY

[1] S. Zhang, J. Carlson, and J. E. Gubernatis, Phys. Rev. B **55**, 7464 (1997), URL `https://link.aps.org/doi/10.1103/PhysRevB.55.7464`.

[2] S. Yamada, T. Imamura, and M. Machida, pp. 243–256 (2018).

[3] J. Xu, C.-C. Chang, E. J. Walter, and S. Zhang, Journal of Physics: Condensed Matter **23**, 505601 (2011), URL `https://doi.org/10.1088/0953-8984/23/50/505601`.

[4] Proceedings of the Royal Society of London A: Mathematical, Physical and Engineering Sciences **276**, 238 (1963), ISSN 0080-4630, URL `http://rspa.royalsocietypublishing.org/content/276/1365/238`.

[5] M. Qin, T. Schäfer, S. Andergassen, P. Corboz, and E. Gull, arXiv e-prints arXiv:2104.00064 (2021), `2104.00064`.

[6] D. J. Scalapino, Rev. Mod. Phys. **84**, 1383 (2012), URL `https://link.aps.org/doi/10.1103/RevModPhys.84.1383`.

[7] S. R. White and A. L. Chernyshev, Phys. Rev. Lett. **99**, 127004 (2007), URL `https://link.aps.org/doi/10.1103/PhysRevLett.99.127004`.

[8] E. H. Lieb and F. Y. Wu, Phys. Rev. Lett. **20**, 1445 (1968), URL `https://link.aps.org/doi/10.1103/PhysRevLett.20.1445`.

[9] Y. Nagaoka, Phys. Rev. **147**, 392 (1966), URL `https://link.aps.org/doi/10.1103/PhysRev.147.392`.

[10] J. P. F. LeBlanc, A. E. Antipov, F. Becca, I. W. Bulik, G. K.-L. Chan, C.-M. Chung, Y. Deng, M. Ferrero, T. M. Henderson, C. A. Jiménez-Hoyos, et al. (Simons Collaboration on the Many-Electron Problem), Phys. Rev. X **5**, 041041 (2015), URL `https://link.aps.org/doi/10.1103/PhysRevX.5.041041`.

[11] E. Vitali, H. Shi, M. Qin, and S. Zhang, Phys. Rev. B **94**, 085140 (2016), URL `https://link.aps.org/doi/10.1103/PhysRevB.94.085140`.

[12] P. A. Lee, N. Nagaosa, and X.-G. Wen, Rev. Mod. Phys. **78**, 17 (2006), URL `https://link.aps.org/doi/10.1103/RevModPhys.78.17`.

[13] S. R. White and D. J. Scalapino, Phys. Rev. Lett. **80**, 1272 (1998), URL `https://link.aps.org/doi/10.1103/PhysRevLett.80.1272`.

[14] C.-C. Chang and S. Zhang, Phys. Rev. B **78**, 165101 (2008), URL `https://link.aps.org/doi/10.1103/PhysRevB.78.165101`.

[15] C.-C. Chang and S. Zhang, Phys. Rev. Lett. **104**, 116402 (2010), URL `https://link.aps.org/doi/10.1103/PhysRevLett.104.116402`.

[16] P. Corboz, T. M. Rice, and M. Troyer, Phys. Rev. Lett. **113**, 046402 (2014), URL `https://link.aps.org/doi/10.1103/PhysRevLett.113.046402`.

[17] L. F. Tocchio, F. Becca, and S. Sorella, Phys. Rev. B **94**, 195126 (2016), URL `https://link.aps.org/doi/10.1103/PhysRevB.94.195126`.

[18] E. Gull, O. Parcollet, and A. J. Millis, Phys. Rev. Lett. **110**, 216405 (2013), URL `https://link.aps.org/doi/10.1103/PhysRevLett.110.216405`.

[19] B.-X. Zheng, C.-M. Chung, P. Corboz, G. Ehlers, M.-P. Qin, R. M. Noack, H. Shi, S. R. White, S. Zhang, and G. K.-L. Chan, Science **358**, 1155 (2017), ISSN 0036-8075, URL `https://science.sciencemag.org/content/358/6367/1155`.

[20] L. F. Tocchio, A. Montorsi, and F. Becca, SciPost Phys. **7**, 21 (2019), URL `https://scipost.org/10.21468/SciPostPhys.7.2.021`.

[21] K. Ido, T. Ohgoe, and M. Imada, Phys. Rev. B **97**, 045138 (2018), URL `https://link.aps.org/doi/10.1103/PhysRevB.97.045138`.

[22] P. Mai, S. Karakuzu, G. Balduzzi, S. Johnston, and T. A. Maier, arXiv e-prints arXiv:2106.01944 (2021), `2106.01944`.

[23] J. Zaanen and O. Gunnarsson, Phys. Rev. B **40**, 7391 (1989), URL `https://link.aps.org/doi/10.1103/PhysRevB.40.7391`.

[24] D. Poilblanc and T. M. Rice, Phys. Rev. B **39**, 9749 (1989), URL `https://link.aps.org/doi/10.1103/PhysRevB.39.9749`.

[25] K. Machida, Physica C: Superconductivity **158**, 192 (1989), ISSN 0921-4534, URL `https://www.sciencedirect.com/science/article/pii/092145348990316X`.

[26] J. M. Tranquada, Advances in Physics **69**, 437 (2020), URL `https://doi.org/10.1080/00018732.2021.1935698`.

[27] A. Wietek, Y.-Y. He, S. R. White, A. Georges, and E. M. Stoudenmire, Phys. Rev. X **11**, 031007 (2021), URL `https://link.aps.org/doi/10.1103/PhysRevX.11.031007`.

[28] M. Ido, N. Yamada, M. Oda, Y. Segawa, N. Momono, A. Onodera, Y. Okajima, and K. Yamaya, Physica C: Superconductivity **185-189**, 911 (1991), ISSN 0921-4534, URL `https://www.sciencedirect.com/science/article/pii/092145349191679X`.

[29] M. Qin, H. Shi, and S. Zhang, Phys. Rev. B **94**, 235119 (2016), URL `https://link.aps.org/doi/10.1103/PhysRevB.94.235119`.

[30] V. S.A.Kivelson, E.Fradkin, Nature (1998), URL `https://doi.org/10.1038/31177`.

[31] T. I. Vanhala and P. Törmä, Phys. Rev. B **97**, 075112 (2018), URL `https://link.aps.org/doi/10.1103/PhysRevB.97.075112`.

[32] E. Fradkin, S. A. Kivelson, and J. M. Tranquada, Rev. Mod. Phys. **87**, 457 (2015), URL `https://link.aps.org/doi/10.1103/RevModPhys.87.457`.

[33] M. Qin, C.-M. Chung, H. Shi, E. Vitali, C. Hubig, U. Schollwöck, S. R. White, and S. Zhang (Simons Collaboration on the Many-Electron Problem), Phys. Rev. X **10**, 031016 (2020), URL `https://link.aps.org/doi/10.1103/PhysRevX.10.031016`.

[34] S. Zhang, *Auxiliary-Field Quantum Monte Carlo at Zero- and Finite-Temperatures*, Vol. 9 of *Many-body methods for real materials*, Ed. E. Pavarini, E. Koch, and S. Zhang (Verlag des Forschungszentrum Jülich, 2019), URL `http://www.cond-mat.de/events/correl19`.

[35] S. Z. Hao Shi (2021), URL `https://aip.scitation.org/doi/10.1063/5.0031024`.

[36] H.F.Trotter, Proceedings of the American Mathematical Society, vol. 10, no. 4, American Mathematical Society, 1959 (1959), URL `https://doi.org/10.2307/2033649`.

[37] J. Hubbard, Phys. Rev. Lett. **3**, 77 (1959), URL `https://link.aps.org/doi/10.1103/PhysRevLett.3.77`.

[38] J. E. Hirsch, Phys. Rev. B **28**, 4059 (1983), URL `https://link.aps.org/doi/10.1103/PhysRevB.28.4059`.

[39] D. R. Hamann and S. B. Fahy, Phys. Rev. B **41**, 11352 (1990), URL `https://link.aps.org/doi/10.1103/PhysRevB.41.11352`.

[40] S. R. White, D. J. Scalapino, R. L. Sugar, E. Y. Loh, J. E. Gubernatis, and R. T. Scalettar, Phys. Rev. B **40**, 506 (1989), URL `https://link.aps.org/doi/10.1103/PhysRevB.40.506`.

[41] S. Zhang and H. Krakauer, Phys. Rev. Lett. **90**, 136401 (2003), URL `https://link.aps.org/doi/10.1103/PhysRevLett.90.136401`.

[42] H. Xu, H. Shi, E. Vitali, M. Qin, and S. Zhang, Phys. Rev. Research **4**, 013239 (2022), URL `https://link.aps.org/doi/10.1103/PhysRevResearch.4.013239`.

[43] S. R. White, Phys. Rev. Lett. **69**, 2863 (1992), URL `https://link.aps.org/doi/10.1103/PhysRevLett.69.2863`.

[44] S. R. White, Phys. Rev. B **48**, 10345 (1993), URL `https://link.aps.org/doi/10.1103/PhysRevB.48.10345`.

[45] C. Lin, F. H. Zong, and D. M. Ceperley, Phys. Rev. E **64**, 016702 (2001), URL `https://link.aps.org/doi/10.1103/PhysRevE.64.016702`.

[46] Y.-F. Jiang, J. Zaanen, T. P. Devereaux, and H.-C. Jiang, Phys. Rev. Research **2**, 033073 (2020), URL `https://link.aps.org/doi/10.1103/PhysRevResearch.2.033073`.

[47] S.-J. Dong, C. Wang, Y.-J. Han, C. Yang, and L. He, npj Quantum Materials **5**, 28 (2020), `1908.10000`.

[48] R. Peters and N. Kawakami, Phys. Rev. B **89**, 155134 (2014), URL `https://link.aps.org/doi/10.1103/PhysRevB.89.155134`.

[49] F. C. Zhang and T. M. Rice, Phys. Rev. B **37**, 3759 (1988), URL `https://link.aps.org/doi/10.1103/PhysRevB.37.3759`.

[50] M. Dolfi, B. Bauer, S. Keller, and M. Troyer, Phys. Rev. B **92**, 195139 (2015), URL `https://link.aps.org/doi/10.1103/PhysRevB.92.195139`.

[51] G. Ehlers, S. R. White, and R. M. Noack, Phys. Rev. B **95**, 125125 (2017), URL `https://link.aps.org/doi/10.1103/PhysRevB.95.125125`.

[52] S. Zhang, J. Carlson, and J. E. Gubernatis, Phys. Rev. Lett. **78**, 4486 (1997), URL `https://link.aps.org/doi/10.1103/PhysRevLett.78.4486`.

[53] S. Jiang, D. J. Scalapino, and S. R. White, Proceedings of the National Academy of Sciences **118**, e2109978118 (2021), `https://www.pnas.org/doi/pdf/10.1073/pnas.2109978118`, URL `https://www.pnas.org/doi/abs/10.1073/pnas.2109978118`.

[54] R. Resta, The European Physical Journal B **79**, 121 (2011), URL `https://link.springer.com/article/10.1140/epjb/e2010-10874-4`.

# VITA

## Hao Xu

Hao Xu was born on August 16th, 1995. He showed strong interest in math and science since he was in primary school. He entered the University of Science and Technology of China in 2011 and transformed into a physics major in his sophomore year. He received his bachelor degree in 2015 and entered William and Mary physics department for his graduate study. Eventually, With his interest in both physics and coding, he joined prof. Shiwei Zhang's computational condensed matter group in 2017, focusing stripe and superconductivity study of Hubbard model. In his spare time, he ran several full marathons and ranked top 0.5% in Google Code Jam competition. After graduation, he hopes to use his math and coding skills to contribute in the field of finance or computer science.